NORTHWESTERN UNIVERSITY

Single-Electron Detection with a SQUID: Toward Quantum-Limited, Relativistic Detection

A DISSERTATION

SUBMITTED TO THE GRADUATE SCHOOL
IN PARTIAL FULFILLMENT OF THE REQUIREMENTS

for the degree of

DOCTOR OF PHILOSOPHY

PHYSICS

By

Benedict A. D. Sukra

EVANSTON, ILLINOIS
DECEMBER, 2025

Dissertation advisor

Gerald Gabrielse

Author

Benedict A. D. Sukra

Single-Electron Detection with a SQUID: Toward Quantum-Limited, Relativistic Detection

Abstract

Our 2023 measurement of the electron magnetic moment in Bohr magnetons, $\mu_s/\mu_B = g/2 = 1.001\ 159\ 180\ 59\ (13)$ is the most precise determination of a property of any fundamental particle. It provides the most precise test of the Standard Model of particle physics. The precision is limited by two systematic effects–a lineshape broadening related to the trapped electron's temperature, and a frequency shift arising from the coupling of the trapped electron and the microwave modes of its confining cavity.

An extensive new apparatus, including a *near*-quantum-limited SQUID and an optimized cylindrical Penning trap has been commissioned. A twenty-fold reduction in the axial temperature of the particle will reduce lineshape broadening and improve the precision of a non-destructive quantum state readout. The improved trap geometry supports a transition toward a quantum non-demolition detection based on a relativistic mass increase, eliminating the need for the use of an inhomogeneous magnetic field. Cavity shifts will be better characterized and corrected for due to a factor of five reduction in trap volume leading to mode density suppression.

One electron has been detected in the new apparatus with the highest signal-to-noise ratio ever observed. Careful characterization of the detector and apparatus identifies surmountable challenges to be addressed, establishing a clear path toward the next-generation, far more precise measurements of the electron and positron magnetic moments.

Acknowledgments

First and foremost, I would like to thank my advisor Professor Gerald Gabrielse, whose intuition, patience, experience, and guidance have profoundly shaped my growth as a scientist. His constant push to innovate and to invent new techniques for this decades-old experiment is the reason we have achieved the progress we have, even during the moments when I doubted whether it would all work out. We dared to take the experiment in a new direction, and for his encouragement, confidence, and vision in making that possible, I am deeply grateful.

I am also grateful to the other members of my committee, Professors André de Gouvêa and Tim Kovachy, for their guidance and support throughout graduate school. I am especially thankful for their insightful questions and advice during my prospectus exam and thesis defense.

I am deeply grateful to Xing Fan, who mentored me during my early stages of my graduate career and who continues to be a thoughtful mentor today. His insistence to "just try" remains one of the most valuable lessons I learned during my PhD. I would also like to thank the graduate students and postdocs on the electron magnetic moment experiment with whom I have had the opportunity to work with. I am indebted to Sam Fayer, Thomas Myers, and Geev Nahal, from whom I learned immensely from in my early years. I am equally grateful to the newer graduate students, Lily Soucy and Bani Sinha, who are now carrying the experiment forward. I greatly appreciate our discussions, their thoughtful questions, and

their dedication in running the experiment while I wrote this thesis. I am proud to have worked with an exceptional group of undergraduate students– Alyssa Matthews, Shungo Fukaya, Owen Roark, Evan Shaman, Saif Salim, and Jacob Garcia, whose creativity and hard work made meaningful contributions to the experiment.

I have also been fortunate to overlap with many other talented graduate students, post-docs, and research staff whose friendship and insightful conversations have enriched my time at Northwestern– Andra Ionescu, Nathaniel McDonough, Daniel Ang, Collin Diver, Zhen Han, Bingjie Hao, Ayami Hiramoto, Peiran Hu, Wayne Huang, Daniel Lascar, Siyuan Liu, Cole Meisenhelder, John Mitchell, Tharon Morrison, Edouard Nottet, Eric Tardiff, Maya Watts, Xing Wu, Junfeng Zhou, and Daniel Zambrano.

A substantial part of this work involved building a new apparatus from the ground up. This would not have been possible without the contributions from the machinists of the Northwestern Machine shop: Thang Bui, Bob Golenia, Salomon Rodriguez, Dinka Spirovska, and John Bussan. Without their efforts and guidance, we would not have built the robust system that we have today. Special thanks must also go to Laura Nevins for her exceptional administrative, logistical, and procurement support.

I would like to thank my parents, family, and friends for their unwavering love and encouragement. I am profoundly grateful to my parents, Benie and Marion Sukra, and to my sister, Krystal Sukra, for their boundless support throughout this journey. I am especially thankful to my partner, Nia Burrell, whose kindness, patience, and encouragement made the latter half of my PhD far more enjoyable. To my friend, Cole Kampa–thank you for keeping me honest and for your steadfast friendship through it all.

Finally, I gratefully acknowledge the continuous support of the electron and positron magnetic moment experiments by the National Science Foundation, the U.S. Department of Energy through the Superconducting Quantum Materials and Systems Center (SQMS), and the John Templeton Foundation.

Contents

List of Figures

List of Tables

Chapter 1

The Electron Magnetic Moment

The electron is an elementary particle with charge e, mass m_e, spin-1/2 and no known internal structure. The measurement of the magnetic moment proportional to its intrinsic spin angular momentum is the subject of this thesis. The electron magnetic moment in Bohr magnetons $\mu_B = e\hbar/2m_e$ is

$$\frac{\vec{\mu}_s}{\mu_B} = -\frac{g}{2}\frac{\vec{S}}{\hbar/2}, \tag{1.1}$$

where $\hbar$ is the reduced Planck constant, and g is the gyromagnetic ratio or g-factor. The g-factor is given by,

$$\frac{g}{2} = -\frac{\vec{\mu_s}}{\mu_B} = 1 + a, \tag{1.2}$$

where a is the small correction ($a \approx 10^{-3}$) known as the anomalous magnetic moment.

In 1928, Dirac's relativistic equation predicted a g-factor exactly equal to 2 [1]. In 1947, Kusch and Foley made the first measurement of the g-factor, discovering a discrepancy from Dirac's prediction at the part-per-thousand level [2]. Attempts to explain this 'anomaly' in recalculations of the magnetic moment contributed to the development of quantum electrodynamics (QED) in 1948 [3–5].

Today, both the measurement and theory prediction of the g-factor of the electron reach

sub-parts-per-trillion (ppt) precision. The theory prediction includes contributions from all sectors of the Standard Model, thus the comparison of the measured electron magnetic moment to the theory prediction provides the most precise test of the Standard Model of particle physics. At the same time, places strong constraints on physics beyond the Standard Model. Any new particle or interaction that couples to the electron not included in the SM would modify the magnetic moment at some loop order, shifting the experimentally measured value while leaving the SM prediction unchanged. Since both the measurement and prediction reach sub-ppt precision, even extremely small BSM effects may become detectable.

The work described in this thesis builds on my contribution to the most precise measurement of the electron magnetic moment ever achieved. Our 2023 measurement of the electron magnetic moment, made with a single electron in a Penning trap cooled to its ground cyclotron state, yielded [6],

$$\frac{g}{2} = 1.\ 001\ 159\ 652\ 59\ (13) \tag{1.3}$$

It is the most precisely determined property of any fundamental particle and its comparison to the theory prediction is precise enough to make possible the most precise test of the SM.

Experimentally, the magnetic moment is determined by measuring the ratio of the single trapped electron's spin frequency ν_s to its cyclotron frequency ν_c,

$$\frac{g}{2} = \frac{\nu_s}{\nu_c} = 1 + \frac{\nu_a}{\nu_c} \tag{1.4}$$

where we have defined the anomaly frequency $\nu_a = \nu_s - \nu_c$. The full expression, including corrections, is given in Chapter 2; here we discus a simplified form to provide the framework for the current discussion.

This chapter explores the g-factor theory prediction and the comparison of the measured

and predicted values as one of the most precise tests of the SM. We introduce the comparison of the electron and positron magnetic moments as a test of CPT invariance in leptons. Finally, we discuss the limits of the previous electron g-factor measurement and how the work described in this thesis provides a path towards an improved measurement of both the electron and positron magnetic moments.

1.1 The Standard Model Prediction

The Standard Model (SM) of particle physics provides an extremely successful theoretical framework for describing the electromagnetic, weak, and strong interactions among all known elementary particles. Despite its tremendous predictive power, best exemplified by the comparison of the measured and SM predicted values of the electron magnetic moment, the SM remain incomplete. It offers no explanation for the existence of dark matter [7,8], the origin of neutrino masses [9, 10], the nature of dark energy [11, 12], or the observed matter-antimatter asymmetry in the universe [13, 14]. Improving the precision of measurements of the SM's most sensitive predictions is therefore essential for identifying possible deviations and guiding the search for physics beyond the Standard Model.

In the framework of quantum field theory, the electron's interactions with the fluctuating vacuum give rise to radiative corrections that shift the electron magnetic moment from the Dirac prediction of $g = 2$. A complete treatment of the SM prediction of the electron magnetic moment is given in [15] and references therein, here we only summarize the results. At the current precision, the electron magnetic moment prediction includes contributions from all sectors of the SM,

$$\frac{g}{2} = \frac{\mu_s}{\mu_B} = 1 + a_{\text{QED}} + a_{\text{hadronic}} + a_{\text{weak}}, \tag{1.5}$$

where a_{QED}, a_{hadronic}, and a_{weak} are contributions from from QED, hadronic, and weak physics respectively. The QED correction includes contributions from the three lepton generations, electron, muon, and tau-lepton, and depends on the ratio of the lepton masses,

$$a_{\mathrm{QED}} = C^{(1)} + C^{(2)}\left(m_e/m_\mu\right) + C^{(2)}\left(m_e/m_\tau\right) + C^{(3)}\left(m_e/m_\mu, m_e/m_\tau\right), \tag{1.6}$$

where m_e, m_μ, and m_τ are the masses of the electron, muon and tau-lepton, respectively. The coefficients $C^{(i)}$, for $i = 1, 2, 3$, are determined from higher order QED theory as an expansion in terms of the fine structure constant α,

$$C^{(i)} = C_2^{(i)}\left(\frac{\alpha}{2\pi}\right) + C_4^{(i)}\left(\frac{\alpha}{2\pi}\right)^2 + C_6^{(i)}\left(\frac{\alpha}{2\pi}\right)^3 + \ldots \tag{1.7}$$

As the ratios of the electron to muon and tau-lepton are small, $m_e/m_\mu = 4.836\ 331\ 70\ (11) \times 10^{-3}$ and $m_e/m_\tau = 2.875\ 85\ (19) \times 10^{-4}$ [16], their contributions to the anomalous magnetic moment is not significant. The heavy lepton QED contributions are grouped and denoted as $a_{\mu,\tau}$.

We rewrite the expression for the magnetic moment as,

$$\frac{g}{2} = 1 + C_2\left(\frac{\alpha}{\pi}\right) + C_4\left(\frac{\alpha}{\pi}\right)^2 + C_6\left(\frac{\alpha}{\pi}\right)^3 + C_8\left(\frac{\alpha}{\pi}\right)^4 + C_{10}\left(\frac{\alpha}{\pi}\right)^5 + \ldots + a_{\mu,\tau} + a_{\mathrm{hadron}} + a_{\mathrm{weak}}\ , \tag{1.8}$$

where mass independent QED coefficients $C_{2n}^{(1)}$ are simplified as C_{2n}. Through the evaluation of thousands of Feynman diagrams (a subset of which are shown in Figure 1.1), these coefficients have been evaluated through the tenth-order. We summarize the results here

with key references,

$$C_2 = \frac{1}{2} = 0.5 \text{ [17]} \tag{1.9}$$

$$\begin{aligned} C_4 &= \frac{197}{144} + \frac{\pi^2}{12} + \frac{3}{4}\zeta(3) - \frac{1}{2}\pi^2 \ln 2 \\ &= -0.328\ 478\ 965\ 579\ 193\ldots \text{ [18,19]} \end{aligned} \tag{1.10}$$

$$\begin{aligned} C_6 &= \frac{83}{72}\pi^2\zeta(3) - \frac{215}{24}\zeta(5) + \frac{100}{3}\left[\left(\sum_{n=1}^{\infty}\frac{1}{2^n n^4} + \frac{1}{24}\ln^4 2\right) - \frac{1}{24}\pi^2\ln^2 2\right] \\ &\quad - \frac{239}{2160}\pi^4 + \frac{139}{18}\zeta(3) - \frac{298}{9}\pi^2\ln 2 + \frac{17101}{810}\pi^2 + \frac{28259}{5184} \\ &= 1.181\ 241\ 456\ 587 \text{ [20]} \end{aligned} \tag{1.11}$$

$$C_8 = -1.912\ 245\ 764\ 926\ldots \text{ [21,22]} \tag{1.12}$$

$$C_{10} = 5.891\ \ (61) \quad \text{[23–25]} \tag{1.13}$$

Here $\zeta(x)$ is the Riemann zeta function.

The QED contributions from the muon and tau-lepton loops are,

$$a_{\mu,\tau} = 2.747\ 572\ (1) \times 10^{-12} \quad \text{[15,22,26–32]} \tag{1.14}$$

The hadronic and weak contributions are [33],

$$a_{\text{hadron}} = 1.693\ (12) \times 10^{-12} \tag{1.15}$$

$$a_{\text{weak}} = 0.030\ 53\ (23) \times 10^{-12} \tag{1.16}$$

The SM prediction for the magnetic moment, Equation 1.8, is a remarkable achievement of quantum field theory. Its evaluation requires an experimentally determined value of the fine structure constant α as an input parameter. The most precise determinations of α requires

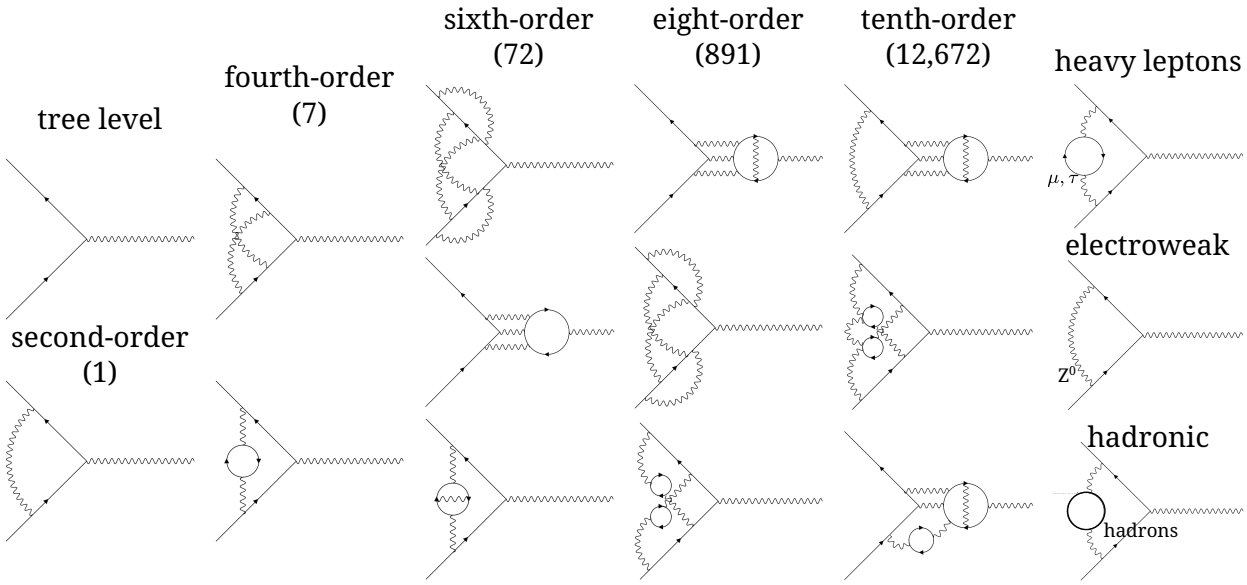

Figure 1.1: Subset of Feynman diagram evaluated to determine the electron magnetic moment. The numbers in the brackets indicate the number of diagrams evaluated at each order.

several measured quantities through the relation,

$$\alpha(X) = \left[\frac{2R_\infty}{c}\frac{A(X)}{A(e)}\frac{h}{m(X)}\right]^{1/2}, \tag{1.17}$$

where X is some atomic species, R_∞ is the Rydberg constant, $A(X)$ is the atomic mass of X, $A(e)$ is the atomic mass of the electron, and $h/m(X)$ is an experimentally determined parameter from photon recoil experiments involving the atomic species X. The most precise determinations of $h/m(X)$ for α come from rubidium (^{87}Rb) and cesium (^{133}Cs) measurements in atomic fountains.

We anticipate that as we advance the precision of the electron magnetic moment measurement, the SM prediction will be improved to enable the most stringent possible test of the theory, as the past progress has shown. In the following sections, we examine the measured input parameters to the SM prediction, identifying current limitations and improvements required to fully exploit the sensitivity of a future substantially more precise measurement

of the electron magnetic moment.

The Rydberg constant is well known from hydrogen spectroscopy, including muonic hydrogen. The most precise measurement of the Rydberg constant R_∞ in atomic hydrogen using the 1S-4P transition is [34],

$$R_\infty = 10\ 973\ 731.568\ 076\ (96)\ [8.7\ \text{ppt}] \tag{1.18}$$

The atomic masses of the electron and atom species X are determined from mass measurements in Penning traps. The atomic mass of the electron is [35, 36]

$$A(e) = 5.485\ 799\ 090\ 67\ (16) \times 10^{-4}\ \ \text{u}\ [28\ \text{ppt}] \tag{1.19}$$

The masses of ^{87}Rb and ^{133}Cs are related to carbon through several charge to mass ratio measurements. The atomic masses are determined as [37],

$$A(^{87}\text{Rb}) = 86.909\ 180\ 535\ (10)\ \text{u}\ [115\ \text{ppt}] \tag{1.20}$$

$$A(^{133}\text{Cs}) = 132.905\ 451\ 963\ (13)\ \text{u}\ [98\ \text{ppt}] \tag{1.21}$$

The quantity $h/m(X)$ is determined through momentum recoil measurements when a photon is absorbed by the species in atom interferometer measurements. The most precise results for Rb [38] and Cs [39] respectively are,

$$h/m(^{87}\text{Rb}) = 4.591\ 359\ 258\ 90\ (65) \times 10^{-9}\ \text{m}^2\ \text{s}^{-1}\ [141\ \text{ppt}] \tag{1.22}$$

$$h/m(^{133}\text{Cs}) = 3.002\ 369\ 472\ 1\ (12) \times 10^{-9}\ \text{m}^2\ \text{s}^{-1}\ [400\ \text{ppt}] \tag{1.23}$$

From the quoted values above we determine the inverse of the fine structure constant as from

the ^{87} Rb and ^{133} Cs measurements as,

$$\alpha^{-1}(^{87}\text{Rb}) = 137.035\ 999\ 203\ (11)\ [80\ \text{ppt}] \tag{1.24}$$

$$\alpha^{-1}(^{133}\text{Cs}) = 137.035\ 999\ 044\ (28)\ [203\ \text{ppt}] \tag{1.25}$$

Today, the largest uncertainties in the determination of the fine structure constant from equation 1.17 are from the photon recoil velocity measurements of ^{87}Rb and ^{133}Cs.
These measured values of the α lead to two Standard Model predictions of the magnetic moment using equation 1.8,

$$g/2\left(^{87}\text{Rb}\right) = 1.001\ 159\ 652\ 180\ 190\ (04)\ (12)\ (92) \tag{1.26}$$

$$g/2\left(^{133}\text{Cs}\right) = 1.001\ 159\ 652\ 181\ 537\ (04)\ (12)\ (235), \tag{1.27}$$

The uncertainties are from the C_{10} coefficient, hadronic contribution, and the fine structure constant respectively. Note that the discrepancy in the determination in C_{10} [25] that appeared in the 2023 g-factor result report [6] has now been resolved [24] and the uncertainty contribution of this term is now 0.004×10^{-12}.

The most recent measurements of the electron magnetic moment in our lab yielded the results,

$$g/2\ (2008) = 1.001\ 159\ 652\ 180\ 730\ (280)\ \ [40, 41] \tag{1.28}$$

$$g/2\ (2023) = 1.001\ 159\ 652\ 180\ 593\ (134)\ \ [6, 42] \tag{1.29}$$

These results are compared to the calculated prediction from the Standard Model using the measured input parameter α in Figure 1.2. This comparison is one of the most precise tests of the Standard Model of Particle Physics and strongly constrains new physics.

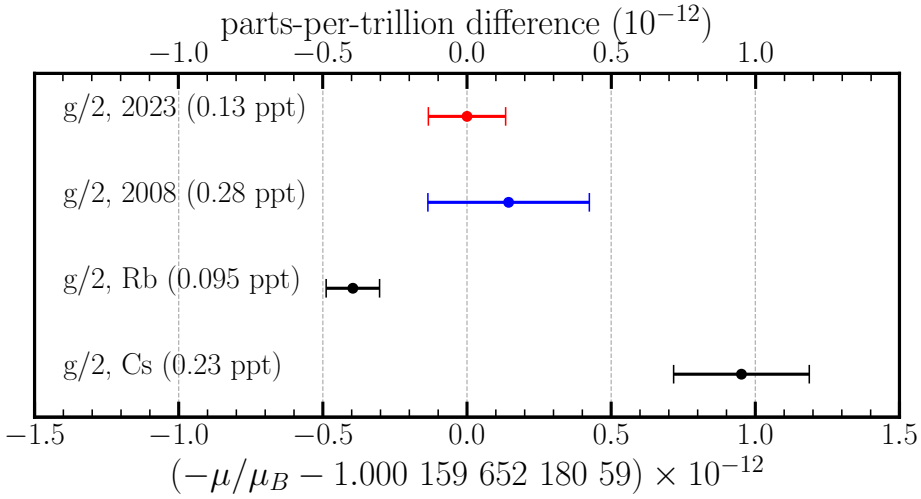

Figure 1.2: Comparison of g-factor measurements with Standard Model prediction which requires input parameter fine structure constant α. A 5.5 σ discrepancy exists between the most recent measurements of α.

While an intriguing discrepancy exists between the measured and both SM predicted magnetic moment values, $\delta(g/2,^{87}\,\mathrm{Rb}) = 0.792 \pm 0.229$ (3.5 σ) and $\delta(g/2,^{133}\,\mathrm{Cs}) = -1.904 \pm 0.489$ (-3.9 σ), these independent determinations of α are themselves discrepant at the 5.5 σ level. Therefore, the most that can be said is that the measured and predicted values of the electron magnetic moment agree to about $\delta(g/2) = 0.7 \times 10^{-12}$, about half the current α discrepancy and five times the best g-factor measurement uncertainty. At the time of writing, work is underway to resolve the current discrepancy in the measurement of α. If this is achieved, a 10 times more precise test of the SM is possible with the measurement of the g-factor at the current precision [43].

This thesis establishes the tools to improve the electron magnetic moment by a factor of at least ten. If this is achieved, not only must the current α discrepancy be resolved but the precision of the determinations of α must be improved by a factor of ten. This requires both improved measurements of $h/m(X)$ and the atomic mass measurements $A(X)$. The current uncertainty contributions to the determination of α are summarized in Table 1.1. If

contribution	^{87}Rb	^{133}Cs
R_∞	0.075×10^{-9}	0.075×10^{-9}
$A(X)$	4.7×10^{-9}	4.6×10^{-9}
$A(e)$	1.2×10^{-9}	1.2×10^{-9}
$h/m(X)$	9.7×10^{-9}	27.3×10^{-9}
total uncertainty	10.8×10^{-9}	27.8×10^{-9}

Table 1.1: Relative uncertainty contributions to the fine structure determination.

a ten times better α determination is required, then in the case of ^{87}Rb, $h/m(X)$ must be improved by a factor of ten and $A(X)$ must also be improved by a factor of 5. Going beyond this precision requires improvements in the atomic mass of the electron and an improved determination of the hadronic contribution to the SM calculation.

At the time of writing, improving the precision of the determination of the fine structure constant is the subject of major interest in the field with a Topical workshop on improving the measurement scheduled [43]. Efforts are underway to improve the measurement of α from photon recoil measurements in ^{133}Cs [44] and ^{87}Rb, this could potentially shed light on the observed α discrepancy.

Proposals have been made to measure α using other atomic species, namely Sr and Yb [45]. In both cases, the relative masses are known as well as for ^{87}Rb and ^{133}Cs– $A(^{87}\mathrm{Sr}) =$ 86.908 877 496 (5) u [58 ppt] and $A(^{171}\mathrm{Yb}) =$ 170.936 331 817 (14) u [82 ppt] [46]. With current technologies, a $h/m(X)$ measurement with fractional uncertainty 1×10^{-11} is possible for these atomic species. These future measurements will be key to resolving the current discrepant α measurements and enabling a 10 times better SM test.

1.2 Determination of the Fine Structure Constant

Equation 1.8 can be inverted to solve for the fine structure constant α as a function of the electron magnetic moment. This yields a precise determination of α, assuming that the

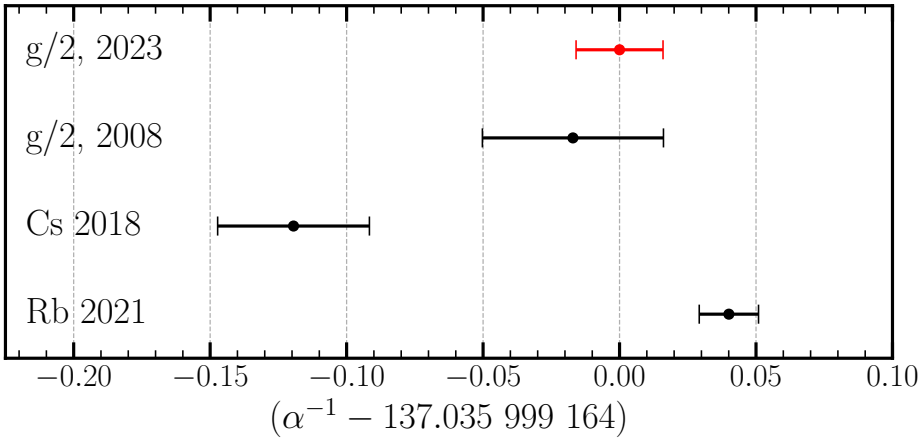

Figure 1.3: Comparison of the determined fine structure constants.

SM prediction is correct and coefficients are correctly evaluated.

Using equation 1.8 and the constants quoted previously in this thesis, we determine the α^{-1} from our two most recent g-factor measurements as,

$$\alpha^{-1}(g/2\ 2008) = 137.035\ 999\ 146\ 5\ (05)\ (14)\ (331) \tag{1.30}$$

$$\alpha^{-1}(g/2\ 2023) = 137.035\ 999\ 163\ 6\ (05)\ (14)\ (159), \tag{1.31}$$

where the uncertainties are from the C_{10} coefficient, hadronic contribution, and the fine structure constant respectively. These results are shown in Figure 1.3 along with the independent measurements of α using equation 1.17. At the current time, both the ^{87}Rb measurement and the electron g-factor through the SM yield determinations of α at similar precisions.

If the goal of a 10 times improved electron g-factor measurement is achieved, then the determination of the fine structure constant from the g-factor will be equally limited by the hadronic contribution and the improved uncertainty on the g-factor measurement.

1.3 Limits on Physics beyond the Standard Model

The comparison between the measured electron magnetic moment and the SM prediction strongly constrains physics Beyond the Standard Model (BSM). While there currently exists discrepant independent determinations of α, in this section we choose to use $\alpha(^{87}\mathrm{Rb})$ as its SM prediction yields a value more consistent with the measured electron magnetic moment. Using $\alpha(^{87}\mathrm{Rb})$, we calculate the discrepancy between measurement and theory as,

$$\delta\left(\frac{g}{2}\right) = \left(\frac{g}{2}\right)\Big|_{\text{meas.}} - \left(\frac{g}{2}\right)\Big|_{\text{theory}} = (0.79 \ \pm 0.23) \times 10^{-12} \ (3.5 \ \sigma) \tag{1.32}$$

While $\delta(g/2)$ shows a 3.5 σ tension, it tightly constrains BSM physics since any new physics contribution a_{BSM} to equation 1.8 must be smaller than the observed discrepancy, that is $a_{\text{BSM}} \leq \delta(g/2)$.

1.3.1 Dark Photon Limits

The dark photon is a hypothetical massive gauge boson carrying $U(1)$ charge. It is analogous to the SM photon and can interact with it through kinetic mixing. The modified SM Lagrangian (in natural units) including the dark photon contribution is,

$$\mathcal{L}_{\text{SM + DP}} = \mathcal{L}_{\text{SM}} - \frac{1}{4}F'_{\mu\nu}F'^{\mu\nu} - \frac{\epsilon}{2}F_{\mu\nu}F'^{\mu\nu} + \frac{m^2_{A'}}{2}A'_{\mu}A'^{\mu} \tag{1.33}$$

where A'_μ and $F'_{\mu\nu}$ are the vector and tensor fields for the dark photon respectively, $F_{\mu\nu}$ is the tensor field of the normal photon, $m_{A'}$ is the mass of the dark photon, and ϵ is the kinetic mixing between the normal and dark photons.

Similar to how the SM photon contributes to the electron magnetic moment at higher orders, the dark photon can couple to the electron as shown in Figure 1.4. The first order loop correction to the magnetic moment from the dark photon is similar in form to the first

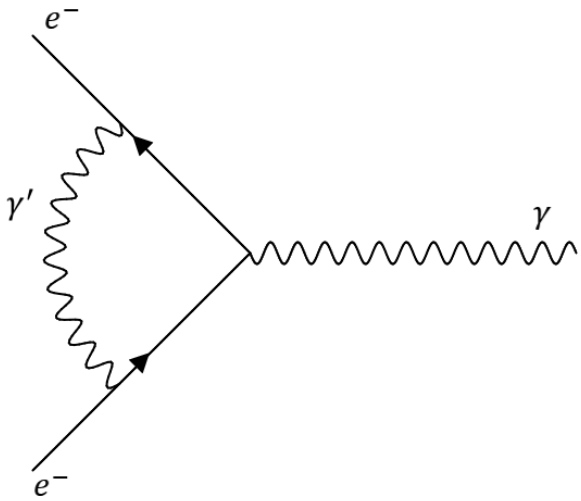

Figure 1.4: Dark photon contribution to the electron magnetic moment at the one loop level.

order correction from the SM photon but scaled by the kinetic-mixing term ϵ and the finite mass of the dark photon $m_{A'}$,

$$a_{\text{dark photon}} = \epsilon^2 \frac{\alpha}{2\pi} \times F\left(\frac{m_{A'}}{m_e}\right), \tag{1.34}$$

where,

$$F(x) = \int_0^1 \frac{2z(1-z)^2}{(1-z)^2 + x^2 z} dz \tag{1.35}$$

We can then set a limit on the dark photon using the observed discrepancy between the SM prediction and measurement [47,48], $a_{\text{dark photon}} \leq \delta(g_e/2) = (0.79 \pm 0.23) \times 10^{-12}$. The limit with 99% confidence level is shown in Figure 1.5. A similar limit can be obtained from the discrepancy between the muon magnetic moment measurement and prediction [49,50]. This limit is also shown in Figure 1.5.

Other searches for the dark photon in this mass range are performed using the invisible decay method in beam dump or collider experiments. Limits from NA48 [51], BaBar [52], and LHCb and CMS [53–55] are shown in Figure 1.5. Note that in the invisible decay

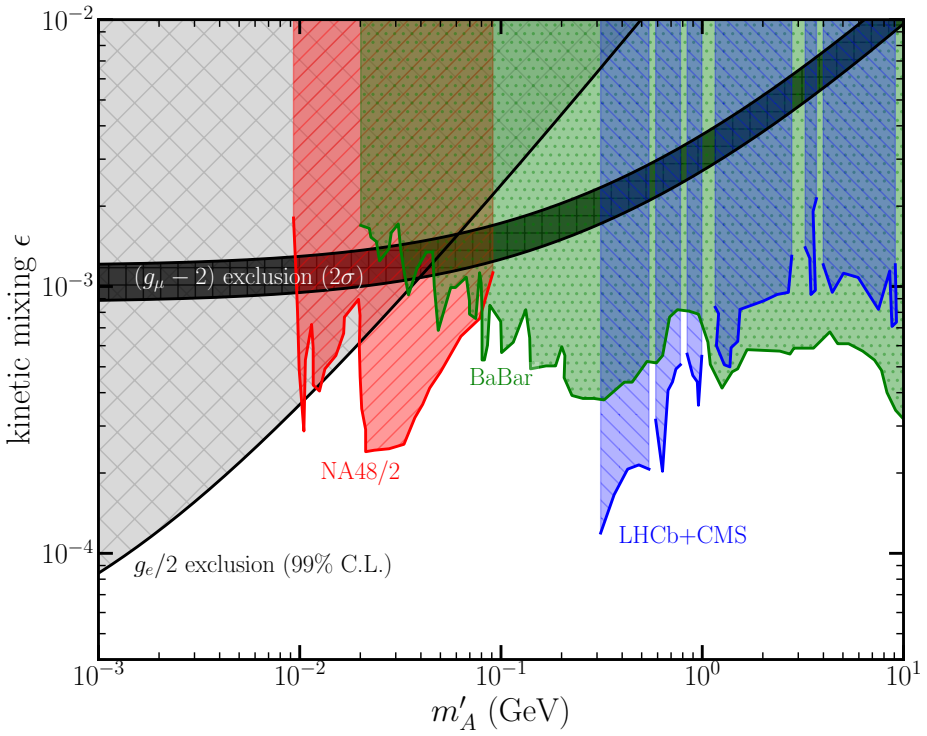

Figure 1.5: Dark photon limit from electron magnetic moment. The limits from the invisible decay methods are reproduced from [48]

searches, unlike in the electron and muon limits, the additional assumption of the dark photon decaying to additional dark sector particles is made. Therefore, the electron and muon measurements set model independent limits on the dark photon in this mass while the invisible decay method is model dependent.

1.4 Electron and Positron Magnetic Moments as a Test of CPT Invariance

In the framework of the Standard Model, physical observables are unchanged under the simultaneous transformation of **C**harge conjugation (particle transformed to its antiparticle), **P**arity inversion (spatial inversion through a point), and **T**ime reversal (reversal of the

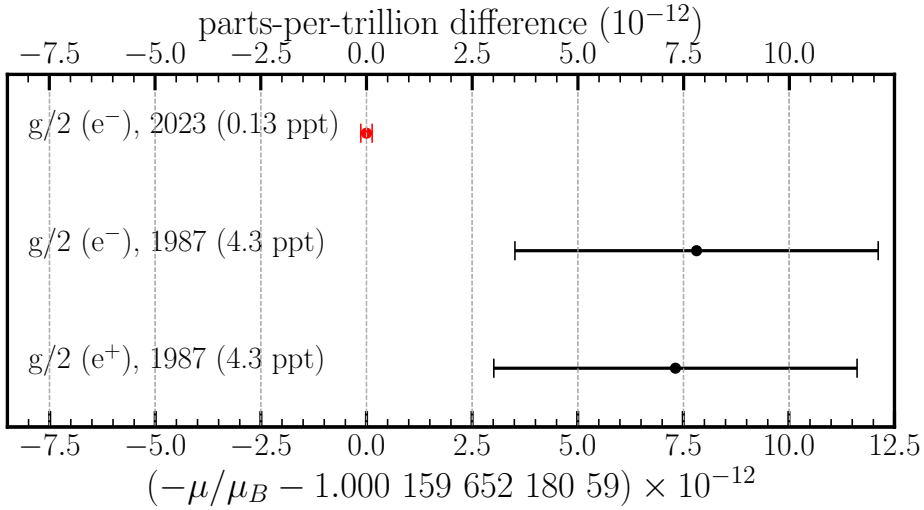

Figure 1.6: Comparison of most recent electron magnetic moment with most recent positron magnetic moments.

directions of all motions). The invariance of the SM under the inversion of these three discrete symmetries is called the CPT theorem or CPT Invariance.

The strongest bound on CPT invariance comes from the the comparison of the kaon and anti-kaon masses [56, 57],

$$|m_{K^0} - m_{\bar{K^0}}|/m_{\text{avg}} < 6 \times 10^{-19}, \text{C.L.} = 90\% \tag{1.36}$$

For leptons, the strongest limit on CPT invariance comes from the 1987 UW measurements of the electron and positron in the same apparatus [57, 58],

$$|g_{e^-,\ 1987}/2 - g_{e^+,\ 1987}/2| = (0.5 \pm 6.1) \times 10^{-12}\ (0.1\ \sigma) \tag{1.37}$$

The most recent measurement of the electron magnetic moment improved on the last measured positron magnetic moment by a factor of 30. Comparing these two measurements

instead yields,

$$|g_{e^-,\ 2023}/2 - g_{e^+,\ 1987}/2| = (7.31 \pm 4.3) \times 10^{-12}\ (1.7\ \sigma), \tag{1.38}$$

where the uncertainty is dominated by the much larger positron measurement uncertainty. A comparison of the previous measurements in the UW experiments with our most recent measurement is shown in Figure 1.6.

The apparatus described in this thesis is a newly designed and built system for a future positron measurement. Replicating the 2023 electron magnetic moment measurement precision with the positron improves the test of the CPT theorem in leptons by a factor of 30, and implementing the new techniques developed in this thesis could push the precision of the measurement of both the electron and positron magnetic moments even further.

1.5 The Next Generation of Electron & Positron Magnetic Moments

The most recent measurement of the electron magnetic moment [6, 42] involved trapping a single electron in a cylindrical Penning trap [59], cooling it to its quantum cyclotron ground state in a dilution refrigerator [60], and measuring the difference between the cyclotron and spin frequencies using a non-destructive quantum state-readout scheme [60] using cryogenic HEMT amplifiers [61,62]. This precision of this measurement was limited by two systematic effects, (Table 1.2) :

- the cavity shift correction - a shift of the measured spin and cyclotron frequencies in the Penning trap from the free space value due to the microwave modes in the Penning trap cavity itself [63, 64]

name	shift (10^{-12})	uncertainty (10^{-12})
total statistical	—	0.029
total systematic	-0.004	0.132
microwave cavity correction	—	0.090
line shape model	0.000	0.094
cyclotron power shift	0.000	0.005
anomaly power shift	0.000	0.010
fluctuation of axial frequency	0.000	0.003
axial frequency shift by resonator	−0.004	0.003
uncertainty of axial damping rate	0.000	0.003
magnetic field drift	0.000	0.009
temperature fluctuation	0.000	0.012
correction from the invariance theorem	0.000	0.000
total	−0.004	0.134

Table 1.2: Uncertainty budget in the 2023 electron magnetic moment measurement (reproduced from [42]).

- an unknown additional broadening that appears in the measured cyclotron lineshape but not the spin lineshape

In this thesis, we describe the construction of an entirely new apparatus to measure both the electron and positron magnetic moments that directly aims to improve on previous measurements by addressing the systematic effects limiting its precision. A new more harmonic Penning trap is designed and demonstrated for higher precision measurement of the particle's axial frequency and a positron accumulation trap has been designed and installed for collecting positrons for a future positron magnetic moment measurement (Chapter 2). The more harmonic trap will enable higher axial frequency resolution and enable quantum nondemolition state-readout from the associated relativistic mass shift of the particle instead of the magnetic bottle [65]. This will give us a 20 times narrower cyclotron linewidth leading to a significantly improved measurement.

A new dilution refrigerator and superconducting magnet has been commissioned for the

use of a *near*-quantum limited Superconducting QUantum Interference Device (SQUID) amplifier for state read out. This system overcomes the challenge of implementing a superconducting amplifier in the large magnetic field of the Penning trap used for the electron experiment. Detection of a single electron with this new amplifier has been demonstrated (Chapter 3).

This new detector and the removal of the magnetic bottle offers a path to narrowing the measured cyclotron lineshape by a factor of 25 but this is still to be observed. If achieved, this will place us in a regime where the expected cyclotron linewidth is much closer to the measured anomaly linewidth. We expect that in this regime we can investigate the source of the observed unknown additional broadening. If the source of the unknown broadening is from magnetic field fluctuations on the tens to hundreds of Hz scale, we have designed and commissioned an active vibration cancellation platform on which the entire apparatus sits to address this. This is discussed in Chapter 2.

The last systematic effect to address is the cavity shift systematic. In Chapter 4, I first outline the cavity correction performed for the 2023 electron magnetic moment measurement. This work informed the design of the new Penning trap cavity. With the new design we expect a reduction in the cavity shift systematic by a factor of 2 if the correction follows exactly what was done in the 2023 measurement. In this regime, the precision electron magnetic moment measurement will be limited by the cavity shift systematic and an improvement by a factor 3 is achievable. Improving beyond this to take full advantage of the potential enabled by the SQUID amplifier and the relativistic detection scheme requires an alternative approach. I will also discuss some possibilities in Chapter 4.

Finally, while we have built and demonstrated the tools for quantum limited detection with state-readout using special relativity, this is still to be demonstrated. Chapter 5 outlines a relativistic detection scheme, what work remains to be done to realize it, and future directions for the electron and positron magnetic moment measurements.

Chapter 2

The Experiment and Apparatus

The measurement of the electron magnetic moment relies on trapping and detecting the motion of a single electron in a Penning trap. In this chapter, we discuss the principle of the measurement using a single particle, its motion in the Penning trap, and the newly constructed and commissioned apparatus used for the experiment.

2.1 Principle of Measurement

Fundamental particles, such as electrons, have both an orbital angular momentum $\vec{L}$ and an intrinsic angular momentum called spin $\vec{S}$. These two angular momenta give rise to an orbital magnetic moment,

$$\vec{\mu_L} = \frac{-e}{2m_e}\vec{L} = -\mu_B \frac{\vec{L}}{\hbar}, \tag{2.1}$$

where $-e$ is the charge of the electron, m_e is the mass of the electron, $\hbar$ is the reduced Planck constant, and $\mu_B = e\hbar/2m_e$ is the Bohr magnetron, and a spin magnetic moment,

$$\vec{\mu_S} = g\frac{-e}{2m_e}\vec{S} = -g\mu_B\frac{\vec{S}}{\hbar}, \tag{2.2}$$

where g is known as the gyromagnetic ratio or the g-factor. The measurement and prediction of the g-factor has a deep historical legacy that is summarised in Chapter 1 and explored in more depth elsewhere [66, 67]. This chapter focuses on the measurement of $g/2$.

In a magnetic field, $\vec{B} = B\hat{z}$, the spin flip and cyclotron energies for an electron are,

$$\hbar\omega_s = |2\vec{\mu_s}B| = \frac{g}{2}\frac{\hbar eB}{m}, \tag{2.3}$$

and,

$$\hbar\omega_c = \frac{\hbar eB}{m}. \tag{2.4}$$

Thus,

$$\frac{g}{2} = \frac{\omega_s}{\omega_c} \tag{2.5}$$

In the actual experiment, we measure the ratio

$$\frac{g}{2} = 1 + \frac{\omega_a}{\omega_c}, \tag{2.6}$$

where the anomaly frequency, ω_a, is defined as the difference between the spin and cyclotron frequencies, $\omega_a \equiv \omega_s - \omega_c$ is about 1000 times smaller than the spin and cyclotron frequencies. By measuring the ratio in equation 2.6, we are able to make a 1000 times more precise

measurement of $g/2$.

For a high precision determination of the magnetic moment, both a highly stable and homogeneous magnetic field are required, along with a long interrogation time. We use a Penning trap as it allows us to confine an electron in a small volume over which the magnetic field is extremely homogeneous for an indefinite amount of time.

This chapter will introduce the details of the measurement of the electron g-factor starting with a more general introduction to Penning traps then the specific apparatus designed for this iteration of the measurement. We have made several improvements over the work of this thesis, including the design and commissioning of a new Penning trap with improved anharmonicity for the g-factor measurement, a second open-endcap trap for positron accumulation for a future positron g-factor measurement, and an entirely new dilution refrigerator and superconducting magnet system required for the implementation of a superconducting *near*-quantum limited detector that is discussed in Chapter 3. The rest of this chapter describes this entirely new apparatus designed, installed, and commissioned for electron and positron magnetic moment measurements.

2.2 The Ideal Penning Trap

A Penning trap is a static trap for confining charged particles that utilizes a large magnetic field and an electrostatic quadrupole. [68,69]. The large magnetic field is provided by a superconducting solenoid while an electrostatic quadrupole is provided by a set of electrodes that is appropriately designed and biased. In the ideal case, the electrostatic quadrupole is formed by a pair of hyperbolic electrodes since the hyperbolic electrodes themselves are the equipotential surface for a electrostatic quadrupole (Figure 2.1). While the hyperbolic geometry was used in earlier Penning trap experiments, today cylindrical Penning traps are favored, both for manufacturing ease and, specifically for the electron g-factor, for the

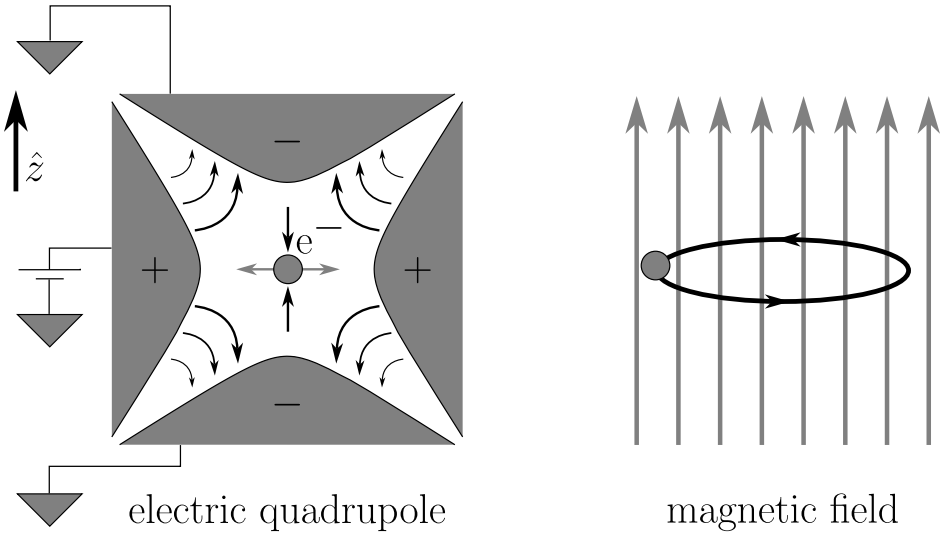

Figure 2.1: Ideal Penning Trap. The trapped ion is confined along the axial ($\hat{z}$) direction by an electric quadrupole formed by hyperbolic electrodes and radially via the Lorentz force via a strong magnetic field along the axial direction.

microwave cavity correction (Chapter 4)

2.2.1 Dynamics of a Charged Particle in a Penning Trap

For completeness we first briefly describe the classical motion of the particle in a Penning trap. At the temperatures achieved in this experiment, a quantum mechanical description of the motion is required, that discussion is presented in the following section.

Classical Motion

In the ideal Penning trap a uniform magnetic field,

$$\vec{B}(\rho, z) = B\hat{z}, \tag{2.7}$$

and a quadratic electrostatic potential,

$$\phi(\rho, z) = V_0 \left(\frac{z^2 - \rho^2/2}{2} \right), \tag{2.8}$$

are applied. The resulting forces on the particle are the Lorentz force and the electric force. These applied fields generate three orthogonal motions as illustrated in 2.2 for classical motions. Along the z-axis the classical axial motion of the particle is independent of the magnetic field and is described by the simple harmonic motion equation,

$$\ddot{z} + \omega_z^2 z = 0, \tag{2.9}$$

where the axial frequency is given by,

$$\omega_z = \sqrt{\frac{eV_0}{m_e}}. \tag{2.10}$$

The transverse motion is a result of the superposition of the Lorentz force from the axial magnetic field and the radial (anti-trapping) potential contribution from the electrostatic quadrupole. The resulting equation of motion is,

$$\ddot{\boldsymbol{\rho}} - \omega_c \times \dot{\boldsymbol{\rho}} - \frac{1}{2}\omega_z^2 \boldsymbol{\rho} = 0, \tag{2.11}$$

where $\omega_c = eB/m_e$ is the free space cyclotron frequency. The $-\frac{1}{2}\omega_z^2 \vec{\rho}$ term originates from the repulsive radial contribution of the electrostatic potential. Transforming equation 2.11 to complex coordinates using $u = x + iy$, the equation of motion becomes,

$$\frac{d^2u}{dt^2} - i\omega_c \frac{du}{dt} - \frac{\omega_z^2}{2} u = 0, \tag{2.12}$$

which has solutions in the form $u_\pm = \rho_\pm e^{i\omega_\pm t}$, describing two circular motions with eigenfrequencies,

$$\omega_\pm = \frac{1}{2}\left(\omega_c \pm \sqrt{\omega_c^2 - 2\omega_z^2}\right) \tag{2.13}$$

In the limit $\omega_z \to 0$, that is without the electrostatic quadrupole, then the radial motion is simply the cyclotron motion. Therefore, the addition of the radially repulsive electrostatic quadrupole field modifies the cyclotron motion into two non-degenerate motions, a fast motion denoted by frequency ω_+ called the modified cyclotron motion, and a slower motion ω_- called the magnetron motion. For a typical electron Penning trap, since the free space cyclotron frequency is much larger than the axial frequency, $\omega_c/\omega_z \sim 10^{-3}$, then the modified cyclotron frequency can be approximated as,

$$\omega_+ = \frac{1}{2}\left(\omega_c + \sqrt{\omega_c^2 - 2\omega_z^2}\right) \approx \omega_c - \frac{\omega_z^2}{2\omega_c} = \omega_c - \omega_m \equiv \omega_c' \tag{2.14}$$

and the magnetron frequency can be approximated as,

$$\omega_- = \frac{1}{2}\left(\omega_c - \sqrt{\omega_c^2 - 2\omega_z^2}\right) \approx \frac{\omega_z^2}{2\omega_c} \equiv \omega_m, \tag{2.15}$$

Energies and Damping Rates

The energies associated with these three motions are derived in detail elsewhere [68] and here we will just summarize the results. The energy associated with the axial motion is the energy of a system in simple harmonic motion with amplitude of oscillation z_A,

$$E_z = \frac{1}{2} m\omega_z^2 z_A^2. \tag{2.16}$$

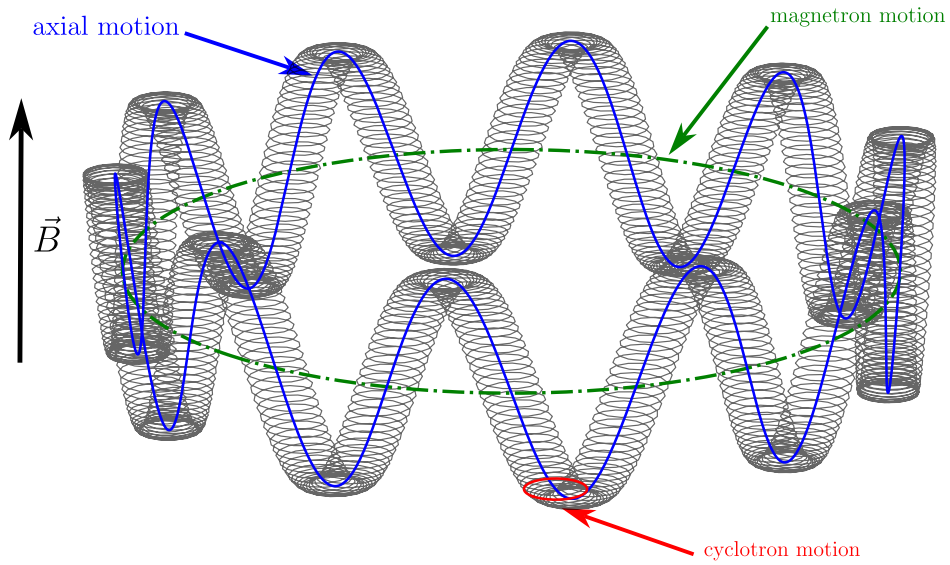

Figure 2.2: Classical Motion of a particle in a Penning Trap

The energy associated with the modified cyclotron motion and magnetron motions with radii ρ_c and ρ_m, respectively, comprise of the kinetic energy associated with that motion, simply $\frac{1}{2}m_e\left(\frac{d\rho}{dt}\right)^2$, and the electrostatic potential energy in the radial direction $-\frac{1}{4}\omega_z^2\rho^2$. Therefore for the modified cyclotron motion,

$$E_c = \frac{1}{2}m\left(\omega_c'^2 - \frac{1}{2}\omega_z^2\right)\rho_c^2 \approx \frac{1}{2}m\omega_c'^2\rho_c^2, \tag{2.17}$$

and for the magnetron motion,

$$E_m = \frac{1}{2}m\left(\omega_m^2 - \frac{1}{2}\omega_z^2\right)\rho_m^2 \approx -\frac{1}{4}m\omega_z^2\rho_m^2, \tag{2.18}$$

both of which have been simplified using the approximation $\omega_c \gg \omega_z \gg \omega_m$ which is true for the electron Penning trap systems used in this work.

It is worth noting that the magnetron motion is unstable, denoted by the negative energy. Therefore, the un-driven magnetron motion will slowly decay into larger and larger orbits until the trapped particle is lost from the trap due to a collision with its walls. The radius

of the magnetron motion is kept small and stable through an RF drive that imparts energy (heats the motion) but shrinks the radius. We typically call this drive the magnetron cooling drive.

The three Penning trap motions all thermalize to their respective equilibrium temperatures on largely different timescales and through different mechanisms. The cyclotron motion will radiatively cool to the ambient temperature of the trap. In free space, this lifetime is given by,

$$\tau_c = \frac{1}{\gamma_c} = 4\pi\epsilon_0 \frac{3m_e c^3}{4e^2\omega_c^2}; \tag{2.19}$$

however, in the high quality (Q) factor cylindrical microwave cavity that forms the Penning trap, spontaneous emission is enhanced on-resonance with these microwave modes and significantly suppressed off-resonance [70]. This inhibition of spontaneous emission is leveraged to extend the cyclotron lifetime from $\tau_c \sim 0.09$ s by a factor 50-100 to $\tau_c \sim 5 - 10$ s at 5.5 T, typically what is used in the g-factor measurement.

For a significant section of the work in this thesis, for the stable operation of the SQUID amplifier (Chapter 3), the experiment is performed at a far reduced field of 0.75 T. Here the free space cyclotron lifetime is $\tau_c \sim 4.5$ s and we expect a much longer extension to the cyclotron lifetime due to the cavity effect on order 100-1000 s.

The axial motion is read out via a detection resonator that strongly damps its motion. The detection and damping of the axial motion is described later in this chapter, but for this section we will just state that the typical damping time constant for the apparatus described in this thesis is $\tau_z = \gamma_z^{-1} \approx 0.008$ s.

The radiative damping of the magnetron motion is essentially identical to the cyclotron motion, and so the *lifetime* of the magnetron motion has the same form as the free space

lifetime of the cyclotron motion scaled to the magnetron frequency,

$$\tau_m = \frac{1}{\gamma_m} = 4\pi\epsilon_0 \frac{3mc^3}{4e^2\omega_m^2} \frac{\omega_c' - \omega_m}{\omega_m} \approx 4\pi\epsilon_0 \frac{3mc^3\omega_c'}{4e^2\omega_m^3} \approx 10^{12} \text{ s} \tag{2.20}$$

In addition to the three Penning trap motions, the trapped electron has a fourth motion by virtue of its intrinsic spin angular momentum. The electron can either be in the spin up ($m_s = +1/2$) or spin down ($m_s = -1/2$) state. The frequency associated with this transition has been previously given in equation 2.3 and the radiative decay rate from spin up to down is given as [68],

$$\tau_s = \frac{1}{\gamma_s} = 4\pi\epsilon_0 \frac{6m^2c^5}{g^2\hbar e^2\omega_s^3} \tag{2.21}$$

At 5.5 T and 0.75 T, the spin decay rate is 4.5 years and 1628 years respectively, timescales much longer than experiment timescale. The spin state therefore remains unchanged throughout the experiment unless directly driven.

Quantum Mechanical Motion

At the temperatures at which the g-factor experiment is performed, a more accurate description of the particle's motion requires quantum mechanics. The three orthogonal Penning trap motions are described simply by three orthogonal quantum harmonic oscillators and the spin state is a two-level quantum system. The Hamiltonian for the system is given explicitly as,

$$\mathcal{H} = \hbar\omega_c' \left(\hat{a}_c^\dagger \hat{a}_c + \frac{1}{2}\right) + \hbar\omega_z \left(\hat{a}_z^\dagger \hat{a}_z + \frac{1}{2}\right) - \hbar\omega_m \left(\hat{a}_m^\dagger \hat{a}_m + \frac{1}{2}\right) + \hbar\omega_s \frac{1}{2}\hat{\sigma}_z, \tag{2.22}$$

where $\hat{a}_i$ and $\hat{a}_i^\dagger$ are the creation and annihilation operators respectively for the cyclotron, axial, and magnetron motions ($i = c,\ z,\ m$ respectively), and $\hat{\sigma_z}$ is the z component of the Pauli matrix. The quantum numbers for the cyclotron, axial, and magnetron states are

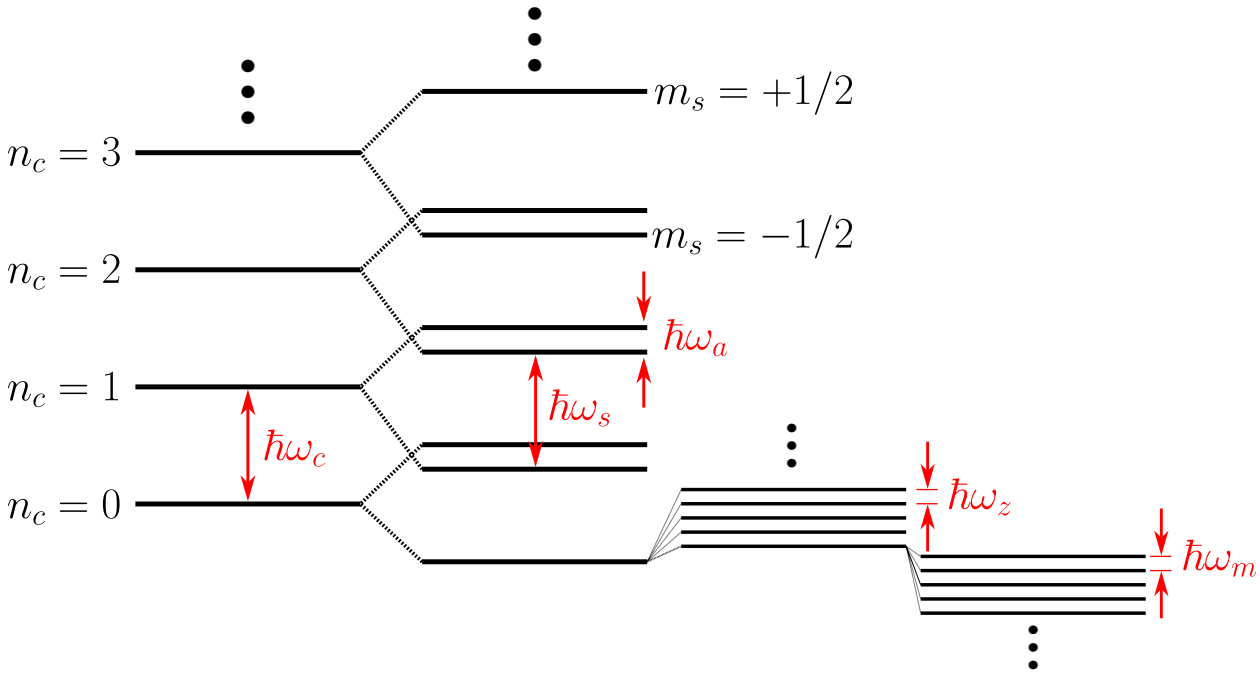

Figure 2.3: Energy level splitting for an electron in a Penning trap (not to scale). The cyclotron level ladder is shown on the far left. Going from left to right, each cyclotron level is split into two spin levels ($m_s = \pm 1/2$, then divided into the axial sub-levels then finally the magnetron sub-levels. Unlike with the cyclotron and axial levels, the magnetron levels are inverting, indicated that this motion is unbound.

denoted by n_i for $i = c,\ z,$ and m, respectively, and $m_s = \pm 1/2$ for the spin states. The level diagram for the system is shown in Figure 2.3 (not to scale). The quantum harmonic oscillator states are described by Bose-Einstein statistics and so average occupation number for these motions in thermal equilibrium with a bath at temperature T is,

$$\bar{n}_i = \left[\exp\left(\frac{\hbar\omega_i}{k_{\mathrm{B}}T}\right) - 1\right]^{-1}. \tag{2.23}$$

The cyclotron motion is cooled via synchrotron radiation until it comes into thermal equilibrium with the physical temperature of the walls of the Penning trap which are cooled by a dilution refrigerator to less than 10 mK. At 0.75 T, $\bar{n}_c = 1.7 \times 10^{-44}$ and at 5.5 T, $\bar{n}_c = 1.3 \times 10^{-319}$. In both cases $\bar{n}_c$ is effectively 0 and the probability of the cyclotron motion

being thermally excited to the first state is 1.6×10^{-44} and 6.5×10^{-322} for 0.75 T and 5.5 T respectively. Thus an electron cooled to its ground state via synchrotron radiation will remain in the ground state indefinitely unless excited by an external drive.

In this thesis we implement a Superconducting Quantum Interference Device (SQUID) amplifier at 120 MHz (Chapter 3). The dilution refrigerator used achieves temperatures of less than 10 mK. The axial motion comes into thermal equilibrium with the amplifier used to read out this motion. At 120 MHz the noise temperature of the SQUID should approach the quantum-limited temperature $T_Q = \hbar\omega/k_B T = 2.9$ mK; however in practice SQUIDs achieve noise temperatures $2 - 5 \times T_Q$ [71–73] . Therefore, in this limit we expect the axial motion temperature to come into thermal equilibrium with the bath temperature, i.e. the base temperature of the dilution refrigerator. At 10 mK the average axial occupation number $n_z \approx 1.3$, almost the quantum ground state.

Since the magnetron motion is *cooled* to a smaller orbit through coupling to the axial motion, the magnetron temperature is then $T_m = -(\omega_m/\omega_z) \times T_z$. Thus the magnetron energy expressed as a temperature is approximately 100 times smaller than the axial temperature. At 0.75 T, $T_m \approx 30$ μK and at 5.5 T, $T_m \approx 4$ μK, while the average occupation number is the same as that for the axial motion $n_m \sim 1$ in this regime.

Table 5 summarizes the characteristic frequencies, damping rates, and quantum numbers at two magnetic field strengths: 0.75 T, at which much of the SQUID demonstration work has been carried out, and 5.5 T, the field historically used for g-factor measurements.

Brown-Gabrielse Invariance Theorem

Thus far we have described an ideal Penning trap system with a quadrupole field that is exactly described by 2.8 and a magnetic field 2.7 perfectly aligned with the axis of the quadrupole field. In practice this is not achievable due to misalignment of the electrodes axis with the applied magnetic field. Additionally, machining imperfections of the electrodes

	frequency	damping time	quantum number
$B = 0.75$ T			
spin	$\omega_s/2\pi \approx 21.0$ GHz	$(\gamma_s/2\pi)^{-1} \approx 1638$ yrs	$m_s = \pm 1/2$
cyclotron	$\omega_c/2\pi \approx 21.0$ GHz	$(\gamma_c/2\pi)^{-1} \approx 4.5$ s	$\bar{n}_c = 1.7 \times 10^{-44}$
axial	$\omega_z/2\pi \approx 120$ MHz	$(\gamma_z/2\pi)^{-1} \approx 0.008$ s	$\bar{n}_z = 1.3$
magnetron	$\omega_m/2\pi \approx 20$ GHz	$(\gamma_m/2\pi)^{-1} \approx 10^{12}$ s	$\bar{n}_m = 1.3$
$B = 5.5$ T			
spin	$\omega_s/2\pi \approx 154.1$ GHz	$(\gamma_s/2\pi)^{-1} \approx 4.2$ yrs	$m_s = \pm 1/2$
cyclotron	$\omega_s/2\pi \approx 154.0$ GHz	$(\gamma_c/2\pi)^{-1} \approx 0.08$ s	$\bar{n}_c = 1.3 \times 10^{-319}$
axial	$\omega_z/2\pi \approx 120$ MHz	$(\gamma_z/2\pi)^{-1} \approx 0.008$ s	$\bar{n}_z = 1.3$
magnetron	$\omega_m/2\pi \approx 330$ kHz	$(\gamma_m/2\pi)^{-1} \approx 10^{12}$ s	$\bar{n}_m = 1.3$

Table 2.1: Summary of frequencies, damping times and quantum numbers for the electron used in the experiment. The quantities are given at two fields, 0.75 T, where much of the SQUID demonstration work is done and 5.5 T, where g-factor measurements have been historically been performed.

result in an imperfect quadrupole field. While the measurement requires the precise measurement of the particle's oscillation frequencies, these frequencies are modified in an imperfect Penning trap.

The Brown-Gabrielse Invariance theorem [74] provides an exact quadratic relationship between the three motional eigenfrequencies of a charged particle in a Penning trap to its free space cyclotron frequency even in an imperfect trap,

$$\nu_c = \sqrt{\nu_c'^2 + \nu_z^2 + \nu_m^2}. \tag{2.24}$$

Brown-Gabrielse showed that the above relationship is exactly invariant with realistic misalignments of the magnetic and electric field axes and variations of the electrostatic potential from the pure quadrupole form. The invariance theorem allows us to precisely determine the free space cyclotron frequency, as required for the g-factor determination 2.6, through directly measurable trap eigenfrequencies.

2.3 Experimental Apparatus

The previous sections of this chapter have explored the ideal electron Penning trap. The actual implementation of the g-factor experiments of the electron and/or positron is discussed here. This apparatus is an entirely new system from that used in the 2023 electron g-factor measurement [6,42] and is purpose-built for the implementation of the *near*-quantum limited SQUID amplifier, detection of spin/cyclotron states via the relativistic mass shift [65], and measurement of the positron magnetic moments.

It includes two new Penning traps: an orthogonal and compensated closed endcap trap for the magnetic moment measurement (called the measurement trap or sometimes the precision trap) and an open endcap trap for the accumulation of positrons from a sodium-22 radioactive source (called the accumulation trap or sometimes the loading trap) before transferring to the measurement trap for the g-factor determination. These 10 mK traps are implemented on a purpose-built dilution refrigerator that rests directly on a 5.5 T cold-bore superconducting magnet at 4.2 K with a significantly reduced fridge field for the implementation of the SQUID. Finally, the entire apparatus sits on top of an active vibration isolation stage that mitigates the coupling of ambient vibration into the dewar top resulting in apparent magnetic field noise.

An overview of the entire experimental apparatus is shown in Figure 2.4. This section will describe each component of the system starting from the Penning trap working outwards.

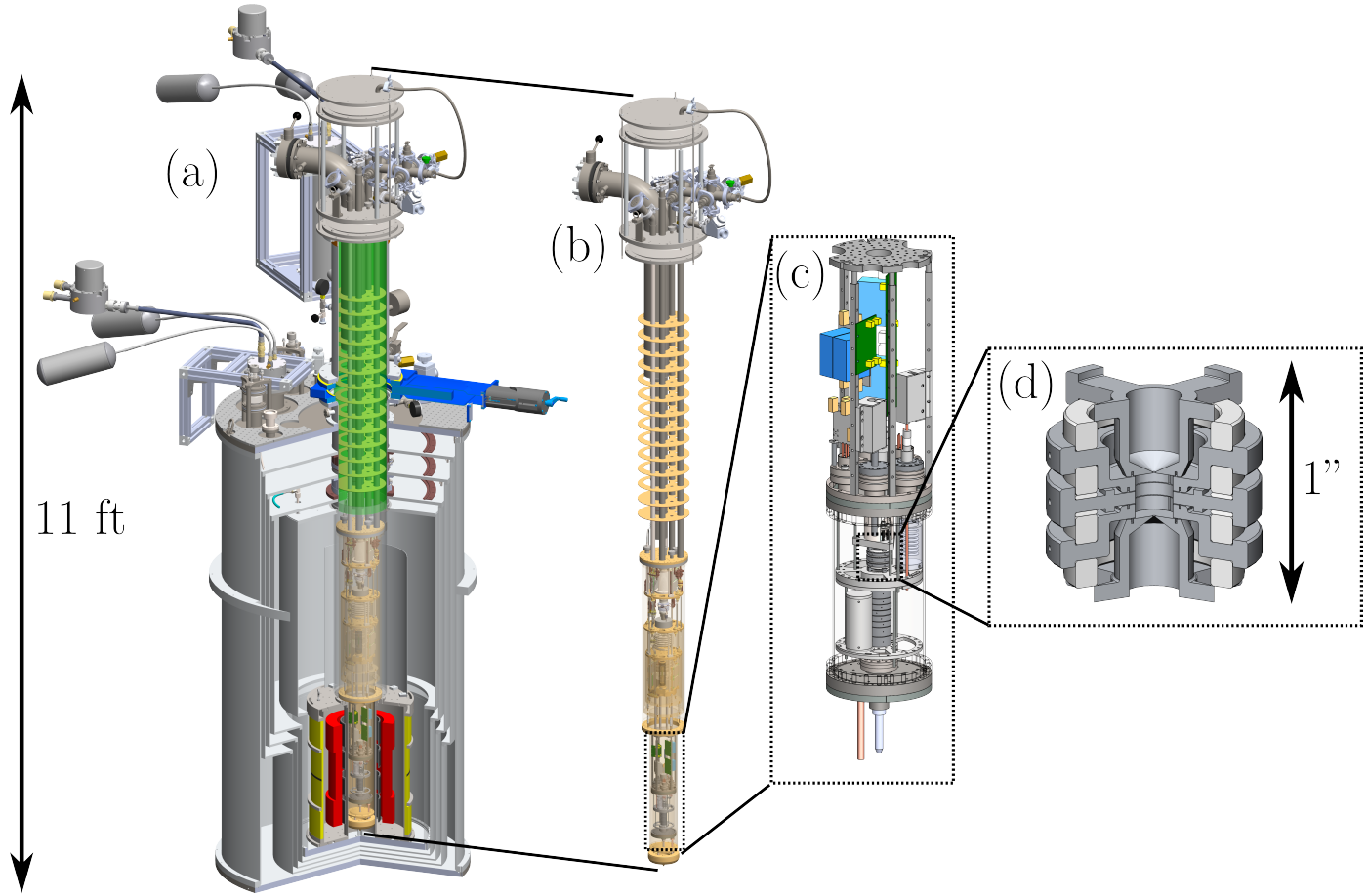

Figure 2.4: Overview of the entire experiment system. The measurement trap (d) sits inside a custom titanium vacuum enclosure (c) onto which critical filters, amplifiers, attenuators are mounted. The vacuum enclosure is fixed to the bottom of a dilution refrigerator (b) capable of achieving temperature < 10 mK. The 10 mK stages of the dilution refrigerator directly rests on top of a 5.5 T superconducting magnet at 4.2 K inside a liquid helium dewar.

2.4 The Designed Penning traps

2.4.1 The Measurement Trap

All quantum measurements of the electron magnetic moment measurements [6, 40, 75] have employed closed endcap cylindrical electron Penning traps. The resulting quantum cyclotron led to three increasingly accurate measurements of the electron magnetic moment in which systematic shift from the coupling of the electron to the trap cavity that confines it has become increasingly important. Closed endcap cylindrical Penning traps enabled these more precise measurements through (i) inhibition of spontaneous emission [70], which made the lifetime of the excited cyclotron state long enough to observed quantum jumps [60, 62]; and (ii) correction of the observed shifts in the measured magnetic moment due to the trap cavity [63, 64].

The major compromise from the earlier experiments utilizing a hyperbolic electrode geometry [58] was the reduction in the detection sensitivity as the harmonic region of the trap was reduced. While this has not limited previous measurements, improving the detection sensitivity enables faster readout and will lead to smaller magnetic bottles and eventually the relativistic bottle detection [65]. This new measurement trap is designed with the primary motivation of improving the detection efficiency of the trap while maintaining favorable cavity properties with the ultimate goal of achieving sufficient detection sensitivity to enable state detection via the relativistic mass shift [65].

Design Goals

The major design goals for the measurement trap are threefold:

1. improve the microwave cavity properties of the trap compared to the 2023 experiment

2. further improve detection efficiency by improving coupling to the trapped particle

3. enable better detection efficiency through a more harmonic trap

In addition to these primary design goals the traps described are constructed out of 99.999% purity silver and the spacers out of fused quartz to eliminate temperature dependent magnetic field variations due to nuclear paramagnetism [76]. Additionally, the traps are designed to be extremely modular for the easy swapping of traps, detection resonators, field emission points, and positron source.

Electrostatics of the Measurement Penning Trap

The designed trap is a five electrode closed endcap cylindrical Penning trap [59], as shown in Figure 2.5. The electrostatics of trap is determined by three dimensions: half of the height of the trap z_0, height of one compensation electrode z_c, and the radius of the trap ρ_0. The typical bias configuration is with the two endcaps grounded and the ring and compensation electrodes at potentials V_R and V_c respectively. The potential in this case is given by the superposition of the potential from the ring electrode and the compensation electrode:

$$V = V_R\phi_0 + V_c\phi_c, \tag{2.25}$$

where,

$$\phi_0 = \frac{1}{2}\sum_{k_{even}=0}^{\infty} C_k^0 \left[\frac{r}{d}\right]^k P_k(\cos\theta) \tag{2.26}$$

and,

$$\phi_c = \frac{1}{2}\sum_{k_{even}}^{\infty} \left[V_R\frac{\partial D_k}{\partial V_c}\right] \left[\frac{r}{d}\right]^k P_k(\cos\theta) \tag{2.27}$$

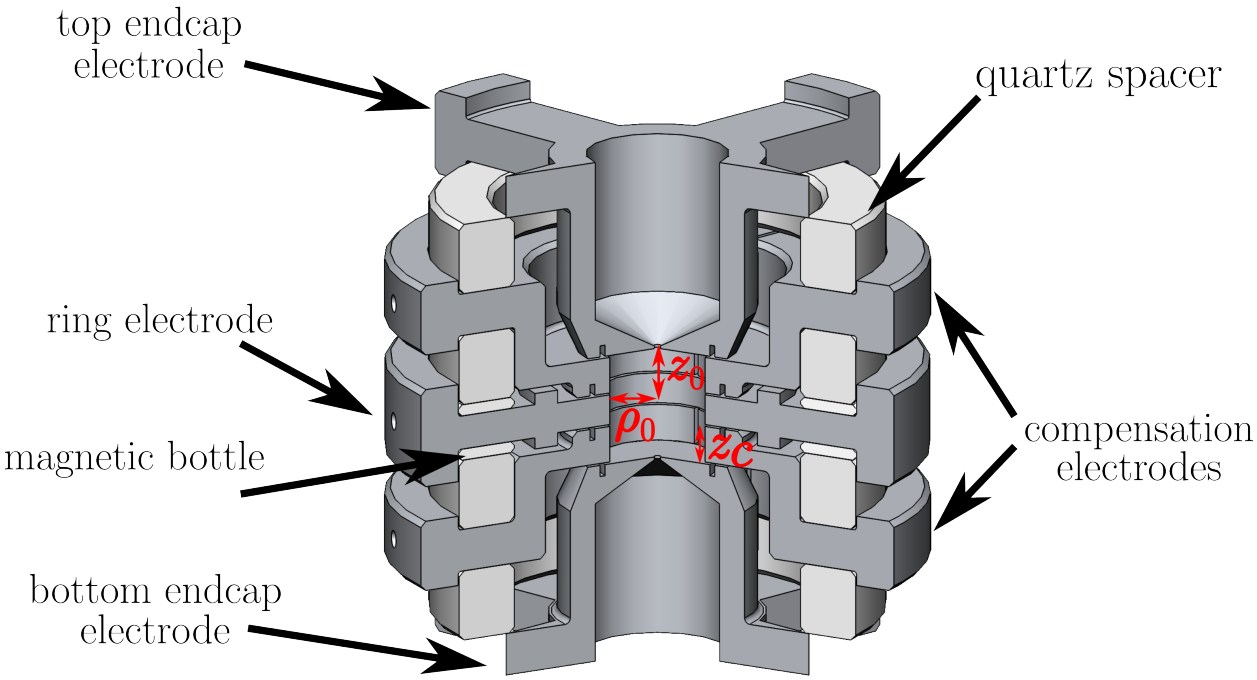

Figure 2.5: The new closed endcap cylindrical Penning trap. Five electrode trap that is orthogonal $\gamma = C_2/C_4 = 0$ and compensated $C_6 = 0$ when tuned.

where $d = \sqrt{1/2\,(z_0^2 + \rho_0^2)}$ and the expansion coefficient C_k^0 and D_k are given by [59],

$$C_k^0 = -\delta_{k2} + \frac{(-1)^{k/2}}{k!}\frac{\pi^{k-1}}{2^{k-3}}\left(\frac{d}{z_0}\right)^k \sum_{n=0}^{\infty} \frac{(-1)^{n+1}(2n+1)^{k-1}\cos^2\left[\frac{1}{2}\left(n+\frac{1}{2}\right)\pi z_c/z_0\right]}{J_0\left[i\left(n+\frac{1}{2}\right)\pi\rho_0/z_0\right]} \tag{2.28}$$

and,

$$D_k = \frac{(-1)^{k/2}}{k!}\frac{\pi^{k-1}}{2^{k-3}}\left(\frac{d}{z_0}\right)^k \sum_{n=0}^{\infty} \frac{(-1)^{n}(2n+1)^{k-1}2\sin^2\left[\frac{1}{2}\left(n+\frac{1}{2}\right)\pi z_c/z_0\right]}{J_0\left[i\left(n+\frac{1}{2}\right)\pi\rho_0/z_0\right]}. \tag{2.29}$$

The above equations can be combined to give the total potential at the center of the trap as,

$$V(\rho, z) = -V_R\left(\frac{z^2 - \rho^2/2}{2d^2}\right) - \frac{V_R}{2}\sum_{\substack{k=0 \\ \text{even}}} C_k\left(\frac{r}{d}\right)^k P_k(\cos\theta), \tag{2.30}$$

where the expansion coefficients are,

$$C_k = C_k^0 + D_k \left(\frac{1}{2} - \frac{V_c}{V_R} \right). \tag{2.31}$$

In a perfectly harmonic trap with $C_k = 0$ for $k > 2$, the axial frequency of the trapped particle is given by,

$$\omega_z = \sqrt{\frac{eV_R}{m_e d^2} (1 + C_2)}. \tag{2.32}$$

However, in a realistic trap with the trapped particle driven to some amplitude A, the axial frequency has amplitude dependence on the anharmonic contributions to the trapping potentials following the equation,

$$\omega_z \left(A^2 \right) \approx \omega_z \left[1 + \frac{3C_4}{4\left(1 + C_2\right)} \frac{A^2}{d^2} + \frac{15C_6}{16\left(1 + C_2\right)} \left(\frac{A^2}{d^2} \right)^2 \right] \tag{2.33}$$

The goal in designing the optimal trap is to select dimensions such that the trap remains harmonic at displacements from the trap center, that is, $C_k \to 0$, for $k > 2$. Alternatively, C_4 and C_6 can be tuned such that the amplitude dependent terms in Equation 2.33 cancel for a fixed amplitude. Since C_k depends on the voltage ratio V_c/V_R, and the trap dimensions ρ_0, z_0, and z_c, there are parameters that can be selected such that higher order contributions to the potential will vanish. For a five electrode trap, the C_4 and C_6 contributions can be canceled simultaneously, and I will outline how it is done in this implementation. Terms beyond C_6 can be canceled in traps with more than five electrodes [77, 78]. In reality, we minimize the coefficients of the amplitude dependent contributions in design but machining imperfections will result in deviations from the designed parameters. We then minimize these contributions by adjusting V_c while driving the particle at large amplitudes.

The relative trap dimensions determine C_k. In this implementation we take z_0 as a free parameter to be scaled and vary the ratios ρ_0/z_0 and z_c/z_0 to achieve the optimal electrostatic

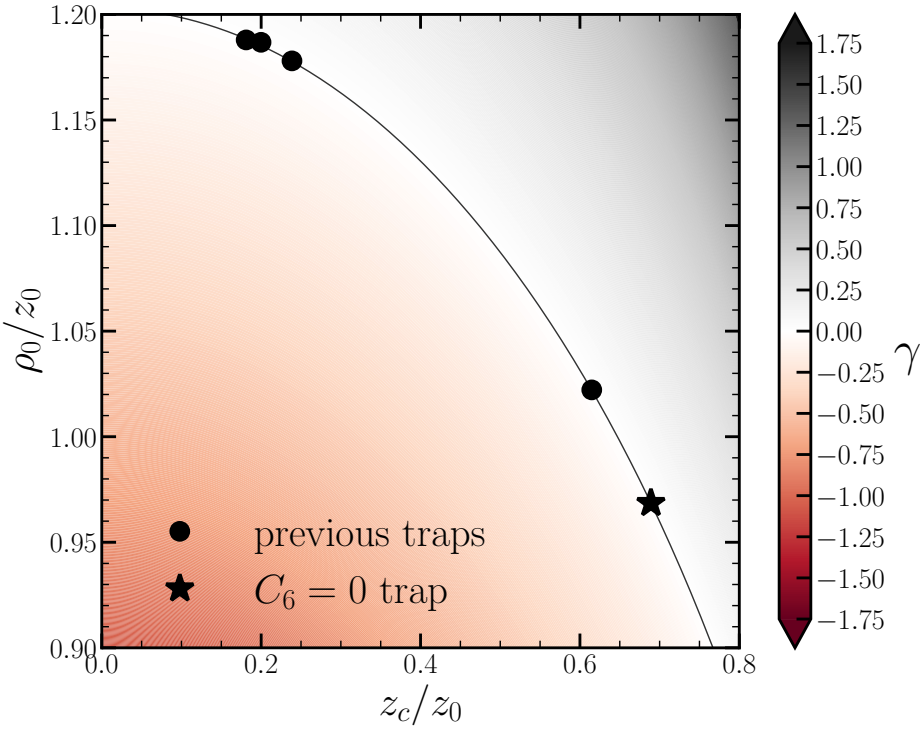

Figure 2.6: Orthogonality condition $\gamma = C_2/C_4 = 0$ plot for closed endcap Penning traps. While the orthogonality condition constrains z_0/ρ_0 and z_0/z_c, z_c/ρ_0 is unconstrained along the marked contour. We have utilized this freedom to satisfy the condition $C_6 = 0$ while $C_4 = 0$

potential. The dimension ratios ρ_0/z_0 and z_c/z_0 are found such that $\gamma = D_2/D_4$ is zero. This allows the the compensation electrode bias V_c can be varied with respect to the V_R to change C_4 but not C_2 [59]. Thus the anharmonicity of the trap can be tuned without changing the axial frequency. A trap that satisfies this condition is called orthogonal and the range of dimensions that satisfy the orthogonality condition $\gamma = 0$ are shown in Figure 2.6.

While the ratios ρ_0/z_0 and z_c/z_0 are now constrained by the orthogonality condition, the ratio z_c/ρ_0 can be varied while maintaining the prior conditions. The goal is now to select dimensions such that a tuning voltage ratio V_c/V_R can be found that simultaneously makes both C_4 and C_6 vanish. This equates to solving 2.31 for $C_4 = C_6 = 0$; therefore what

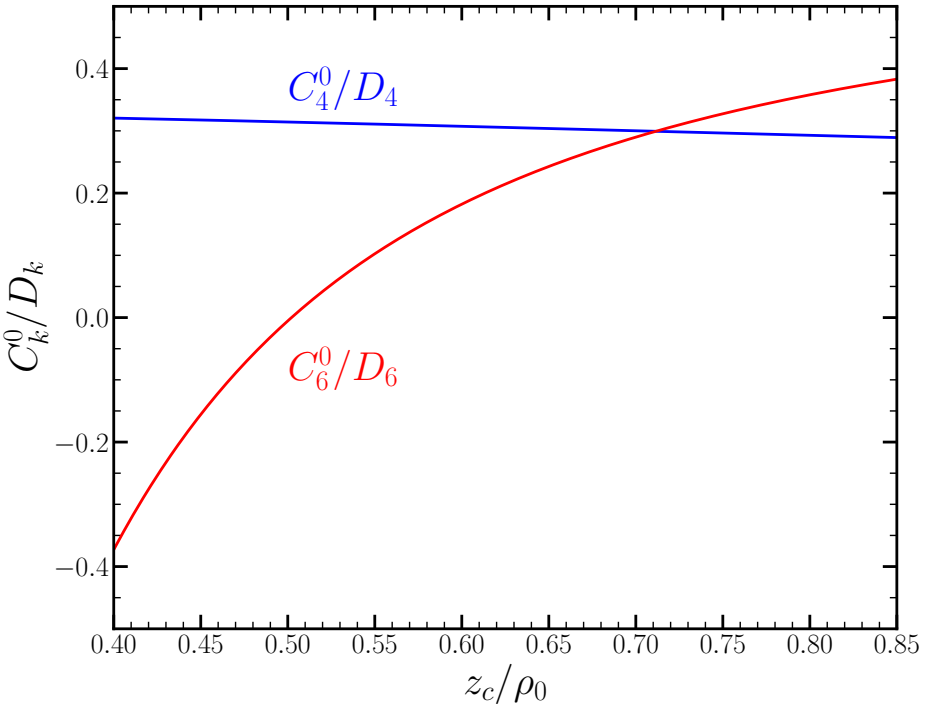

Figure 2.7: Parameter search for determining orthogonality and compensation for the closed endcap Penning trap. $C_4^0/D_4 = C_6^0/D_6$ where the lines intersect and therefore for these trap dimensions z_c/ρ_0, both C_4 and C_6 can be tuned to zero for the same bias ratio V_c/V_R

must be determined is the ratio of z_c/ρ_0 that makes $C_4^0/D_4 = C_6^0/D_6$. Figure 2.7 shows the parameter scan to determine these optimal dimensions.

The dimensions ratios that achieve these conditions for the five electrode closed endcap cylindrical Penning are $\rho_0/z_0 = 0.9684$, $z_c/z_0 = 0.6892$, and $z_c/\rho_0 = 0.7117$. The calculated optimal voltage tuning ratio to cancel both the 4th and 6th order contributions to the potential is $V_c/V_R = 0.7993$. The key trap dimension parameters, along with other key parameters are summarized in Table 2.2.

The expansion coefficients C_k^0 and D_k for the designed trap along with the combined expansion coefficient C_k when the trap is tuned to the optimal voltage ratio are summarized in Table 2.3. It is important to note that the added benefit of canceling the 6th order contribution only becomes relevant when the trapped particle is driven to a large axial

parameter	**value**
half-height of trap: z_0	2500 μm
radius of trap: ρ_0	2421 μm
compensation electrode height z_c	1723 μm
image charge parameter on endcap: c_1	0.630
antisymmetric bias parameter: c_3	0.492
calculated optimal voltage ratio: V_c/V_R	0.7993

Table 2.2: Key design parameters for the designed closed endcap Penning trap

amplitude, otherwise the 4th order contribution dominates.

Furthermore, although we have designed a trap to cancel both C_4 and C_6 simultaneously, the limit on how small C_6 can be tuned will be determined by the achieved machining imperfection in dimensions. As shown in [42], we can estimate the realistic value of C_6 achievable with typical machining tolerances by varying the dimensions of trap by 25 μm (four times larger than the measured machining tolerance) and recalculating the achieved C_6 when tuned. With this procedure, we estimate that the $|C_6| < 4.6 \times 10^{-3}$, a factor of 20 smaller than the trap used in the 2023 g-factor measurement ($C_6 = -0.1$). This improvement in trap design should therefore enable a factor of 20 times better axial frequency resolution through its driven motion. At the time of writing we have not demonstrated this improvement in the driven detection but have observed enhanced dip detection where orthogonality is less relevant as the axial excitation is small.

Improved Detection Efficiency

Significant efforts have gone into improving the detection efficiency in this iteration of the Penning trap for the electron magnetic moment. To contextualize the specific improvements made, we will first discuss how the motion of the electron is detected and its state is read out.

In the electron magnetic moment experiment, the axial motion of the particle is the only

parameter	value	parameter	value when tuned
C_2^0	0.0453	C_2	0.0453
D_2	0.0000		
C_4^0	-0.2582	C_4	0
D_4	-0.8628		
C_6^0	0.1467	C_6	0
D_6	0.4901		
C_8^0	-0.0743	C_8	-0.0416
D_8	-0.1092		

Table 2.3: Calculated expansion electrostatic potential expansion coefficients for the closed endcap cylindrical Penning trap. The calculated expansion coefficient when tuned to the optimal voltage tuning ratio $V_c/V_R = 0.7993$ is also given.

probe of its motion. The cyclotron and spin frequencies are ~ 150 GHz, and therefore cannot be efficiently read out at single electron sensitivities. The magnetron motion, is *cooled* to an effectively stable orbit ($\tau_m > 10^{12}$ s) but is in an unstable equilibrium. Any dissipative forces used for detection would damp this motion increasing the magnetron radius. Only the axial motion is directly measured. By coupling it to the spin and cyclotron motions, transitions in those states can be inferred from corresponding shifts in the axial frequency.

The electron's axial oscillation induces an image charge current in the trap endcap. This small induced current is dropped through a large effective resistor producing a small voltage signal that is amplified through a cryogenic detector chain to a signal that is measurable at room temperature. The equations of motion of the particle are solved in detail elsewhere [42, 68]. We summarize the relevant results here.

The induced current on the endcap electrode is,

$$I = \frac{ec_1}{2z_0}\frac{dz}{dt}, \tag{2.34}$$

where c_1 is called the asymmetric expansion coefficient or sometimes called the image charge parameter. For the designed trap $c_1 = 0.630$, slightly smaller than the previous Penning

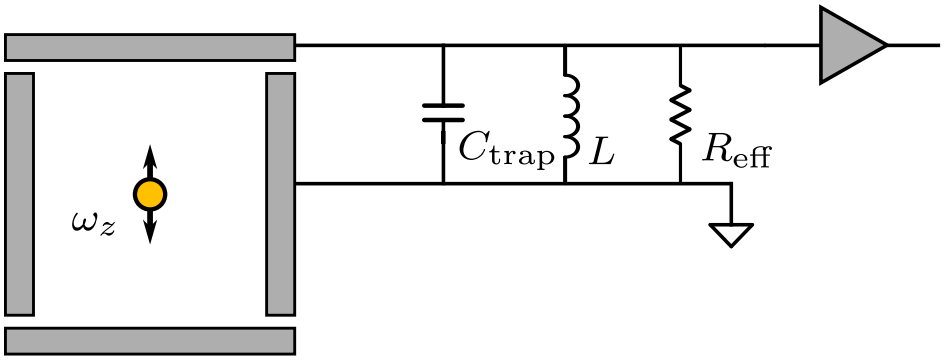

Figure 2.8: Equivalent LCR circuit used to measure the induced image charge current from the oscillating electron.

trap where $c_1 = 0.784$. The effective resistance R_{eff}, that this current is dropped over arises from an LCR resonant circuit tuned to the axial frequency of the particle. The C in this circuit is the parasitic capacitance between the endcap electrode used for detection and ground, primarily through the nearest compensation electrode. The L is from a low loss quarter wave helical resonator [79] made from a high purity silver wire and placed as close as possible to the detection electrode. This detection circuit is shown in Figure 2.8.

The resonant frequency of this parallel LCR circuit is,

$$\omega_0 = \frac{1}{\sqrt{LC}}, \tag{2.35}$$

and the effective impedance of the circuit is given by,

$$Z(\omega) = \left(i\omega C + \frac{1}{R_{\text{eff}}} + \frac{1}{i\omega L} \right)^{-1}, \tag{2.36}$$

where R_{eff} is the effective resistance of the circuit on resonance where the reactances of the inductor and capacitor cancel and the electron sees a purely resistance impedance,

$$R_{\text{eff}} = \frac{Q}{\omega_z C} = Q\omega_z L, \tag{2.37}$$

where Q is the quality factor of the LCR circuit. The electron signal is $V = IR$, and the primary source of noise is the Johnson-Nyquist noise which scales as temperature. Therefore, to improve SNR for the single electron signal, the handles are c_1, z_0, Q, and the temperature of the circuit T. While c_1 is set by the relative trap dimensions and has been fixed by the orthogonality and compensated conditions, all other parameters have been improved on.

The temperature of the LCR circuit has been significantly reduced through the implementation of a non-dissipative *near*-quantum noise limited SQUID amplifier. This is discussed in detail in Chapter 3. The size of this trap, i.e. $z_{0,\text{new trap}} = 2500$ μm has been reduced compared to the old trap, $z_{0,\text{old trap}} = 3833$ μm. This change has improved the electron signal by a factor of about 1.5.

The last factor enhanced is the Q of the LCR resonant circuit. As described in [80], the Q of a quarter wave helical resonator scales like the resistance of the shield and coil material, the diameter of the shield D, and the inductance of the coil L. We have chosen high purity silver for coil and shield materials to achieve the lowest possible resistance. The diameter of the shield is confined by the largest possible resonator that can be fit in the trap vacuum enclosure. A larger resonator can be constructed and placed outside of the trap chamber but at the expense of signal loss due to a long path between detection electrode and the resonator. The largest possible resonator that could be constructed and fit in the vacuum enclosure has $D = 1$ inch.

We have selected the resonant frequency of particle and detection circuit to be centered at 120 MHz to be at the center of the maximum gain bandwidth of the SQUID amplifiers. With this constraint, the only path to improving L is through reducing the trap parasitic capacitance. In the previous system, the trap capacitance was ~ 13 pF [41]. Significant design changes were made and evaluated with finite element methods using Ansys Electrostatics Software to reduce the trap capacitance from 13 pF to ~ 7 pF. This iterative design process is shown in Figure 2.9. We estimate that through these changes we were able to increase the

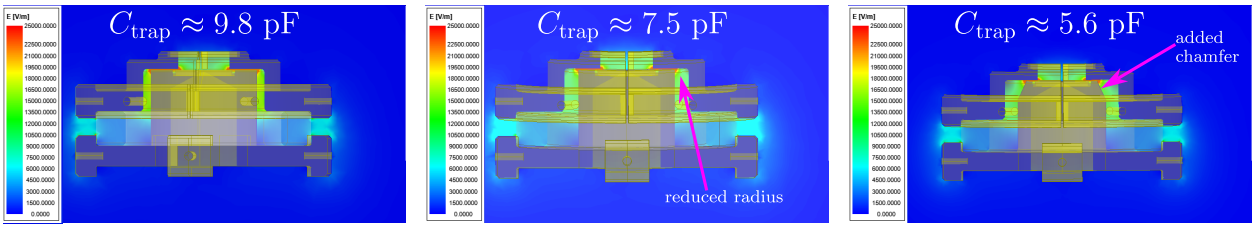

Figure 2.9: Finite element analysis driven capacitance reduction of the trap's parasitic capacitance. From the first to second iteration the outer radius of the endcap electrode was decreased reducing the C_{trap} by 2 pF. The added chamfer in the third iteration, along with other smaller modifications not highlighted in the figure, resulted in a calculated $C_{\text{trap}} \approx 5.8$ pF. In practice this capacitance is measured to be ~ 6.8 pF, presumably from other paths of stray capacitance.

L of the LCR circuit by a factor of ~ 2.

In the installation of the resonator to the resonator to the trap system we observed a degradation of the Q when the trap DC bias lines were connected. These losses were attributed to radiation loss from the long path between these leads and the DC bias filter circuits. We minimized this loss through adding large resistors on the DC bias lines as close as possible to the trap electrodes.

Altogether, with these improvements we achieved $Q \approx 1400$ at cryogenic temperatures, and an effective parallel resistance $R_{\text{eff}} = 270$ kΩ at 200 mK. To completely quantify the improvement in the signal to noise achieved in this apparatus we consider the electron's axial damping rate γ_z. The dissipation of the induced image current in the tuned circuit damps the electron's axial motion with a rate given by [68],

$$\gamma_z = \left(\frac{ec_1}{2z_0}\right)^2 \frac{R_{\text{eff}}}{m_e} \tag{2.38}$$

With the parameters realized in this apparatus we calculate that $\gamma_z/2\pi \approx 20$ Hz. This is a factor of 4 improved on the 2023 g-factor measurement and about a factor of 20 improved on the 2008 g-factor measurement.

Microwave Cavity Properties

The metal walls of the measurement trap form a microwave cavity satisfying the boundary condition $E_{\parallel} = B_{\perp} = 0$. For the trap sizes typically used for the electron experiment, the fundamental mode of this trap-cavity is ~ 20 GHz, far below the typical cyclotron frequency used in the measurement. Therefore, the trap itself modifies the density of radiation modes that the electron's cyclotron motion can couple to away from its free space value [63, 64]. The result is two fold:

1. inhibited spontaneous emission off-resonance and enhanced spontaneous emission on-resonance with cavity modes that couple to the cyclotron motion

2. a shift in the measured cyclotron in the trap $\bar{\nu}_c^{\mathrm{cav}}$ from the free space value value needed in equation 2.6

Inhibited spontaneous emission is advantageous, since without it we would not have sufficient time between excitation and decay to observe quantum jumps. However, the cavity-induced shift of the cyclotron frequency constitutes a dominant systematic that must be carefully evaluated and presently limits the ultimate precision of the experiment (see Chapter 4). To mitigate this, the trap geometry was changed from the hyperbolic form to the more calculable cylindrical geometry in the modern era of the electron g-factor measurement. Alternative geometries, such as the spherical trap and the hyperbolic trap, have also been considered [81, 82].

A cylindrical cavity of radius ρ_0 and height $2z_0$ imposing boundary conditions $E_{\parallel} = B_{\perp} = 0$ allows two classes of electromagnetic standing waves: *transverse-electric*, or TE modes, and *transverse-magnetic*, or TM modes. The electric and magnetic fields for these modes are straightforwardly derived elsewhere [83] and their characteristic frequencies are

given by,

$$\omega_{mnp}^{\mathrm{TE}} = c\sqrt{\left(\frac{x'_{mn}}{\rho_0}\right)^2 + \left(\frac{p\pi}{2z_0}\right)^2}, \tag{2.39}$$

for TE modes, and,

$$\omega_{mnp}^{\mathrm{TM}} = c\sqrt{\left(\frac{x_{mn}}{\rho_0}\right)^2 + \left(\frac{p\pi}{2z_0}\right)^2} \tag{2.40}$$

for TM modes, where x_{mn} is the nth zero of the order-m Bessel function ($J_m(x_{mn}) = 0$), and $x'_m n$ is the nth zero of the derivative of the order-m Bessel function ($J'_m(x'_{mn}) = 0$). The mode indices m, n, and p specify the nodal structure: $m = 0, 1, 2, \ldots$ gives the number of nodes in ϕ over π radians, $n = 1, 2, 3, \ldots$ gives the number of radial antinodes in $E\phi$, and $p = 1, 2, 3, \ldots$ for TE modes or $p = 0, 1, 2, \ldots$ for TM modes gives the number of axial antinodes.

The modes that couple to the cyclotron motion are those with non-zero transverse ($\hat{\phi}$ and $\hat{\rho}$) electric field components close to the trap center. These are the $\mathrm{TE}_{1n(\mathrm{odd})}$ and the TM $_{1n(\mathrm{odd})}$ modes.

A secondary microwave cavity design consideration are modes with an electric field gradient that scales like $z\hat{\rho}$ or $\rho\hat{z}$, or modes with a magnetic field independent of z or ρ. These are the $\mathrm{TE}_{1n(\mathrm{even})}$ and the TM $_{1n(\mathrm{even})}$ modes. These modes facilitate the coupling of the cyclotron and axial motions and can be utilized for cavity assisted sideband cooling. In this scheme, energy from the axial motion can be transferred to the cyclotron motion to enable even lower axial temperatures and therefore a more precise measurement.

From the discussion on the design of the orthogonal and compensated trap, we have fixed the dimension ratios ρ_0/z_0 , z_c/z_0, and z_c/ρ_0, and have left z_0 as a free parameter. While the distribution of the microwave mode structure cannot be modified since the relative dimensions has been fixed, the frequency interval can be adjusted through changing z_0. To reduce the cavity shift systematic a smaller cavity is desirable as the particle can couple to

far fewer modes leading to a smaller correction. That is,

$$\Delta\frac{g}{2}\Big|_{\text{cav}} \propto (\text{ interval of modes })^{-1} \propto z_0 \tag{2.41}$$

The limit on how small the trap can be made comes from the machining capability of our trap fabricators. We take the smallest achievable electrode height to be what has been achieved in previous traps, that is $z_c = 766$ μm in the trap used for the 2006, 2008, and 2023 g-factor measurements. We have taken the more conservative approach of setting the height of the trap $z_0 = 2500$ μm, which sets the height of the smallest electrode $z_R = 2(z_0 - z_c) = 1550$ μm. This allows us to produce a trap with the smallest electrode twice the size of the previous traps while reducing the trap size by about 40%.

The calculated cavity mode structure in this new trap cavity is shown in Figure 2.10. Contrast this new trap mode structure with the trap used in the 2006, 2008, and 2023 measurements, Figure 2.11. The interval between modes is improved by a factor of ~ 3 providing many ideal frequencies for a future g-factor measurement. Additionally, note that the first mode that couples to the electron's cyclotron motion is TE_{111} at 47 GHz in this trap compared to TE_{111} at 27 GHz in previous traps. This opens the door to a measurement of the magnetic moment below the relevant "cut-off" frequency of the trap, where the contribution of the microwave cavity shift is expected to be minimized. However, note that in such a measurement, the modified cyclotron lifetime will be very long. This is advantageous for averaging and increasing the the measurement precision but makes the measurement challenging without a fast mechanism to drive the particle back to the ground state after excitation.

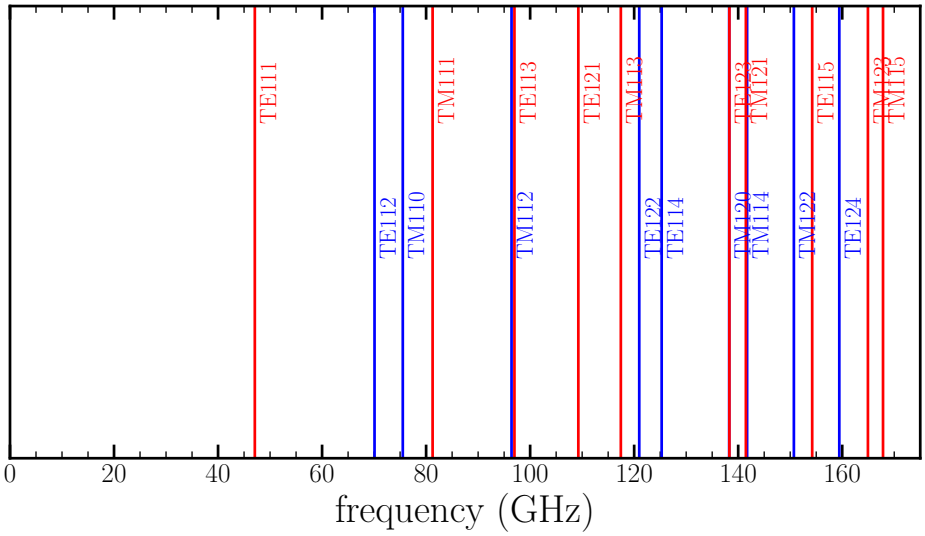

Figure 2.10: Microwave mode structure in the new orthogonal and compensated closed endcap Penning trap. Red lines are modes that couple to the cyclotron motion of a trapped electron at the center of the trap and blue lines are modes with electric field structure that can be exploited for cavity-assisted axial sideband cooling

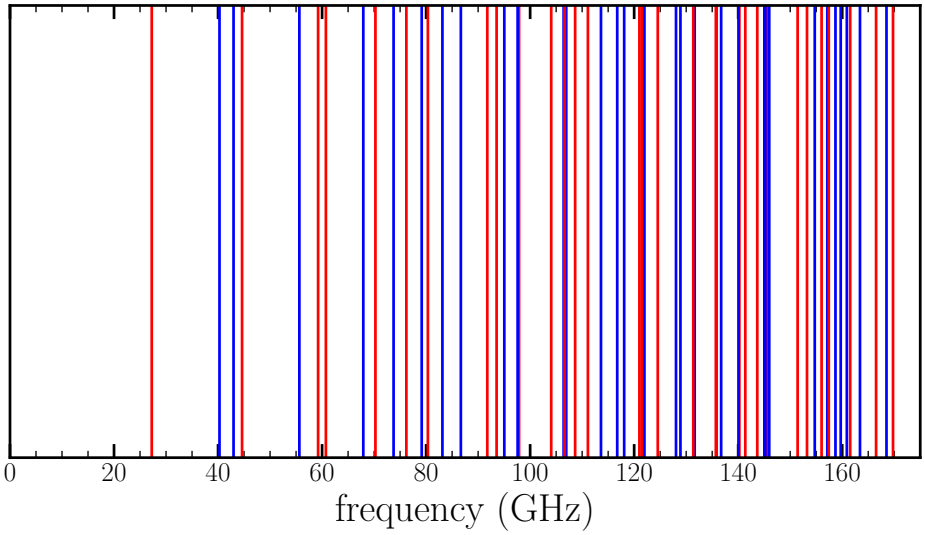

Figure 2.11: Microwave mode structure in the trap used in previous g-factor measurement. Red lines are modes that couple to the cyclotron motion and blue lines are modes that can be used for cooling. The mode labels have been omitted due for clarity.

2.4.2 The Accumulation Trap

A secondary goal of the designed apparatus is to measure the positron's magnetic moment at a precision that matches the measured electron's magnetic moment. While electrons are easily loaded from a field emission point point, centered on small on-axis holes of the trap, loading positrons is more complicated. We load positrons from a radioactive Na-22 source that undergoes the decay process,

$$^{22}_{11}\mathrm{Na} \longrightarrow {}^{22}_{10}\mathrm{Ne} + e^{+} + \nu_e \tag{2.42}$$

While a fraction of the emitted high energy positrons from this process can be slowed down with the use of a single crystal moderators to eV energies [84], the confinement challenge still remains. If a charged particle can enter an electrostatic trapping region, it can escape that region in the absence of any damping mechanism. Furthermore, damping even meV positrons in typical trap sizes is incredibly challenging as the timescale for damping would be less than a microsecond.

Similar to what has been established by predecessors in our group [85–87], we aim to capture positrons through field ionization of strongly magnetized Rydberg positronium. Rydberg positronium is produced through passing the emitted positrons through a 2 μm single crystal tungsten foil (100) that acts as a transmission moderator. These high n state positronium atoms are easily ionized in modest electric fields such that a electron/positron can be confined in an electrostatic well while the paired positron/electron carries away the excess energy. This mechanism allows us to accumulate both positrons and electrons from the radioactive source into the loading trap.

We have designed and fabricated a new positron accumulation trap (2.12) for the ionization and collection of these positrons, and the efficient transfer to the measurement trap for the g-factor measurement. The designed apparatus is similar to that described in [87]

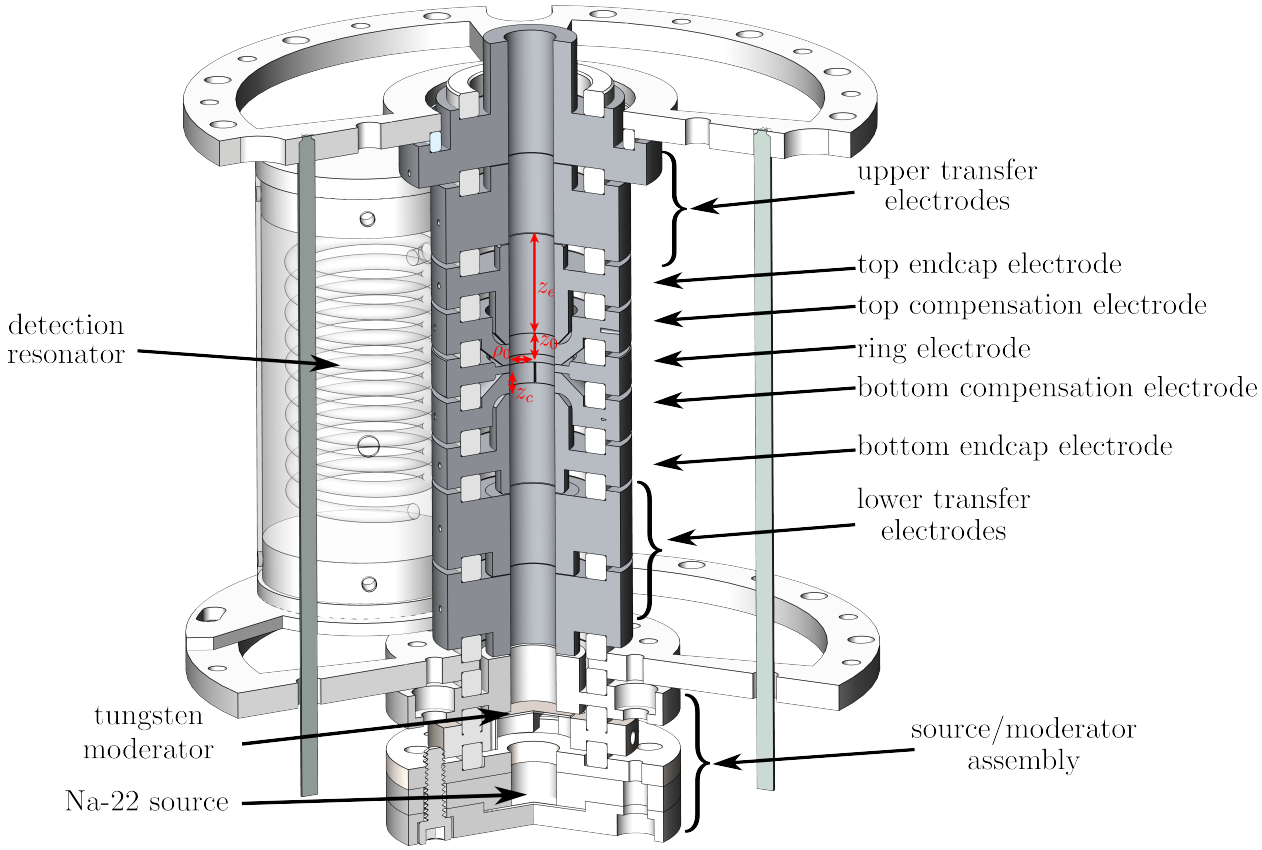

Figure 2.12: New positron accumulation trap and source moderator assembly. The positron accumulation trap is an orthogonal and compensated open endcap Penning trap with additional transfer electrodes for shuttling of positrons to the measurement trap placed above this trap. The source/moderator assembly is designed to be easily demountable for fast moderator treatment. The entire system is modular and is designed to be attached on to the base of the measurement trap.

with two major differences. First, we design and implement an open endcap orthogonal and compensated Penning trap. The open endcap Penning trap allows more access for the accumulation of positrons from the radioactive source before transfer into the closed endcap trap used for precision measurements. The design principle followed here is identical to that described for the measurement trap and key design equations are derived in [88]. We will

only summarize the electrostatic results here.

Near the center of the trap the potential is given as,

$$V(\vec{r}) = -\frac{V_R}{2} \sum_{\substack{k=2 \\ \text{even}}}^{\infty} \bar{C}_k \left(\frac{r}{d}\right)^k P_k(\cos\theta) \tag{2.43}$$

where the expansion coefficients are given as

$$\bar{C}_k = \bar{C}_k^{(0)} + \bar{D}_k \left(\frac{1}{2} - \frac{V_{\text{comp}}}{V_R}\right) \tag{2.44}$$

and for the open endcap Penning trap the coefficients are given by

$$\bar{C}_k^{(0)} = \frac{(-1)^{k/2}}{k!} \frac{\pi^{k-1}}{2^{k-3}} \left(\frac{d}{z_0 + z_e}\right)^k \sum_{n=0}^{\infty} (2n+1)^{k-1} \frac{A_n^{(c)}}{J_0\left[\left(n+\frac{1}{2}\right)\pi\rho_0/\left(z_0+z_e\right)\right]} \tag{2.45}$$

and

$$\bar{D}_k = \frac{(-1)^{k/2}}{k!} \frac{\pi^{k-1}}{2^{k-3}} \left(\frac{d}{z_0 + z_e}\right)^k \sum_{n=0}^{\infty} (2n+1)^{k-1} \frac{A_n^{(d)}}{J_0\left[\imath\left(n+\frac{1}{2}\right)\pi\rho_0/\left(z_0+z_e\right)\right]} \tag{2.46}$$

where

$$A_n^{(c)} = \frac{1}{2}\left((-1)^n - \sin\left[\frac{\left(n+\frac{1}{2}\right)\pi z_0}{z_0+z_e}\right] - \sin\left[\frac{\left(n+\frac{1}{2}\right)\pi\left(z_0-z_c\right)}{z_0+z_e}\right]\right) \tag{2.47}$$

and

$$A_n^{(d)} = \sin\left[\frac{\left(n+\frac{1}{2}\right)\pi z_0}{z_0+z_e}\right] - \sin\left[\frac{\left(n+\frac{1}{2}\right)\pi\left(z_0-z_c\right)}{z_0+z_e}\right]. \tag{2.48}$$

The only new parameter appearing here that was not in the equations for the closed endcap traps is z_e which is the endcap electrode height.

The design principle is summarized in Figure 2.13. and key dimensional and trapping parameters for this trap are summarized in Tables 2.4 and 2.5.

The orthogonal and compensated Penning trap is implemented to improve the sensitivity

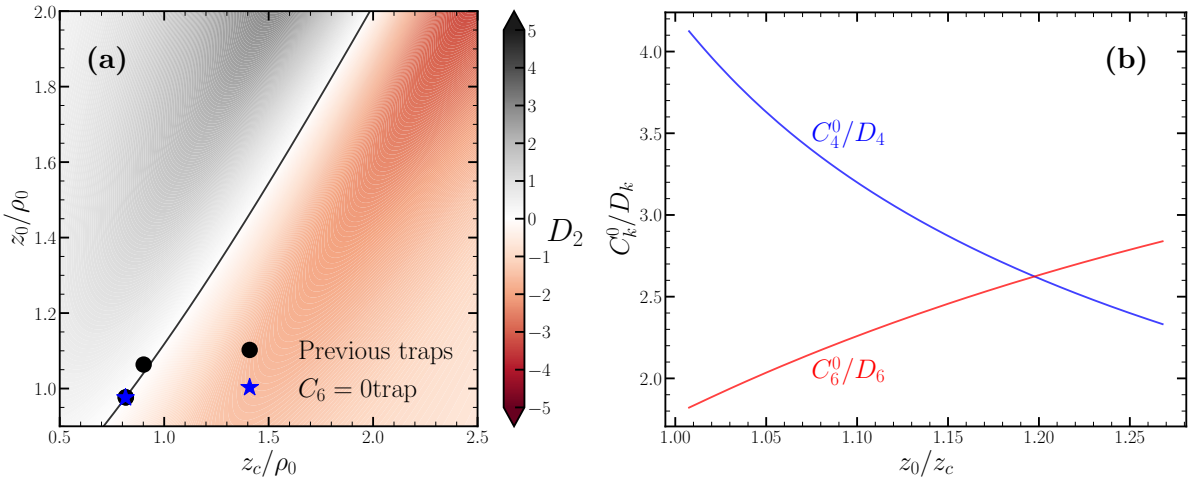

Figure 2.13: (a) Design principle: as in the measurement trap, dimensions are scaled to the chosen parameter ρ_0, set equal to the measurement trap radius. Unlike the measurement trap, the conditions of orthogonality and compensation have been established in prior designs. (b) Orthogonality and compensation plots for a closed-endcap Penning trap. At the intersection, $C_4^{(0)}/D_4 = C_6^{(0)}/D_6$, allowing both C_4 and C_6 to be tuned to zero with a single compensation bias.

of the trap to small number of positrons from a weak radioactive source (about 50 μCi at the time of installation) in a hermetically sealed capsule. While in Fogwell's design [87], the source is placed on a retractable stage to for storage when not in use, we sought to simplify the design through placing the source and moderator assembly inside of the trap vacuum enclosure. During the fabrication and commissioning of the system, direct loading of electrons and positrons were observed from the radioactive source. In our design, this direct loading would present a major challenge and led to a redesign of the source and moderator assembly such that source is positioned off access to the loading holes of the measurement trap. The 2.5 mm circular active area of the source is positioned 2 mm off-axis to the trap. With the source positioned about $\sim$ 90 mm away from the access hole, direct loading would require a misalignment of the magnetic field axis and the trap axis on order 1°.

Despite these efforts, we still observe direct loading from the source at a rate of 1 electron every 2-3 hours. We expect that a 1° misalignment is unlikely and hypothesize that the load-

parameter	**value**
half-height of trap: z_0	3089 μm
radius of trap: ρ_0	3165 μm
compensation electrode height: z_c	2578 μm
endcap electrode height: z_e	12000 μm
image charge parameter on endcap: c_1	0.3346
antisymmetric bias parameter on endcap : c_3	0.2202
calculated optimal voltage ratio: V_c/V_R	0.8813

Table 2.4: Orthogonality Parameters for open endcap Penning Trap.

parameter	**value**	**parameter**	**value when tuned**
C_2^0	0.5450	C_2	0.5450
D_2	0.0000		
C_4^0	-0.2120	C_4	0
D_4	-0.5558		
C_6^0	0.1638	C_6	-0.0002
D_6	0.4299		
C_8^0	-0.0197	C_8	0.0271
D_8	-0.1228		

Table 2.5: Orthogonality Parameters for open endcap Penning Trap when tuned $V_c/V_R = 0.8813$

ing mechanism must be either from gammas directly from the source or from the annihilation of positrons from the source traveling through the trap walls and either ionizing residual gas molecules in the trap directly or from pair creation from these high energy gammas.

At the time of writing, the loading mechanism is being investigated and efforts are underway to mitigate it. If the direct loading cannot be stopped in this scheme then, the modular trap assembly is designed such that the position of the accumulation and measurement trap can be swapped with minimal change, and a retractable source mechanism can be implemented.

2.5 New Dilution Refrigerator and Magnet System

A significant portion of this thesis work has gone into the commissioning of a new apparatus delivered in June, 2021 for the implementation of the newly designed and fabricated Penning traps and the implantation of the *near*-quantum limited SQUID amplifier. The major design change from previous systems is a superconducting solenoid with strong fringe field cancellation that makes it possible to implement the SQUID amplifier close to the Penning trap. This magnet is detailed in 3.3.1.

Additionally, for the implantation of the SQUID, the length of the dilution refrigerator was extended significantly such that the SQUID could be placed at the coldest part of the fridge, the mixing chamber, but still be sufficiently far away from the strong magnetic field.

Furthermore the new system has several operability improvements:

1. A large gate valve for minimizing helium loss during fridge insertion
2. Pulsed tube refrigerator cooled radiation shields instead of a liquid nitrogen dewar/shield
3. Joule-Thomson stage in lieu of a 1 K pot

These improvements will be discussed in detail in the following sections.

2.5.1 Modular Trap Vacuum Chamber and Tripod Region

In this experiment, we used a slightly modified version of the trap chamber redesigned by Fan in [42] (Figure 2.14). The new trap chamber is machined from Grade 2 titanium to reduce temperature dependent magnetic field fluctuations from nuclear paramagnetism [76]. The new design emphasizes modularity with non-custom parts to enable fast troubleshooting and improve cycle time. DC trap biases that were fed through individually brazed feedthroughs in previous iterations are replaced by a design that uses standard 8-pin 1.33 inch non-magnetic

titanium conflat feedthroughs. RF drives for both traps are also fed through this feedthrough while the RF detection line is fed through a custom brazed shielded silver feedthrough that is fabricated in house.

The standard conflat flanges seal the trap enclosure with copper gaskets. All other vacuum seals are made with indium. The bottom of the vacuum enclosure is fitted with an annealed copper tube for pumping out. After pumping the chamber for 24 hours, the chamber is sealed to atmosphere by *pinching-off* the soft copper pump out port with a specialized tool. Once *pinched-off*, there is no active pumping on the system and when cooled to cryogenic temperatures. The vacuum in the chamber was measured to surpass 5×10^{-17} Torr [89, 90] and we estimate that it is $\sim 10^{-30}$ Torr.

Both accumulation and measurement traps are assembled independently and sandwiched between two silver plates. The detection resonator for each trap system is mounted to each of these plates forming two modular trap systems that can be easily mounted and/or demounted from the trap vacuum enclosure. The field emission point used for loading electron(s) into the measurement trap is aligned with the trap axis and placed above the measurement trap. The source and moderator assembly is an independent sub-system that can be quickly mounted or demounted to the bottom of the accumulation trap.

The vacuum enclosure is mounted on to a silver tripod that is fabricated and assembled in house. During typical operation, we measure the temperature at the top of this silver tripod reaching temperatures below 10 mK with no heat load. This "tripod region" houses critical cold DC filters for biasing the trap, cold attenuators for driving the particle's motion, and an high electron mobility transistor (HEMT) for detecting the motion of electrons/positrons in the accumulation trap. The SQUID amplifier for detecting the motion of the electron in the measurement trap is mounted to the mixing chamber above.

The full wiring diagram including filters, attenuators, and amplifiers mounted at warmer stages is given in Figure 2.15. DC lines are heavily filtered to maintain voltage stability

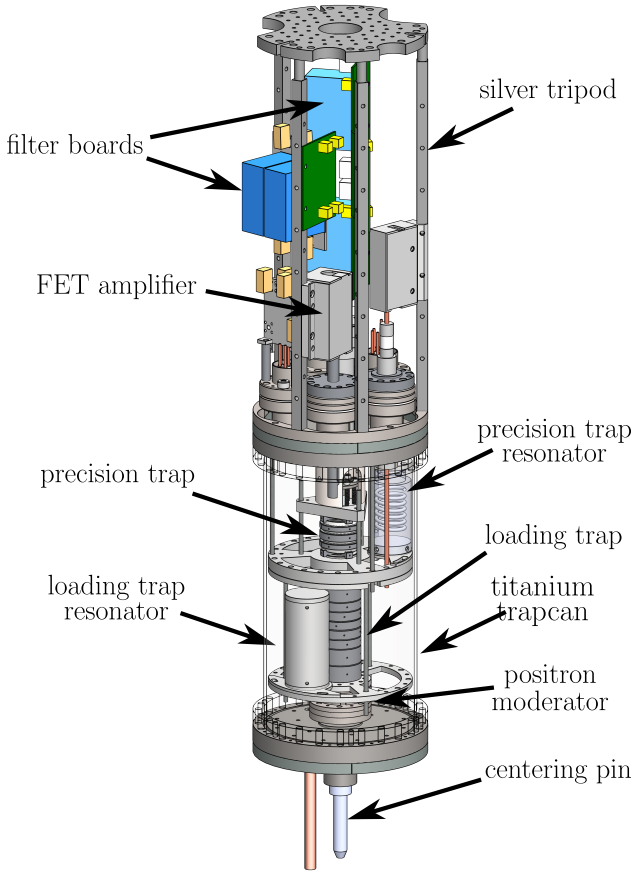

Figure 2.14: Schematic of titanium trap vacuum chamber and silver tripod. The trap chamber houses the accumulation trap, measurement trap, both detection resonators, and the source/moderator assembly. Critical RF drive and DC electronics are mounted to the silver tripod and cooled to dilution refrigerator temperatures.

of the trap, in particular the ring electrodes, to achieve high axial frequency stability. RF drive lines are heavily attenuated cryogenically to suppress room temperature Johnson noise leakage down to the trap. The anomaly/axial drive lines has -35 dB cold attenuation from fixed attenuators and $\sim$ 12 dB attenuation from cold stainless steel micro-coax lines while the magnetron *cooling* drive line (or SB drive line) has -50 dB cold attenuation from fixed attenuators and $\sim$ 12 dB attenuation from cold micro-coax. Both of these are above the $\sim$ 45 dB attenuation needed to suppress the room temperature Johnson noise. The two

stage HEMT detection chain for the accumulation trap is required to provide sufficient gain to amplify the Johnson noise resonance circuit from the ultra-low dilution refrigerator temperature to above the room temperature noise floor. The precision trap detection chain is a three amplifier chain with enough gain to amplify the noise resonance from 10 mK to above the room temperature Johnson noise and is explored in detail in 3.

2.5.2 Dilution Refrigerator

The trap vacuum chamber and tripod are mounted onto the mixing chamber of our custom dilution refrigerator constructed by JANIS ULT. There are two main differences in this system compared to that used in the 2023 g-factor experiment. First, the section below the mixing chamber that is cooled to $\sim$ 10 mK is significantly longer than in the previous apparatus. This enables us to extend the trap into the center of the 6 T superconducting solenoid and mount the SQUID system 50 cm away from the center of the magnet where the fringe field is significantly reduced. This elongated design enables the operation of the SQUID while maintaining dilution refrigerator temperatures both at the trap region and the SQUID region.

In practice, we measure the same temperature at both the mixing chamber and the top of the tripod region to within 1 mK indicating a good thermal connection between these stages. During optimal running, with no heat load, both these regions of the dilution refrigerator achieve temperatures of $<$ 10 mK. The second major difference from the 2023 system is the replacement of 1-K pot or pumped helium-4 stage with a Joule-Thomson (JT) stage. Mixture is pressurized at the input of this stage with a hermetically sealed compressor. Through the expansion of 4 K pre-cooled mixture in the JT chamber, this stage reaches temperature of 2.2 K or less. The advantage of JT stage over a 1-K pot stage is that no helium is consumed from the dewar to pre-cool the mixture, therefore reducing our overall helium consumption.

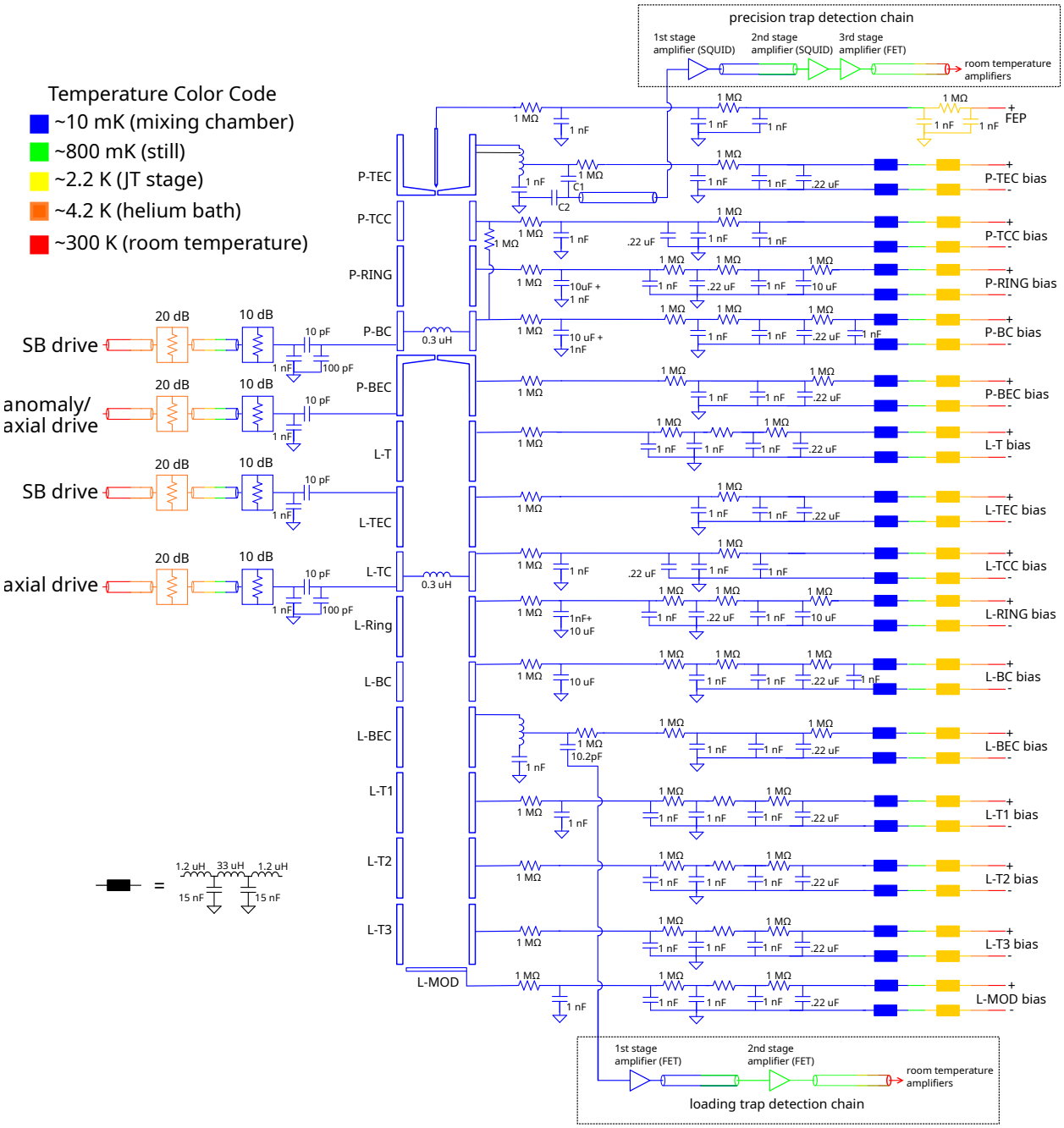

Figure 2.15: Overview of the Penning trap wiring, both traps measurement and positron loading

Below the JT stage are Still, intermediate cold plate, and mixing chamber stages which routinely reach temperatures of 1 K, 300 mK, and 10 mK respectively.

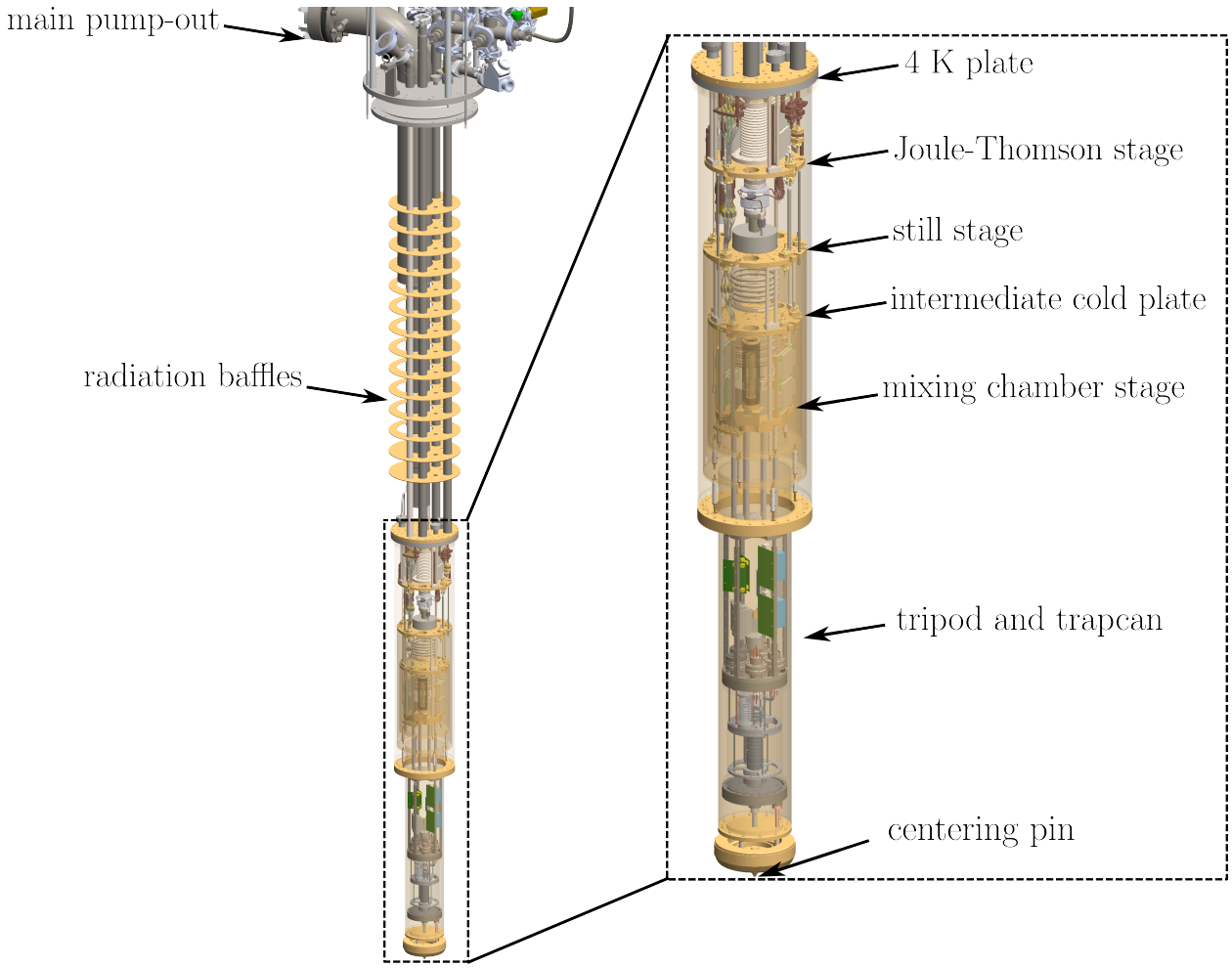

Figure 2.16: Expanded dilution refrigerator section.

The cooling power of the dilution refrigerator is shown in Figure 2.17. The cooling power of the fridge at 25 mK is about 30 μW when run at a high flow rate configuration, that is, when the still stage is heated. The two bias lines of the SQUID amplifier are typically filtered with 25 kΩ cold resistors thermally anchored to the mixing chamber (see Figure 3.15), and carry currents of $\sim$ 10 μA each. This would deliver a heat load of 5 μW in total, therefore, we can reach temperatures bath temperatures of $<$ 25 mK with the SQUID running. Lower temperatures can be reached if the DC bias filter resistors are thermally anchored to the still stage instead. The axial motion of particles in the accumulation trap is

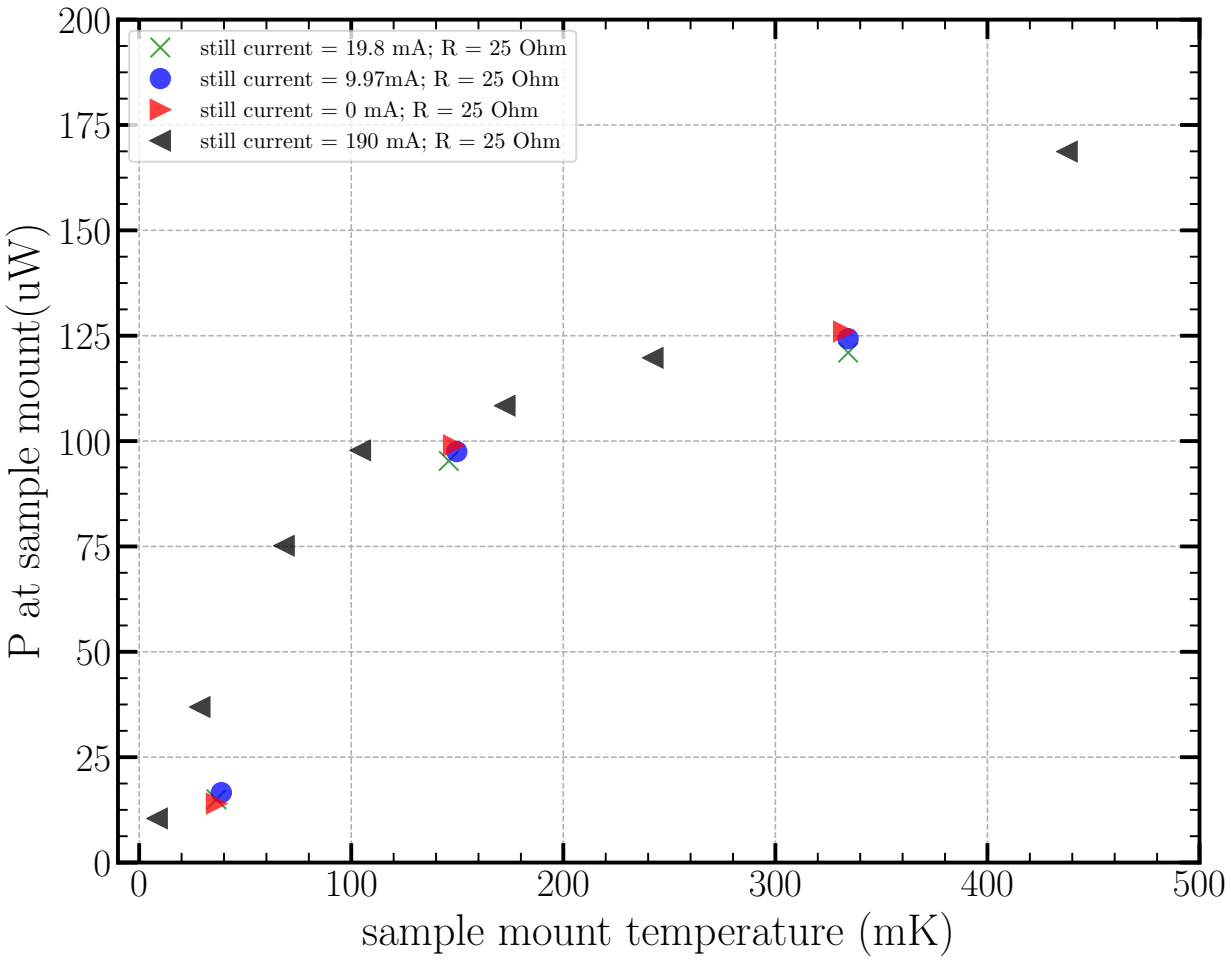

Figure 2.17: Cooling Performance of the dilution refrigerator.

detected using the traditional cryogenic HEMT amplifier starved down to low currents [61]. We typically run these amplifiers with a current $I_{\text{drain}} = 100$ μA dissipating about 100 μW on the mixing chamber. It is important to note that with the HEMT, even in this starved down configuration, where bath temperature can reach below 50 mK, the noise temperature of the amplifier circuit is typically much larger (1-5 K).

2.5.3 Superconducting Magnet and Magnet Dewar

The dilution refrigerator is inserted into a liquid helium dewar with a 6 T cold bore niobium-titanium solenoid magnet. Like with the 2023 system, the cold bore design enables a direct mechanical link between the superconducting solenoid and the dilution refrigerator. The complete system is shown in Figure 2.18. The 2008 g-factor measurement [40, 41] was limited by relative motion between the dilution refrigerator and the magnet resulting in apparent magnetic field noise. This reduced the data collection run time to periods of quiet ambient vibration conditions. Additionally, ambient temperature fluctuations were observed to cause magnetic field fluctuation. This resulted in the entire apparatus having to be temperature regulated [41].

In the 2023 measurement [6, 42], this redesign of the magnet-fridge coupling allowed continuous data acquisition resulting in 20 times more statistics and the measurement of the g-factor at 11 different magnetic fields. However, this cold bore design introduces two major challenges to the operation of the system. First, the dewar helium boil off is now about 18 L per day compared to a few liters per week in the previous system. This boil-off would be prohibitively costly if not for local helium recovery and reliquefication using a commercial helium reliquefier (CRYOMECH PT420RL). This reliquefier has a reliquefication capacity of around 30-40 L per day. The additional capacity of the reliquefier allows us to recover helium boil off from other experiments in the lab and even liquefy helium from compressed helium gas cylinders.

The second challenge introduced by the cold bore design is the added difficulty and complexity when inserting the dilution refrigerator directly into the liquid helium bath during the cool down of the system. This labor intensive process typically leads to the dewar being unavoidably open to atmosphere during the cool down. Despite significant efforts to mitigate this, cool down in the old system led to loss of helium to atmosphere and contamination

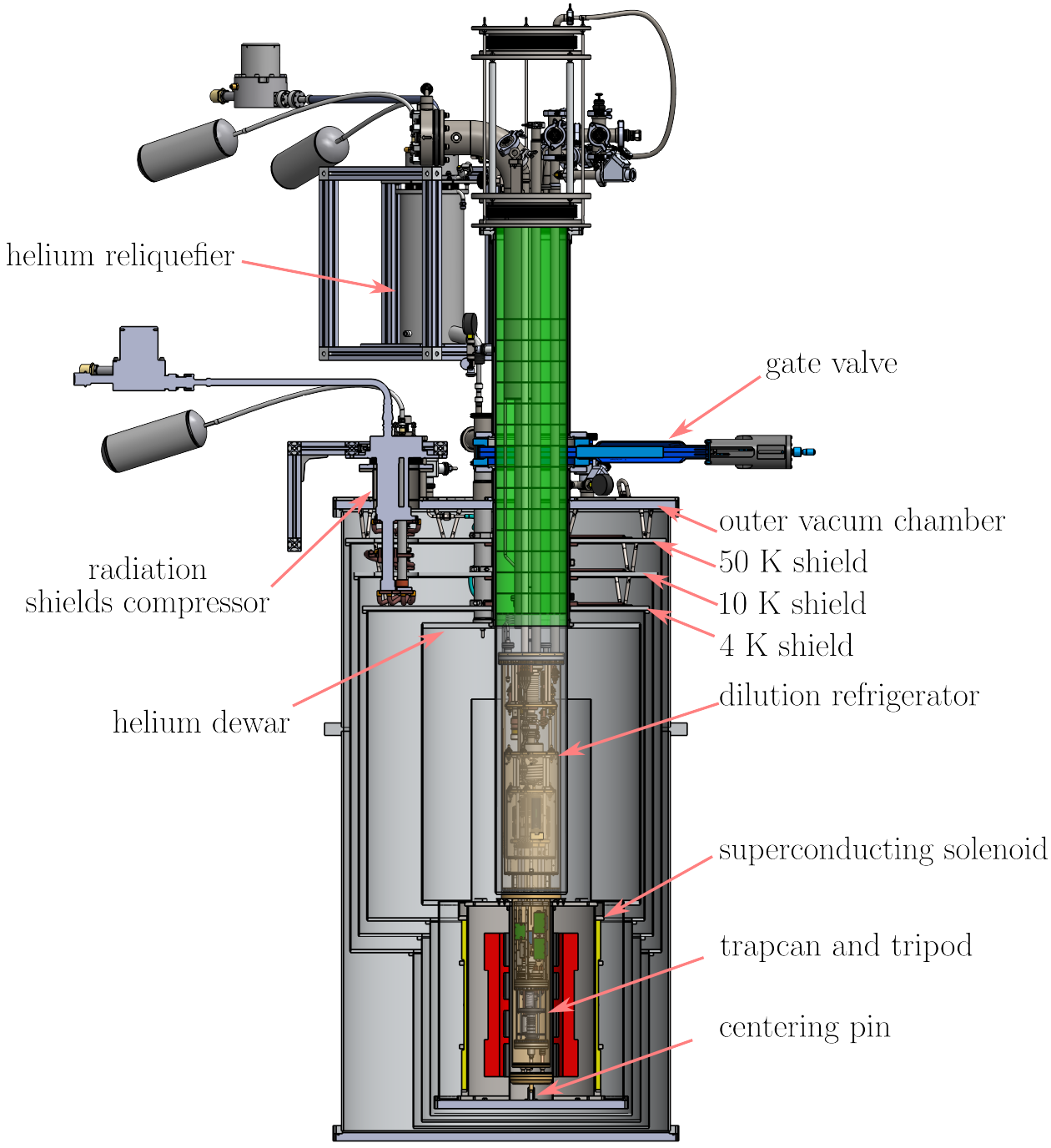

Figure 2.18: New Magnet Dewar

of the liquid helium dewar space with air leading to clogging of the reliquefier. In the new system, we mostly avoid this operational complexity through the introduction of a large gate valve between a long aluminum nipple flange above the gate valve. A seal is made between the top of the long nipple and the dilution refrigerator apparatus using a cryogenic O-ring. This allows us to seal the system from atmosphere before the gate valve is opened and the fridge is inserted into the liquid helium dewar. Through this improved design we are able to recover most of the helium boiled off during the cool down and the cool down process is greatly simplified.

The final major change in the new system is the replacement of the liquid nitrogen dewar shield that encased the liquid helium dewar with a pulse tube refrigerator (CRYOMECH PT415) cooled three-layer radiation shield. During normal operation, the three layers reach temperatures of 80 K, 25 K, and 5 K as measured at the top of the shields. This significantly reduces the radiation heat load on the liquid helium dewar and the conduction heat load along the neck of the dewar. We find that the system is capable of running with the thermal shields pulse tube refrigerator turned off for about 12 hours before the increased heat load begins to increase the boil off of the dewar.

We have found that once this system, with the dilution refrigerator installed, is capable of running indefinitely without the need for refilling liquid helium. The only instances where liquid helium must be added to the system is during periods where the reliquefier is turned off for an extended period of time, or when there is an additional heat load on the system either during the dilution refrigerator cool down or during the ramping of the superconducting magnet.

Thermoacoustic (Taconis) Oscillations in the Dewar

Although the system runs without issue today, we encountered significant challenges in the commissioning of the magnet dewar system that were not observed by the manufacturers

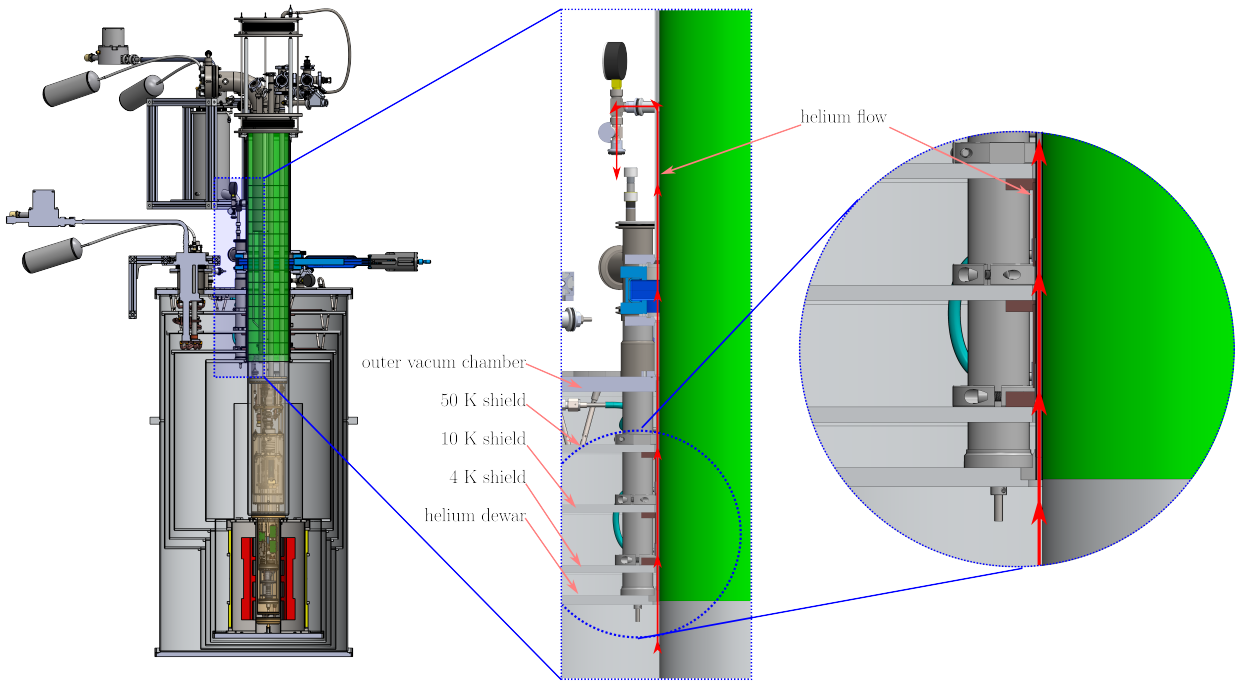

Figure 2.19: Source of major thermoacoustic oscillation in the dewar

in their abridged factory validation tests. During the first cool down of the dewar, the system ran without helium loss for about 20 hours before spontaneously transitioning to a mode where the boil off more than doubled to about 40 L per day, far above the reliquefication capacity of the local helium reliquefier.

This test was repeated several times and the clear trend emerged that as the system got colder, it would cross a threshold condition where the boil off would suddenly become unmanageable. After many studies, we discovered that the cause for the sudden increase in boil off was several sources of thermoacoustic oscillations in ports of the dewar between room temperature and the 4 K space. A narrow tube with one end closed at room temperature and the other open at 4 K, will create a self-excited flow oscillation pulling significant warm helium gas into the dewar and creating a massive heat load. A source of one such thermoacoustic oscillation along the neck of the dewar is show in Figure 2.19 and its vibration spectrum

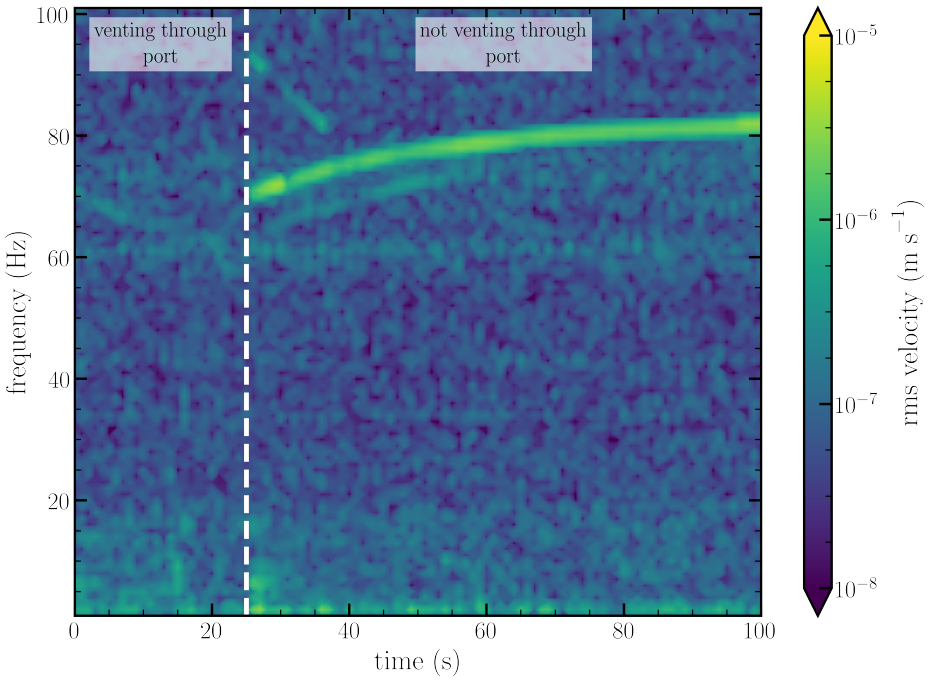

Figure 2.20: Fill port thermoacoustic oscillation

when self-excited is shown in Figure 2.20

We hypothesize that the reason why these oscillations are more severe in this system is because the top of the liquid helium dewar is held at a very low temperature aided by the cooling of the radiation shields. The reason this was not observed in the factory tests is because the tests were not run long enough for the upper part of the liquid helium dewar to reach its base temperature.

Once identified, the solution to the thermoacoustic oscillations is straightforward:

- In ports that with vent paths, we ensure the correct flow path to avoid stationary columns of helium gas. An example of this is in Figure 2.19

- In ports without vent paths, we introduced small holes along the length of the vent port (inside the liquid helium dewar) to damp out the thermoacoustic oscillation preventing its resonant behavior.

2.5.4 Vibration Isolation in the New System

Both the 2023 and 2008 g-factor measurements suffered from a broadening of the measured cyclotron lineshape from an undetermined source. A possible source of this broadening is magnetic field noise. Since the cyclotron line (linewidth $\sim$ 100's of Hz) is affected by the broadening effect but not the anomaly line (linewidth $\sim$ 0.1 Hz), then it suggest the timescale of magnetic field noise that could result in the broadening to be sub-hertz to a few hundred Hz. A vibration induced magnetic field noise in superconducting solenoids has been observed around this frequency range [91].

We have designed and installed an active vibration isolation platform to reduce the coupling of ambient terrestrial vibrations in the lab to our dewar. The platform relies on TMC Vibration Control's STACIS III vibration isolation system. The STACIS III system integrates inertial vibration sensors with a feedback loop to control piezoelectric actuators to cancel vibrations on the platform in real time. The isolation bandwidth is from 0.6 to 150 Hz with 40-70% isolation at 1 Hz and more than 90% isolation above 2 Hz. The performance of the vibration isolation floor on installation is shown in Figure 2.21

In the optimal case, that is, with most pump lines decoupled, we achieve vibration criterion VC-H or better ($< 3 \times 10^{-7}$ ms^{-1}) across the performance band of the STACIS platform. This is already a challenging vibration criterion to achieve and is at the limit of the performance of the isolation platform. For reference Figure 2.21 includes some other vibration criterion levels:

- VC-C or better - adequate for optical microscopes up to 1000×, lithogragraphy and moderately sensitive electron microscopes that resolve up to 1 μm detail size
- VC-E or better - challenging criterion suitable for the most demanding sensitive equipment including laser based systems, e-beam lithography working at nanometer scales

It is important to note here that the vibration isolation system only isolates from vibration

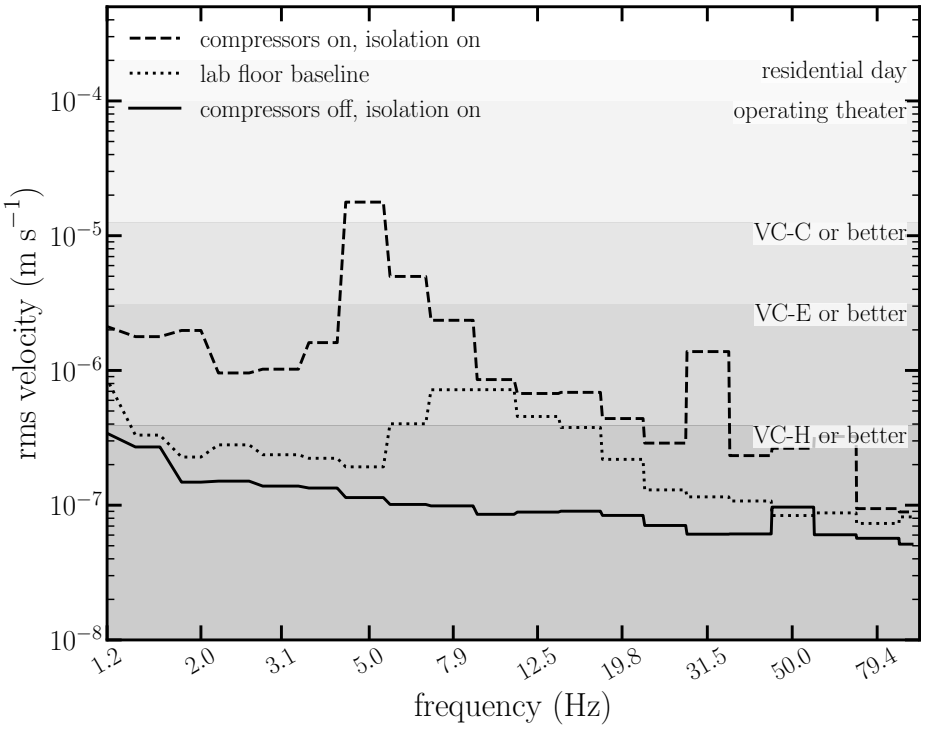

Figure 2.21: Isolation of Dewar top from ambient vibrations

it senses from its own inertial sensors coming from the floor below. It is unable to isolate or cancel from vibration noise coming from within, e.g. thermoacoustic oscillations, or from vibrations coupled in above the floor platform, e.g. PTR compressor or pump noise coupled in through pumping lines. In fact, the STACIS isolation platform will incorrectly respond to vibration noise coupled in from above resulting in an amplification of this noise and even the generation more vibration noise frequencies as seen in Figure 2.22. Here a large thermoacoustic oscillation is introduced through stopping the flow of helium through a vent port introducing vibrations at 35 Hz and 75 Hz. The response of the STACIS floor to these internal oscillations produces more noise at frequencies that depend on the internal oscillation frequency.

Extensive work must now follow the installation of the floor to optimally decouple the top of the dewar from its surrounding environment.

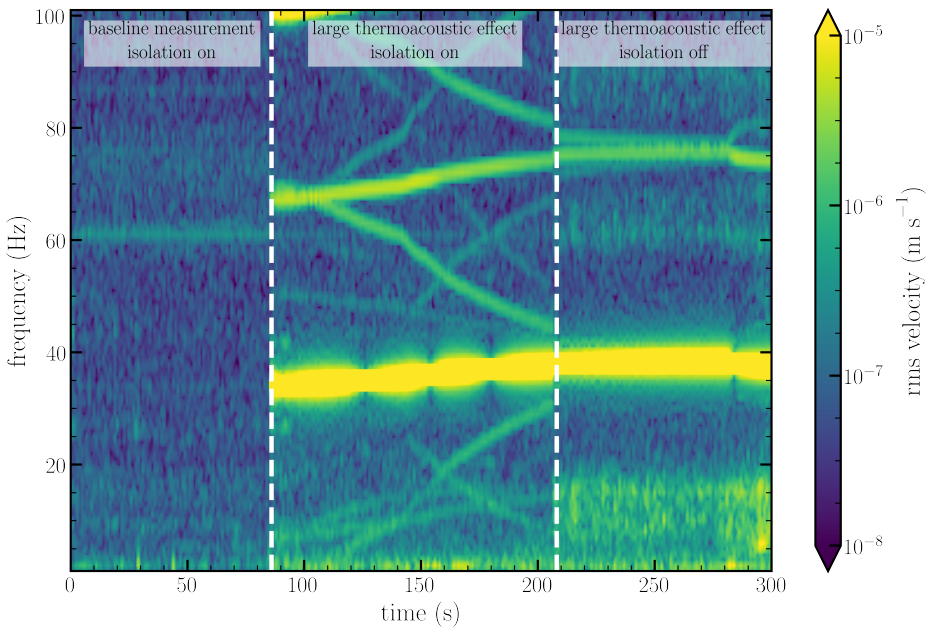

Figure 2.22: Isolation Performance when a violent thermoacoustic oscillation emerges. The left most panel shows the vibration spectrogram in the optimal case with the STACIS platform, the middle panel we enable an internal thermoacoustic oscillation in the dewar with the isolation platform on, and the left panel shows the vibration spectrum with the thermoacoustic oscillation but with the isolation platform off. In the middle panel it is clear that the isolation platform is unable to damp the internal oscillation of the dewar and in fact makes it worse creating vibrations in response to the thermoacoustic noise.

2.6 Summary

An entirely new apparatus has been designed, installed, and commissioned for future electron and positron magnetic moment measurements. New more harmonic harmonic Penning traps are implemented with improved axial frequency sensitivity. The new traps are installed in an entirely new dilution refrigerator capable of achieving temperatures of less than 10 mK. The superconducting solenoid has been redesigned to have a smaller fringe field for the implementation of the SQUID amplifier and is housed in a new magnet dewar that can run indefinitely without helium loss. Finally, we have implemented vibration isolation solutions to address the unknown broadening in the measured cyclotron line observed in previous g-factor measurements.

Chapter 3

Implementation of a Quantum Limited Detector

The induced image current from the trapped electron's axial oscillation is our only probe of its motion. This small current oscillating at the trapped particle's axial frequency is passed through a LCR resonant tuned circuit. When the axial frequency of the particle is on resonance with the tuned circuit, the image charge current induced sees a purely resistive load $R = Q\omega_z L$. This small signal is amplified by a chain of low noise cryogenic amplifiers such that it becomes measurable using room temperature electronics. The signal-to-noise ratio of the signal is the ratio of the electron signal to the Johnson noise of the high impedance LCR circuit.

Past measurements have used a low noise High Electron Mobility Transistor or HEMT amplifiers (Fujitsu FHX13LG) starved down to dissipate only 50-100 μW of power, three orders of magnitude below its designed 10 mW power output. Even with heroic heat sinking of the transistor to the dilution refrigerator, the HEMT heats the dilution refrigerator to around 100 mK and, even at these temperatures, the electron's axial motion is heated to a temperature of several kelvin by the amplifier's temperature [61]. This elevated noise

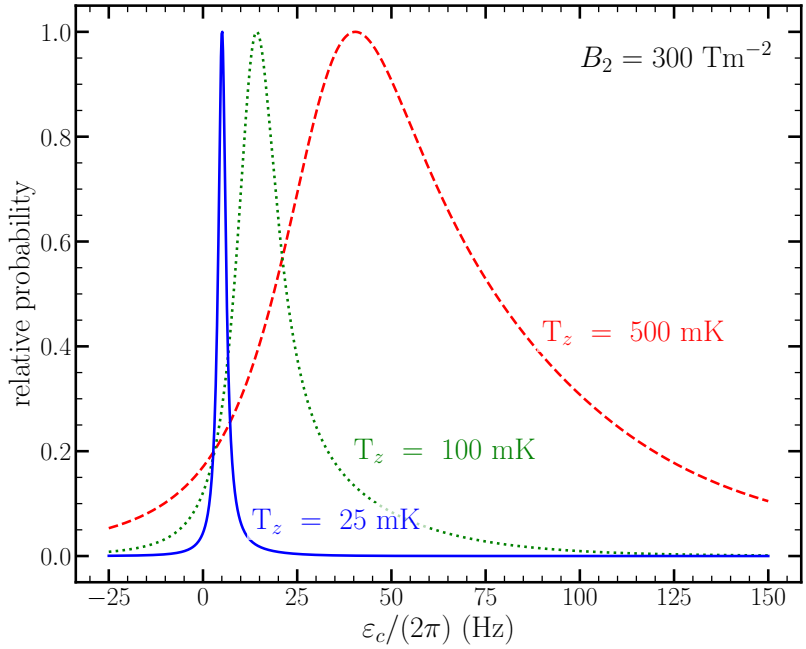

Figure 3.1: Cyclotron lineshape temperature dependence plotted against detuning $\varepsilon_c/2\pi$ for magnetic bottle size $B_2 = 300$ Tm^{-2}, the bottle size used in the most recent measurement. The axial damping rate is $\gamma_z/2\pi = 20$ Hz, cyclotron damping rate is $\gamma_c/2\pi = 0.05$ Hz, axial frequency is $\nu_z = 120$ MHz, and the drive strength is $\Omega_c = 0.1 \times \gamma_c$.

temperature heats the particle's motion in the inhomogeneous field of the magnetic bottle used for state readout. This broadens the measured cyclotron lineshape and this axial temperature broadening effect was one of the leading systematics in the 2023 measurement.

The cyclotron linewidth is is given by [68, 92–94],

$$\Delta\omega_c = \frac{eB_2}{m_e}\frac{k_B T_z}{m_e \omega_z^2}, \tag{3.1}$$

where B_2 is the size of the magnetic bottle, T_z is the temperature of the electron's axial motion. The calculated cyclotron lineshape [93, 94] for $B_2 = 300$ Tm^{-2} at three axial temperatures $T_z = 500$ mK, 100 mK, and 25 mK are shown in Figure 3.1. The lineshape is a Lorentzian at the cyclotron frequency convolved with an exponential tail that arises from the thermal distribution of axial states in the inhomogeneous magnetic field of the magnetic

bottle. The goal of this work is to reduce the axial temperature by a factor of 20 from the 500 mK limit in the 2023 measurement will narrow the measured lineshape by a factor of 20. The cyclotron frequency can then be determined far more precisely from a narrower resonance line.

This work implements a *near*-quantum limited Superconducting QUantum Interference Device (SQUID) amplifier to achieve the lowest possible axial temperature of the particle. The SQUID amplifier has been shown to reach noise temperatures T_n of 2–5 times the quantum limited temperature T_{SQL} at that frequency [73]. At 120 MHz, $T_{\mathrm{SQL}} = 2.9$ mK, and therefore we can expect in the ideal implementation to achieve noise temperatures $T_n \approx 6 - 15$ mK.

The figure of merit in out experiment for the electron magnetic moment experiment is the axial temperature of the particle. As we will discuss in this chapter, we expect that the axial temperature of the particle will be limited by the bath temperature of the dilution refrigerator T_0. This presents a clear path to achieving a factor of 20 reduction in the axial temperature and cyclotron linewidth. This chapter discusses the axial temperature of the particle, operation of the SQUID amplifier, its implementation in the electron Penning trap, and demonstrations of single electron detection with the new amplifier.

3.1 Axial Temperature of the Particle

The axial temperature of the particle is determined by the bath temperature T_{bath} and the additional temperature added by the amplifier's elevated internal temperature at its input T_{in}. We can estimate the axial temperature of the particle by first determining the temperature at the input to the first stage SQUID amplifier then considering how much of that amplifier input temperature couples to the electron through our matching circuit.

Temperature at the input to the first stage. Figure 3.2 shows our amplifier noise

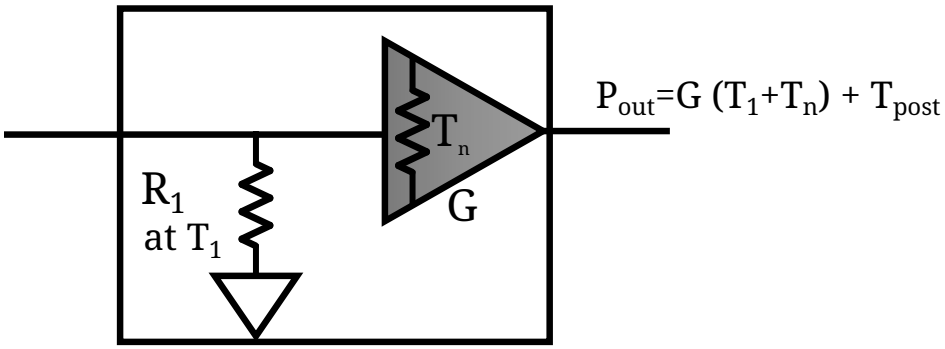

Figure 3.2: Amplifier Noise Model

model. Referenced to the power at the output of the amplifier, the temperature seen at the input of the amplifier, in the worst case scenario, is,

$$T_{\text{in}} = T_1 + T_n + T_{\text{post}}/G, \tag{3.2}$$

where T_1 is the physical temperature of the amplifier's input resistor, T_n is the noise temperature of the amplifier, T_{post} is the noise added at the output of the amplifier from subsequent stages of amplification, and G is the linear power gain of the amplifier. This model assumes the worst case that the internal noise added by the amplifier, as seen at the output, maximally adds to the temperature seen at the input to the amplifier.

For a SQUID, we assume that $T_1 = T_{\text{bath}} = 10$ mK and the noise temperature is 5 times the standard quantum limit [73]. Thus $T_n = 5 \times T_{\text{SQL}} = 15$ mK. The temperature added by post amplifiers must be suppressed such that it does not significantly contribute to T_{in}. Assuming that subsequent amplification stages add no noise (i.e. T_{post}/G is negligible), then we achieve $T_{\text{in}} = 25$ mK. Therefore, the number of subsequent amplification stages must be designed to ensure this criteria.

The first stage room temperature amplifier (FZX60-P103LN+) adds at most 350 K of noise at its input. Suppressing this noise contribution at the input to the first stage SQUID requires linear gain $G = 35000$ (45dB) across the amplifier detection chain. We accomplish

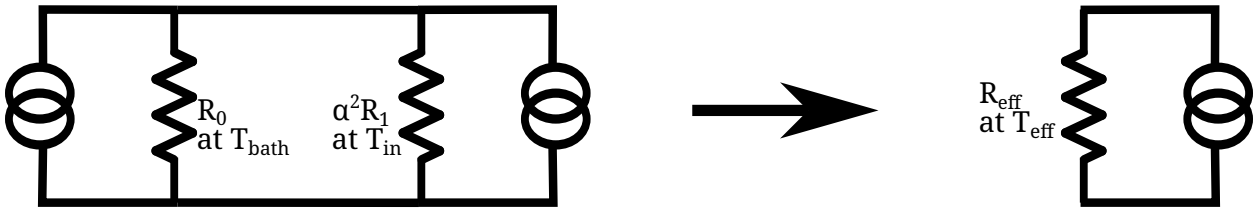

Figure 3.3: Model for noise coupled to electron through our impedance matching circuit. α is the impedance transformation ratio.

this through our cascaded cryogenic detection chain consisting of two SQUIDs each having 20 dB gain and a cryogenic FET with 15 dB gain. This chain adds 55 dB of gain cryogenically when optimally tuned. In this case the the room temperature amplifier's contribution at the input to the first stage SQUID is ~ 1 mK. Therefore, the total temperature at the input of the first stage SQUID amplifier is $T_{\text{in}} = 26$ mK or lower.

Amplifier noise driving the electron's axial motion. We perform a huge impedance transformation between the high-Q LCR circuit at temperature T_{bath} used to damp the electron's motion, $R_0 \approx 250\ k\Omega$, to the input of the first stage SQUID, $R_1 \approx 100\ \Omega$ at temperature T_{in}. The RF transformer has an effective *turns ratio* of α. We use the model shown in Figure 3.3 to estimate the effective resistance R_{eff} and its temperature T_{eff} as seen by the electron. Thus, $R_{\text{eff}} = R_0\alpha^2 R_1/(R_0 + \alpha^2 R_1)$ and T_{eff} is given by,

$$\frac{T_{\text{eff}}}{R_{\text{eff}}} = \frac{T_{\text{bath}}}{R_0} + \frac{1}{\alpha^2}\frac{T_{\text{in}}}{R_1}. \tag{3.3}$$

If the LCR-circuit is perfectly matched to the input to the amplifier, $R_0 = \alpha^2 R_{\text{in}}$. In this configuration, the effective temperature as seen by the electron $T_{\text{eff}} = \frac{1}{2}(T_{\text{bath}} + T_{\text{in}}) \approx 22.5$ mK. This 20 times lower than the axial temperatures observed in the 2023 g-factor experiment. In instead, to maintain a high R_{eff} as seen by the electron, we under-couple the

LCR-circuit to the input of the amplifier, so $R_0 \ll \alpha R_{\rm in}$,

$$T_{\rm eff} \simeq T_{\rm bath} + (T_{\rm in} - T_{\rm bath})\frac{R_0}{\alpha^2 R_2} + \ldots \tag{3.4}$$

If $\alpha^2 R_1 \gg R_0$ the axial temperature of the electron will approach the bath temperature provided by the dilution refrigerator.

3.2 Principle of the SQUID

A DC SQUID consists of a single superconducting loop containing two Josephson Junctions (Figure 3.4). It combines two physical principles: (i) flux quantization in a closed superconducting loop [95, 96], and (ii) Josephson tunneling through a JJ [97, 98], a device consisting of a thin layer of insulator sandwiched between two superconductors.

The flux through a superconducting loop is quantized in integer multiples of the flux quantum $\Phi_0 \approx h/2e = 2.07 \times 10^{-15}$ Wb. The addition of the Josephson junctions probe the phase of the Cooper pair wavefunction whose wavelength depends on the flux penetrating the SQUID loop. The two junctions interfere, thus the SQUID's critical current (and therefore its voltage response under bias) oscillates periodically with the flux threading the SQUID loop in units of the flux quantum Φ_0. This makes the SQUID extremely sensitive to magnetic field, changes with typical sensitivities of 1 fT/$\sqrt{\rm Hz}$.

There is no voltage drop across the Josephson junction as the current flowing through it, $I_{\rm bias}$, is increased from zero until the critical current I_c is surpassed ($I_{\rm bias} > I_c$). Above this current, the behavior of the junction approaches Ohm's law. As the current is reduced back to zero, the voltage drop across the Josephson junction remains non-zero until $I_{\rm bias} < I_c$, after which it suddenly drops to zero. This hysteretic behavior is undesirable in most applications and is eliminated by adding a shunt resistor $R_{\rm sh}$ in parallel with the Josephson junction to

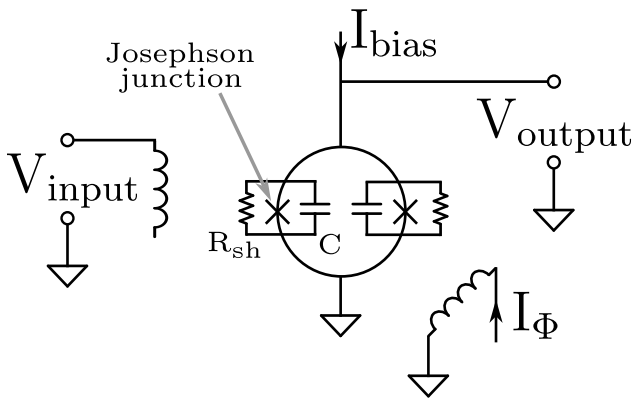

Figure 3.4: SQUID amplifier circuit schematic. The SQUID consists of a superconducting loop with two Josephson junctions. Each junction has a parasitic capacitance C and shunt resistor $R_{\rm sh}$. The SQUID is tuned to its optimal gain bias configuration with a coil carrying current I_Φ called the flux bias current and signal is coupled into the SQUID loop with the main coil on the left.

add damping. The shunt resistor dissipates the excess energy of the junction, preventing the superconducting phase difference from continuing to change with time, producing a voltage, once the current drops below I_c, thereby eliminating hysteresis. Additionally, real Josephson junctions have some parasitic shunt capacitance C. The schematic of a typical SQUID loop is shown in Figure 3.4.

The measured DC characteristics of the DC SQUID used in this experiment are shown in Figure 3.5. As seen in Figure 3.5 (a), the voltage drop across the loop remains zero until the critical current is surpassed. At currents above the critical current, the junctions are in the finite-voltage resistive state where the voltage drop is described by the Resistively and Capacitively Shunted Josephson (RCSJ) model [99]. The critical current through the whole SQUID I_c is a function of the applied flux,

$$I_c(\Phi) = 2I_{c,0}\left|\cos\left(\pi\frac{\Phi}{\Phi_0}\right)\right|, \tag{3.5}$$

where Φ is the flux through the SQUID loop. This describes the position of the two knees of the IV-curves shown for different flux bias settings.

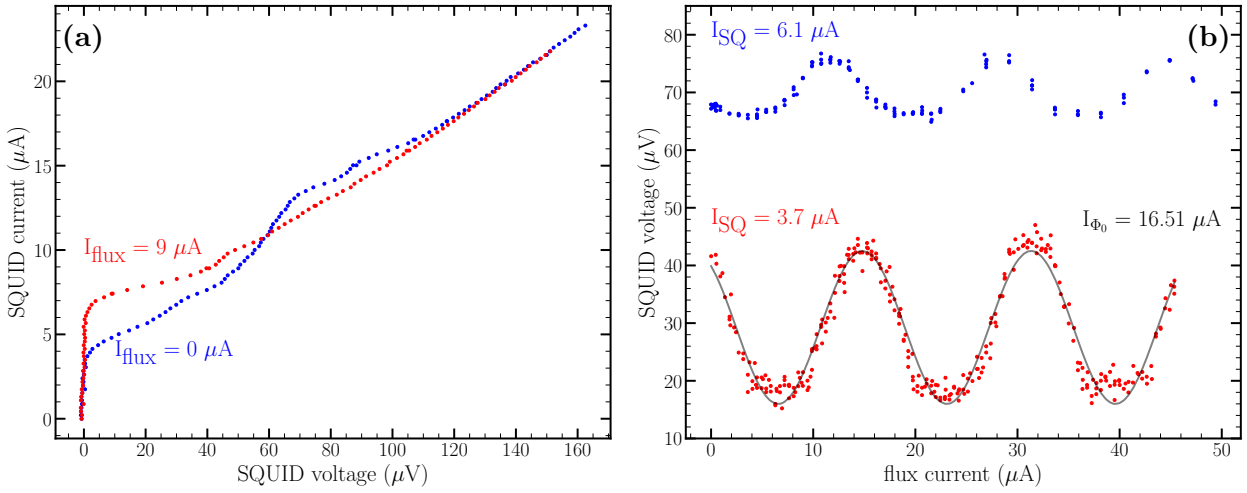

Figure 3.5: Measured DC characteristics of the SQUID at 4 K. (a) Typical IV-curve at two different flux bias conditions. (b) Flux current scan at two different SQUID biases. Fitting these curves this we determine the current for one flux quantum 16.5 μA.

Figure 3.5 (b) shows the voltage drop across the SQUID loop at a fixed bias current I_{bias} as a function of the flux through the loop which is controlled by the flux current I_{flux}. This oscillatory behavior is described by,

$$V_{\text{SQ}} = R_{\text{sh}} \left(I_{\text{bias}}^2 - 4I_c^2 \cos^2 \left(\pi \frac{\Phi}{\Phi_0} \right) \right)^{1/2} \tag{3.6}$$

The flux threading the SQUID can be adjusted, through changing I_{flux}, to the steepest point of the response curve making the device extremely sensitive to fluctuations of the flux around this region. This response has often been exploited to build magnetometers, voltage standards, microscopes, and ultra-sensitive low-noise amplifiers. The first use of a DC SQUID as an RF amplifier for a single electron in a Penning trap is explored in the rest of this chapter.

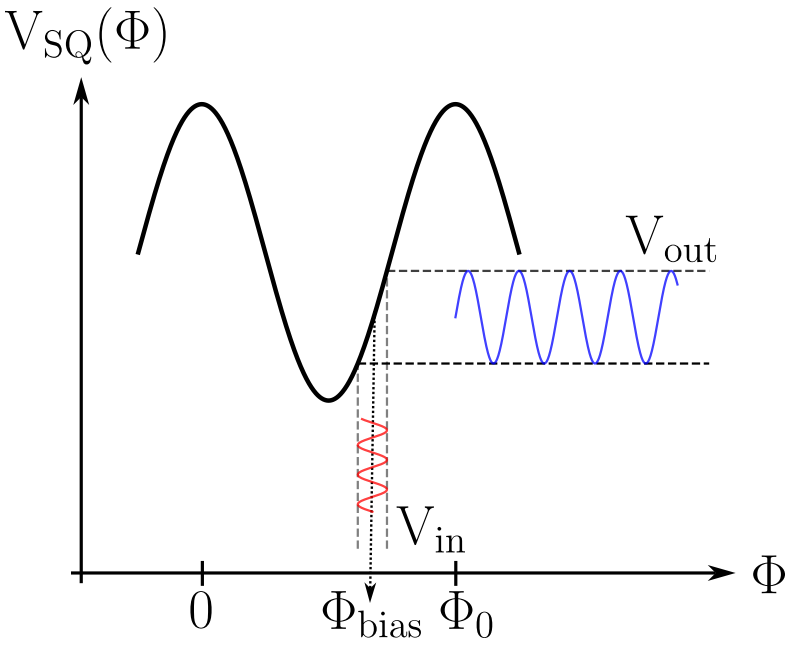

Figure 3.6: SQUID Transfer Function

3.2.1 The DC SQUID as an RF Amplifier

The standard DC SQUID can be configured as an RF amplifier by coupling the input RF signal to the SQUID loop through windings placed on top of the loop [100]. The oscillating current through input coil I_{signal} creates a tiny oscillating magnetic field that is coupled into the SQUID on top of the flux bias, that is $I_{\text{flux bias, total}} = I_{\text{flux}} + I_{\text{signal}}$. As schematically illustrated in Figure 3.6, by tuning the flux bias of the SQUID to the steepest part of the transfer function, a small oscillating voltage at the input of the SQUID produces a large voltage at its output.

While the described coupling scheme works well at relatively low frequencies, with standard commercial devices readily available up to 20 MHz, the parasitic capacitance between the RF input coil and the SQUID loop severely reduces the gain at higher frequencies. The Microstrip SQUID Amplifier or MSA was invented to circumvent this challenge by coupling signal into the SQUID through a resonant circuit formed by a superconducting microstrip

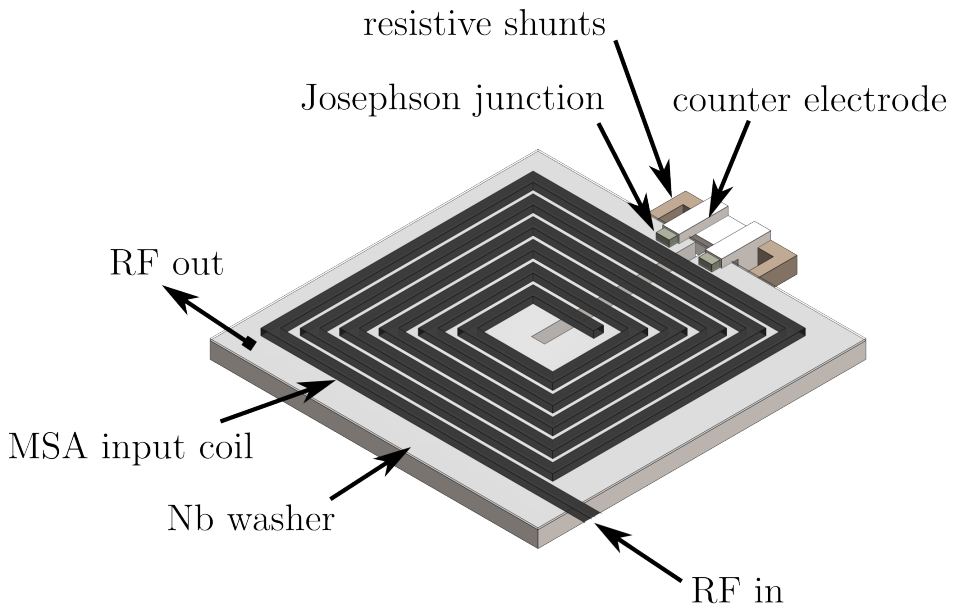

Figure 3.7: Schematic of the Microstrip SQUID Amplifier

resonator patterned on an thin insulating layer directly on top of the SQUID [101]. A schematic of an MSA is shown in Figure 3.7.

The microstrip inductance and parasitic capacitance to the SQUID plane form a resonant circuit. One end of the microstrip is connected to the input signal and the other is left open forming a half wave resonator. In this configuration the MSA has maximum gain when the input signal's wavelength is roughly half the effective length of the microstrip input coil.

MSAs with frequencies from 100 MHz to a few GHz and gains higher than 20 dB have been fabricated. Noise temperatures less than 1 K are typically reported, often below the ambient physical temperature [73, 102, 103] at temperatures ranging from 50 mK to 4 K.

For the work described in this thesis, we use a SQUID with gain centered at 120 MHz where $T_{\mathrm{SQL}} = 2.9$ mK. In the best implementations, the noise temperature achieved is typically 2–5 times the quantum-limited temperature [102]. We therefore expect that in this regime, the axial temperature of the particle will be limited by the ambient physical

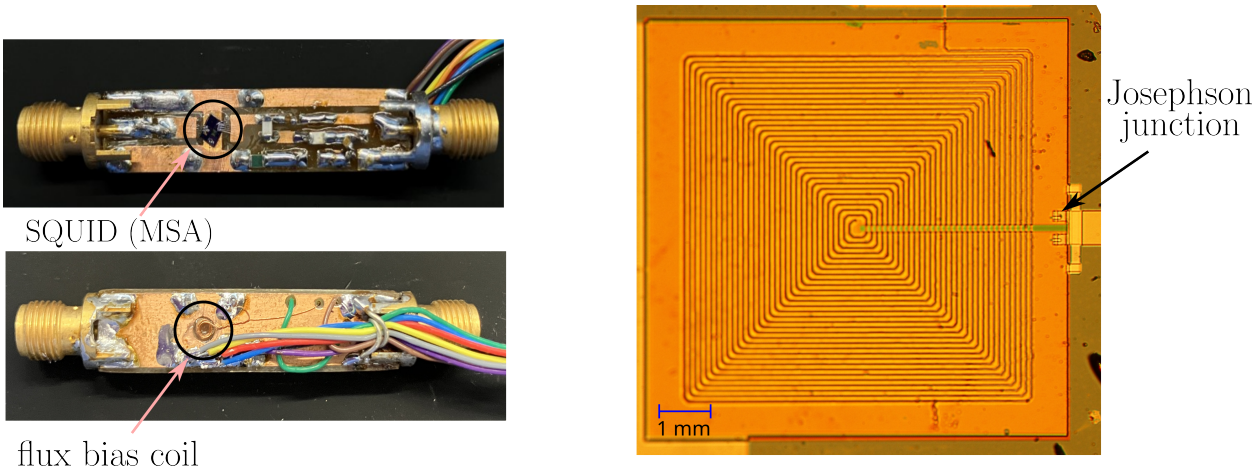

Figure 3.8: 120 MHz Microstrip Amplifier. (a) MSA SQUID PCB board. RF is capacitively coupled into and out of the SQUID chip via 1 nF capacitors. The DC SQUID biases are fed onto the board via the attached wires. (b) Magnified image of the MSA SQUID amplifier chip.

temperature of the dilution refrigerator, about 10–25 mK, and not the noise temperature of the amplifier like in all previous g-factor experiments.

3.2.2 The Microstrip SQUID Amplifier and its Performance

Figure 3.7 shows a schematic of the MSA consisting of a microstrip resonant input coupling coil and a niobium washer with Josephson junctions, and resistive shunts comprising the SQUID loop. The MSA used in our experiments is a custom device fabricated by ez-SQUID that is resonant at 120 MHz. This device is shown in Figure 3.8.

It consists of a 600 μm $\times$ 600 μm niobium washer on a silicon oxide substrate with a slit of width 10 μm and length 300 μm cut out to form the SQUID loop. The Josephson junctions are located at the base of the of the loop and are made from about 3 μm^2 of Nb-Al-Al_2O_x-Nb with a critical current of about $I_c = 10$ μA at 4 K across both junctions forming the SQUID. The Josephson junctions are shunted with a palladium shunt resistor of resistance $R_{\mathrm{sh}} \sim 10\ \Omega$ at 4 K. The ground side of the Josephson junctions and shunt resistor

is a niobium counter electrode. The MSA design and fabrication process is described in more detail in [104, 105].

On resonance, the MSA behaves as a parallel LCR resonator. As detailed in [104], the measured resonance frequency of fabricated MSAs are far below what would be expected if the device was just the expected parasitic capacitance and inductance of the microstrip loop L. The input inductance of the MSA is instead modeled as $L_i \approx n^2 L + l \times L_0$, were L_0 is the inductance of the SQUID washer ($L_0 \approx 100$ nH). The input impedance Z_0 of the MSA is dominated by the dynamic resistance of the SQUID shunts and Josephson junction. On resonance is $Z_0 \approx 100\ \Omega$. Similarly the output impedance of the SQUID is dominated by the dynamic resistance of the shunted Josephson junction. This makes impedance matching in the cascaded amplifier chain fairly challenging as discussed in 3.3.3.

The MSA is mounted onto a PCB as shown in 3.8. The RF input, output, and DC biases to the MSA chip are made by wire bonding to the PCB. The RF signals are coupled in and out to SMA connectors through 1 nF capacitors. The SQUID is biased through a low pass filter on the PCB board. The flux bias coil is a simple copper wire-wound coil placed behind the SQUID chip on the reverse side of the board.

Gain, Noise Temperature, and Power Dissipation

The three figures of merit that define the effectiveness of the SQUID amplifier are the gain, noise temperature, and power dissipation. As discussed previously, while the physical temperature the particle sees is the bath temperature T_0 plus some contribution from the noise temperature of the amplifier T_n, with sufficiently low T_n, we approach a regime where the temperature of the particle is limited by the bath temperature T_0.

The SQUID must amplify the noise resonance from an LCR circuit at 10–25 mK to well above the noise temperature of the following stages. We cascade amplifiers together, each with gains of 15 dB or more, to reach the goal of 45 dB power gain. The cascaded amplifier

chain is discussed in detail in Section 3.3.3.

The gain performance of the SQUID was measured at 4 K, Figure3.9. The gain peaks at 18 dB around $\sim$ 125 MHz and the Q of the amplifier with a 50 Ω source impedance is about 5. The SQUID saturates at very small input powers (> -100 dBm) and drives above this strength will result in effectively zero power transmission or even attenuation. Very strong RF drives may even quench the SQUID turning it off. For this test, the drive strength of the Network Analyzer is set to -20 dBm and is further attenuated with 60 dB of warm attenuation followed by 25 dB of cryogenic attenuation. The output of the SQUID is attenuated by 5 dB followed by two room temperature amplifiers each with gain $\sim$ 30 dB (MITEQ AU-1442-400).

The SQUID bias lines are heavily filtered with low pass RC circuits at room temperature and cryogenically. We find that heat-sunk cryogenic filters and attenuators are critical for stable operation. The gain measurement is made with SQUID in line then calibrated with the SQUID removed but the rest of the drive line remaining the same.

At the time of writing, the noise temperature of the SQUID used in this experiment has not been measured at dilution refrigerator temperatures, although efforts are being made to accomplish this. For this discussion, we reproduce the results presented in [42] for the noise temperature of a similar SQUID measured at 3.6 K.

The noise temperature of the amplifier T_n is inferred from the noise spectral power as measured on the the spectrum analyzer. The gain of the amplifier must be carefully calibrated out for an accurate measurement. Under the assumption that the noise temperature contribution of subsequent amplifier stages ($T_{\rm post}$) is negligible, i.e. $T_{\rm post}/G_{\rm SQUID} << T_n$, then the noise temperature of the MSA is simply,

$$T_n = \frac{P_0^{\rm on} - P_0^{\rm off}}{G_{\rm total}} - T_{\rm bath}, \tag{3.7}$$

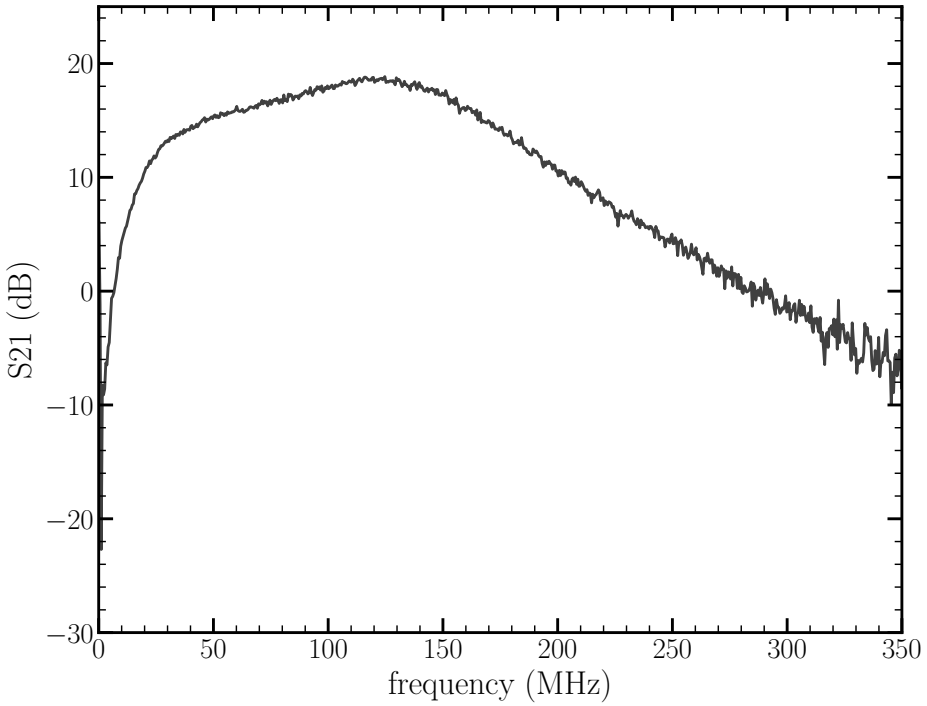

Figure 3.9: Gain of the implemented SQUID amplifier at 4 K. The SQUID bias is set $I_{\text{bias}} = 8$ μA and the flux bias is adjusted to produce the maximum gain. The drive is attenuated to ~ -120 dBm

where P_0^{on} and P_0^{off} are the measured noise spectral powers on the spectrum analyzer, G_{total} is the total gain of the system, and T_{bath} is the temperature of the bath (3.6 K).

Even at 3.6 K, we see a significant reduction of about a factor of 10 in the noise temperature of the MSA compared to our traditional HEMT amplifier across the amplification bandwidth. In the dilution refrigerator implementation this noise temperature should reduce even more to the extent that the back-action noise that the trapped particle sees will be limited by the ambient physical temperature of the dilution refrigerator and not the temperature at the input of the SQUID. The final figure of performance metric we will consider in the implementation of the SQUID is its power dissipation. In previous experiments where a HEMT is employed for axial detection, the power dissipation of the amplifier would approach 10 μW. This would raise the temperature of the dilution refrigerator to more than

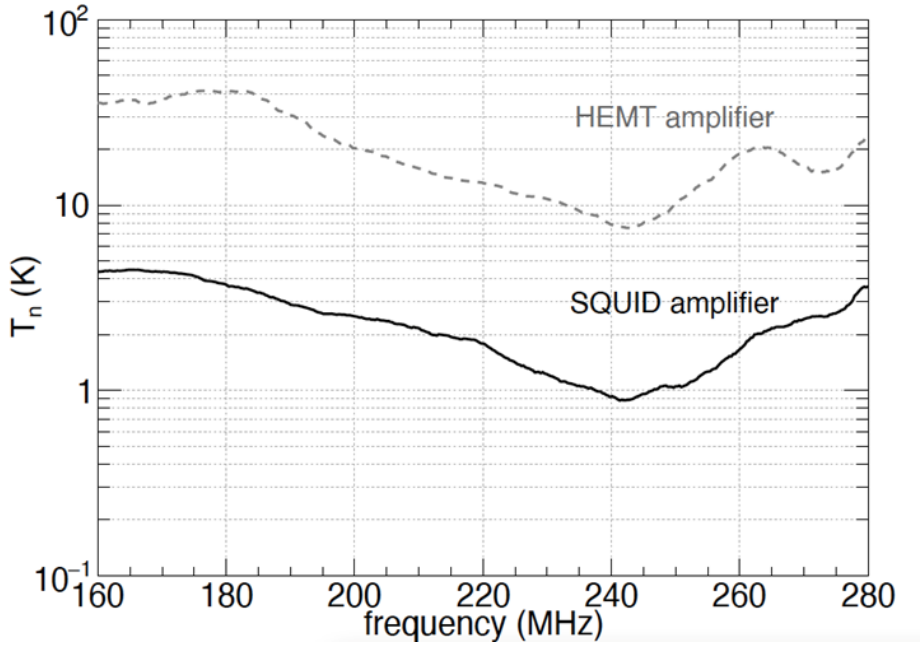

Figure 3.10: SQUID noise temperature measurement at 3.6 K. The noise temperature performance of the traditional HEMT amplifier used in previous measurements is also shown.

80 mK.

The SQUID is operated with a SQUID bias $I_{\text{bias}} \approx 10$ μA and flux bias $I_{\text{flux}} \approx 5$ μA. While in principle, this would result in < 1 nW power dissipation over the shunt resistors of the SQUID, in practice we operate the SQUID with cryogenic RC-filters ($R \approx 25$ kΩ) heat sunk to the mixing chamber. The power dissipated in these filters are the main sources of heat in this implementation of the SQUID. Even in this configuration, the heat load is < 5 μW and the fridge can reach temperatures of < 25 mK. In future implementations of the SQUID, we plan to move these low pass filters to higher stages of the fridge (e.g. still) to achieve even lower temperatures.

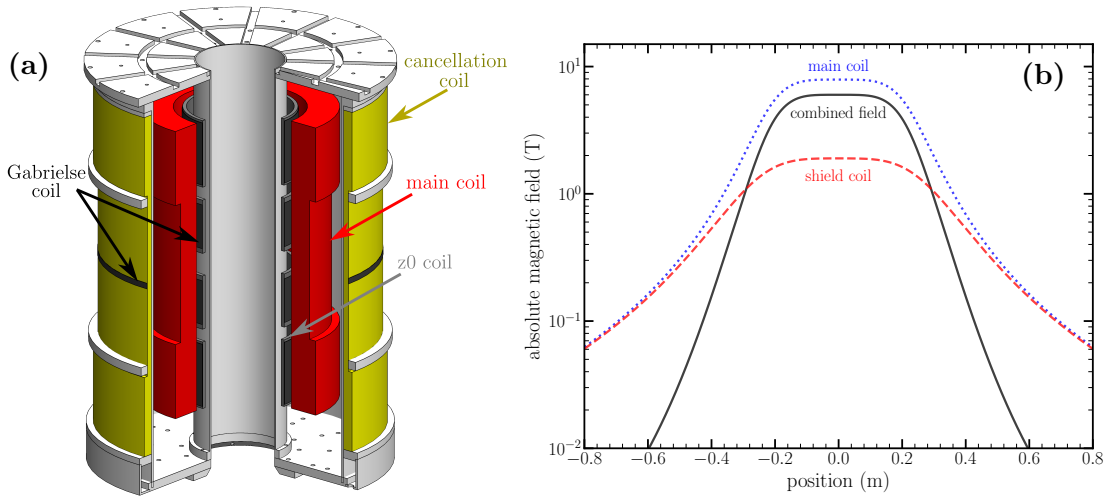

Figure 3.11: (a) Superconducting solenoid with cancellation coil. The main coil (red) and cancellation coil (yellow) are wound from a continuous wire carrying the same current but in opposite directions. (b) The combined effect is a solenoid whose fringe field drops off dramatically with offset from the magnet center.

3.3 Integration of SQUID Amplifier

A SQUID has not been used to detect a trapped electron prior this work. A major challenge is that the Penning trap requires a large magnetic field (e.g. 5 T = 50 kG) while a shielded SQUID will quench unless its ambient field is below 0.005 T = 50 G. At detection frequencies above 100 MHz, the distance between the particle and the detector must be short, and cryogenic since the signal from the single trapped electron is small. For this reason, the SQUID has only ever been used to detect trapped ion [106] whose far lower oscillation frequency (150 kHz) makes it possible to locate the SQUID well outside the large magnetic field volume, using a bucking coil to cancel a large solenoid fringing field.

This section will explore the challenges and methods used to couple a high frequency DC SQUID amplifier to a single electron trapped in a very strong magnetic field.

3.3.1 Shielded Superconducting Solenoid

A new superconducting solenoid with a substantially reduced fringe field was designed and implemented (Figure 3.11) to allow the SQUID to be located near the electron. The magnet consists of two niobium titanium solenoids of two radii connected in series, each carrying the same current, but in opposite directions. At the designed maximum current, the inner coil generates a field of of 7.9 T at the center of the solenoid while the shield coil generates a field of -1.9 T so the net field at the center of the magnet is 6 T. The relative radii of the two coils are chosen such that away from the center of the magnet, the leading term in the net fringe field of the magnet is greatly reduced.

A comparison of the fringe field of our new magnet and the superconducting magnet used in the 2023 g-factor measurement is shown in Figure 3.12. The SQUID amplifier is 50 cm away from the center of the magnet on the mixing chamber. At this position, the fringe field for a 5.5 T field at the center of the solenoid is < 20 mT $= 200$ G.

3.3.2 Double Layer Superconducting Shield

The SQUID we used is fabricated with thin film Nb which will quench in ambient fields of 5 mT = 50 G, so more shielding is required to used the SQUID in our magnetic field. The new magnet allows us to implement a niobium superconducting shield, this shield must be cooled below its superconducting temperature before the magnetic field is applied, i.e. it must be zero-field cooled since if the superconducting shields were cooled in a strong magnetic field, flux would be trapped in the superconducting shield. We rely on the Meissner effect when zero-field cooled for effective shielding.

We can achieve zero-field cooling in two ways: (i) with a second outer high temperature superconducting shield that is cooled before insertion into the magnet, or (ii) by ramping the magnetic field after cooling both shields below their critical temperatures.

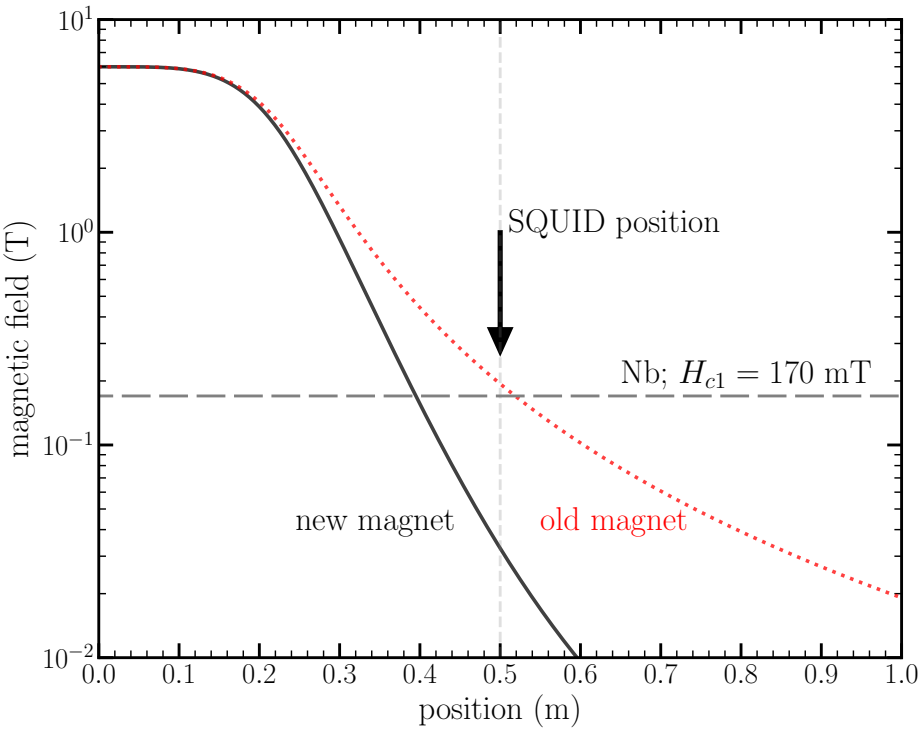

Figure 3.12: Fringe field from the superconducting solenoid compared to the fringe field from an ordinary solenoid.

Historically, in the electron g-factor measurement and other high precision ion Penning trap experiments, the magnetic field is ramped to the desired field and left to stabilize over the period of several weeks to months. In the 2008 g-factor experiment [41], a magnetic field drift of up to 1 ppb/hr even a month after ramping the magnet made it impossible to make high precision $g/2$ measurements during this time. We are able to shorten the settling time after measurements through a more optimized "ringing in" method [42]. In the 2023 g-factor measurement, we achieved drift rates of ~ 0.3 ppb after a day of ramping that enabled measurements at 11 distinct magnetic fields over 6 months. While this demonstration makes ramping after cooling the shields more feasible, we sought to demonstrate a method for operation of the SQUID without having to ramp the magnet.

We designed and tested a double-layer superconducting shield consisting of an outer high-temperature superconducting shield made from bismuth strontium calcium copper oxide 2223

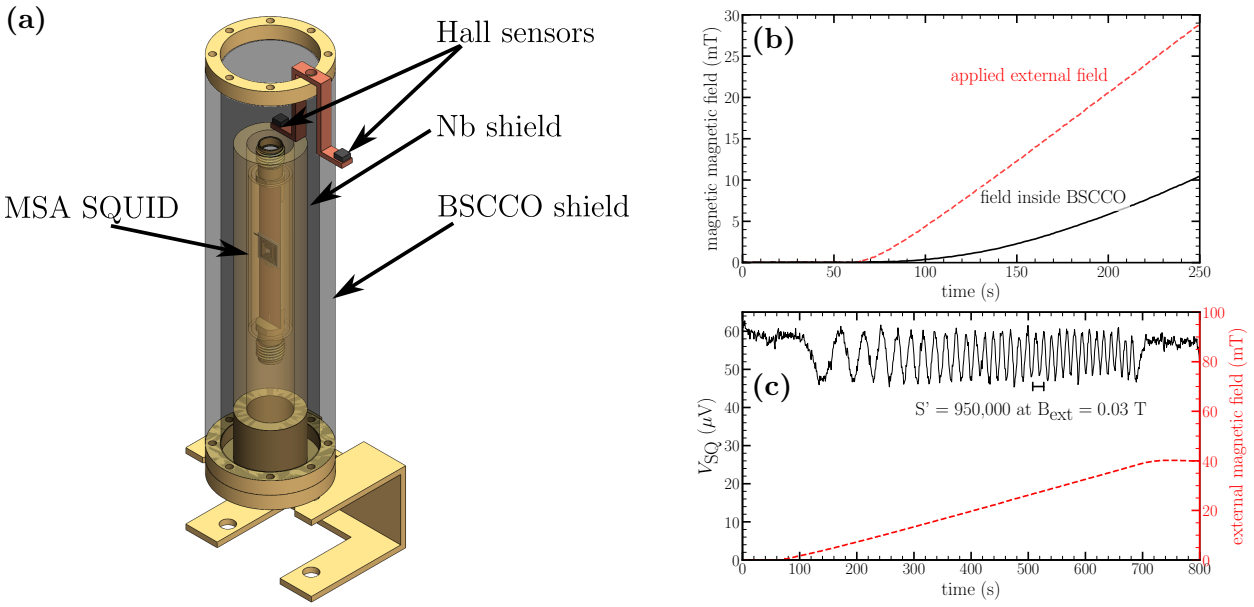

Figure 3.13: (a) Designed two layer superconducting shield consisting of the BSCCO outer shield and inner Nb shield. (b) Measured shielding performance of the dual layer superconducting shield. (c) Measurement of the field penetration into the SQUID loop using the SQUID as a DC magnetic field sensor

(BSCCO, pronounced *bisko*) and an inner niobium shield (Figure 3.13 (a) [42]. BSCCO has a transition temperature of $\sim$ 108 K and critical field of 0.15 T, while niobium has a critical field of around 10 K and lower critical field of around 0.17 T. Both shields are open endcap tubes and in this configuration there is some flux penetration into the shields; this penetration is described in detail here [107]. For all results that follow in this thesis work we use this double layer superconducting shield.

We initially characterized the superconducting shield with two hall sensors, one placed inside the BSCCO shield and a second placed outside of both shields. An external magnetic field is ramped slowly and the field inside and outside the shield is monitored. The results of this test are shown in Figure 3.13 (b). In this configuration, we see enough shielding to use the pre-cooled BSCCO for zero-field cooling of the Nb shield *in-situ*. In a separate test, Figure 3.13 (c), we use the MSA placed inside both shields as a magnetic field sensor. With

the SQUID set to a fixed current bias, we monitor the DC voltage across the SQUID V_{SQ} as the magnetic field is ramped. The voltage drop across a properly biased SQUID oscillates with period Φ/Φ_0, where Φ is the flux penetrating the SQUID loop and $\Phi_0 = 2.07 \times 10^{-15}$ Wb is the flux quantum,

$$\Phi = B_{\mathrm{in}} A \cos\theta, \tag{3.8}$$

where B_{in} is the flux penetrating the Nb shield at the position of the SQUID, A is the area of the SQUID loop ($A \approx 0.01$ mm^2), and θ is the misalignment angle between the SQUID plane and the axis of the applied field. The SQUID mounted such that its plane is parallel to the applied field, $\theta \approx 90^\circ$, but the exact misalignment cannot be measured. We define a modified shield factor S',

$$S' = \frac{B_{\mathrm{ext}}}{B_{\mathrm{in}} \cos\theta} = \frac{\Phi_0}{\Delta B_{\mathrm{ext}}|_{\Phi_0} A}, \tag{3.9}$$

where $\Delta B_{\mathrm{ext}}|_{\Phi_0}$ is the change of the external magnetic field that causes one flux quantum oscillation of the SQUID. This is directly measurable from 3.13 (c). Critically, this definition has folded in the effect of misalignment between the SQUID and the magnetic field axis, and is therefore the figure of merit for SQUID shielding performance. From this test, we determine $S' = 950,000$ for the double layer shield. We expect this to be sufficient for the integration of the SQUID with the Penning trap apparatus.

The first method of zero-field cooling cooling of the shield involves pre-cooling the BSCCO shield before inserting into the fringe field of the magnet. We lower the dilution refrigerator into the liquid helium dewar with the magnet ramped to its set field. The cold gas from the boil off of liquid helium cools the dilution refrigerator. We lower the dilution refrigerator until its lower end is immersed in liquid helium. The fridge is then parked in that position, about 1.5 m away from the center of the magnet, while it is cooled to below the critical temperature of BSCCO. Cooling the fridge to about 100 K takes about 6-8 hours and boils off around 100 L of liquid helium. While we are able to recover some of the liquid helium

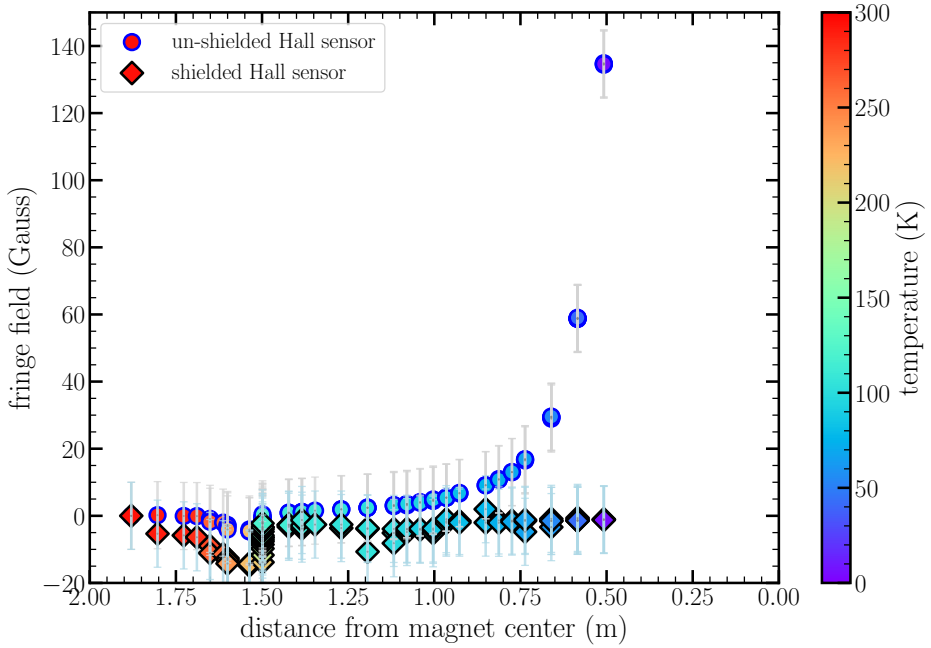

Figure 3.14: Shielding performance with superconducting shields pre-cooled.

locally during the process, this pre-cooling technique proves fairly challenging and costly since we are unable to locally recover all of the liquid helium.

Once the shields are cooled below the critical temperature of the BSCCO, as measured with a calibrated CERNOX sensor placed as close as possible to the shield, we continue to lower the fridge into the magnet dewar until it is seated in place. To characterize the effectiveness of this method we installed two cryogenic hall sensors, one inside the BSCCO shield and the other outside the shield, to monitor the fringe field as the dilution refrigerator is lowered.

The result of our first trial of this scheme is shown in Figure 3.14. Both sensors start off at room temperature and are cooled to about 100 K when parked 1.5 m away from center of the magnet. The relatively small change in the measured fringe field here is due to the temperature dependence of the field-to-voltage transduction function of the Hall sensor. Our measurement of this temperature dependence sets the scale of the error bars on the plot.

Once below the critical field of the BSCCO, we continue to lower the fridge until both sensors are 50 cm away from the center of the magnet, this is where the SQUID is placed during operation.

We observe that while the unshielded sensor measures the increasing fringe field of the magnet as it is lowered, the shielded sensor does not. This suggests that this scheme works effectively in preserving the ambient magnetic field at 1.5 m away from the magnet when placed much closer to the center of the magnet during the dilution refrigerator cool-down. With this scheme we were able to see the SQUID turn on in the dilution refrigerator for the first time. However, as time progressed in the strong magnetic field, the performance of the SQUID degraded and we decided to switch to the second method of zero-field cooling for the shields.

In the second method of zero-field cooling the shields, we pre-cool both shields *in-situ* with the magnet ramped to zero field then ramp the field to a large field. Even in this method, we observe that the gain stability of the SQUID worsens at very large magnetic fields and very low temperatures. We are currently exploring the cause of the instability and are working on alternative designs of the superconducting shield with the goal of eliminating the observed gain instability. In all the results that follow in this chapter, we used on a field of 0.75 T after zero-field cooling *in-situ*. In order to achieve stable SQUID detection at higher fields, an improved magnetic shield has been designed and is being fabricated (Section 3.5.2).

3.3.3 Impedance Matching and Cascaded Amplifiers

A critical consideration in integrating the SQUID-based detection chain is achieving sufficient gain to amplify a signal comparable in magnitude to the noise at 10 mK such that it exceeds the noise level at room temperature. This requires 40–45 dB in power gain and

is achieved with a three-stage cryogenic amplifier chain (Fig. 3.15) consisting of two MSAs and a cryogenic HEMT amplifier (FHX13LG). The gain of each amplifier was measured independently, with the MSAs providing approximately 20 dB of gain (Fig. 3.9) and the cryogenic HEMT about 15 dB gain when optimally biased for cryogenic operation. This gain should be sufficient for our purposes; however, impedance mismatches between stages can lead to power reflections that reduce the effective gain below that required for reliable detection.

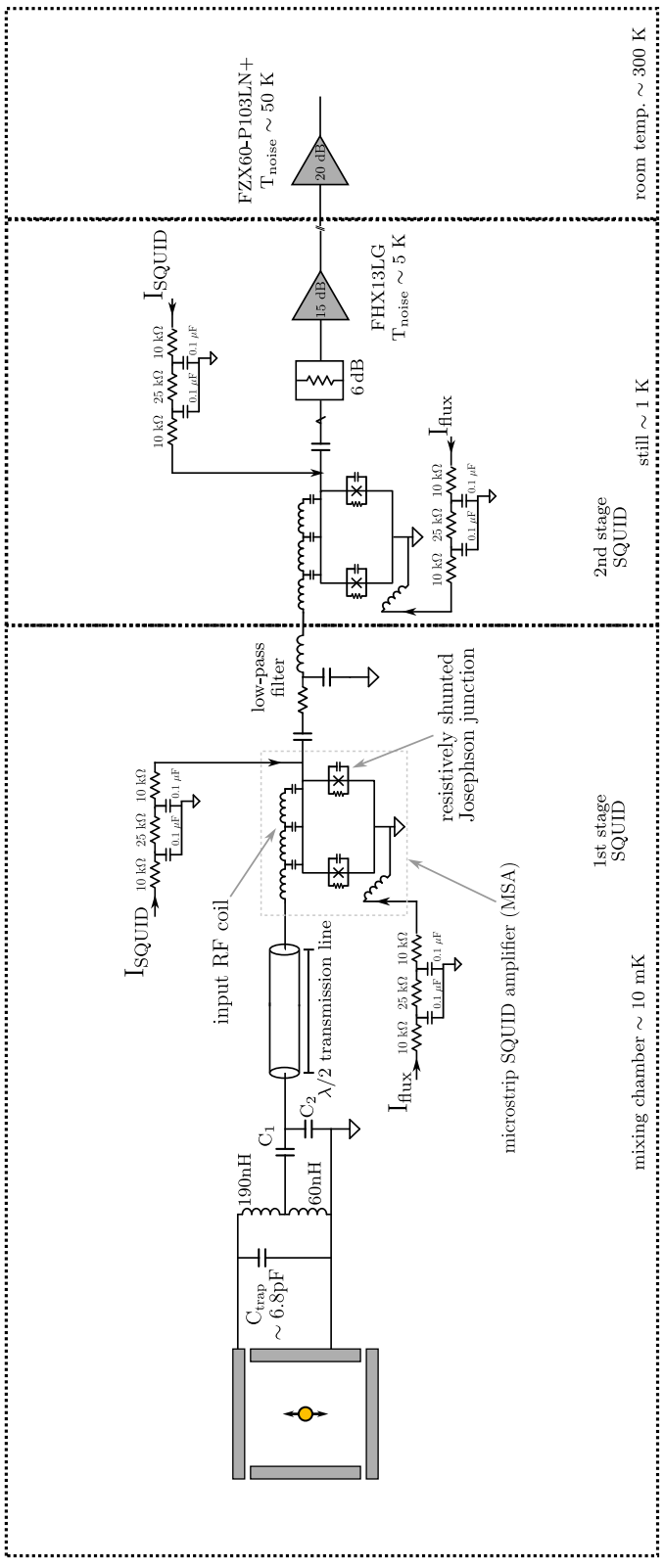

Figure 3.15: Complete SQUID detection chain implemented in the dilution refrigerator. C_1 and C_2 were adjusted between runs for better coupling to the amplifier. For most of the data presented in this thesis these were 2.2 pF and 16 pF respectively.

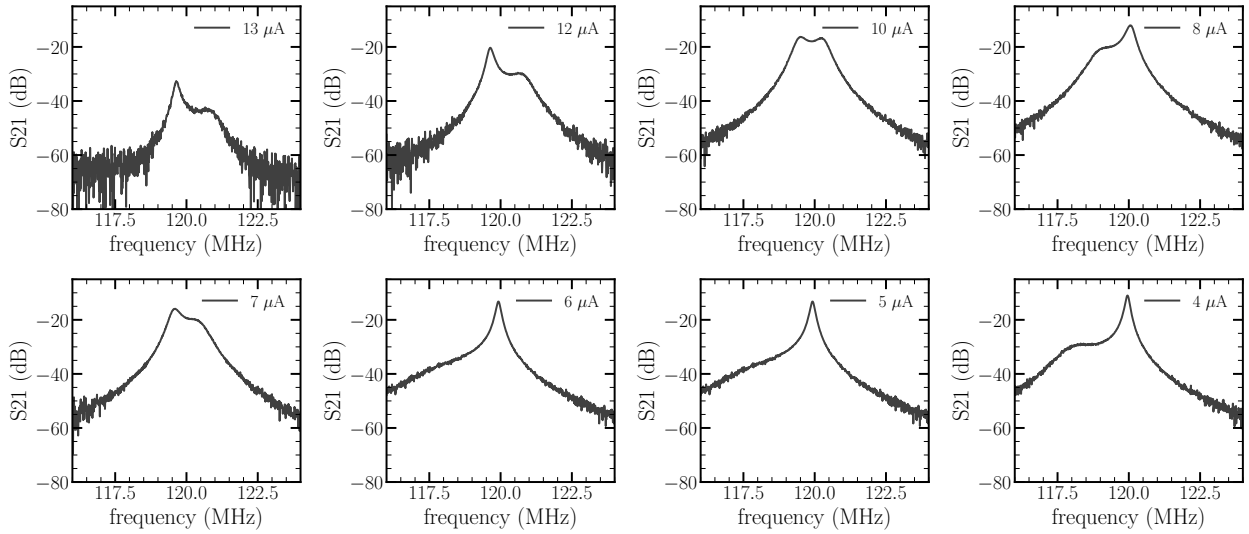

Figure 3.16: Driven detection resonance of the SQUID measured on a network analyzer as the first stage SQUID's flux bias is varied from 4 μA to 13 μA (about one cycle). Measurements are taken at 4 K with drive strength less than -120 dBm. The SQUID bias is held constant during the measurements shown here.

For optimal detection and damping of a single electron in the Penning trap, we implement a tuned circuit designed that cancels the trap capacitance with a high-Q inductor providing the largest possible impedance on resonance (Equation 2.38). At temperatures below 4 K, with $Q \approx 1400$, $\omega_{LC}/2\pi = 120$ MHz, and $L \approx 250$ nH, the resulting impedance is $R_{\text{eff}} \approx 260$ kΩ on resonance. This high impedance must be transformed down to approximately match the input impedance of the microstrip SQUID amplifier (MSA).

The input impedance of MSAs similar to those implemented in this work has been studied extensively [104, 105]; however, quantitative agreement between theoretical models and experimental data remains limited. Furthermore, the narrow dynamic range of the SQUID, which saturates at roughly 100 dBm, necessitates large cryogenic attenuation of test drives that complicates direct impedance characterization. Nevertheless, the available models and measurements provide sufficient guidance for the present implementation.

In constructing the impedance-matching network between the high-impedance LCR cir-

cuit and the MSA, we model the SQUID input as a resistive load of roughly 100 Ω on resonance of its input circuit following prior work [104, 105]. In practice, the MSA input impedance is not fixed, it varies with both SQUID and flux bias currents introducing flexibility. This challenge can also be exploited to optimize coupling *in situ*.

The impedance transformation is achieved using a two-stage matching scheme consisting of an inductive transformer followed by a capacitive divider [42]. On resonance, the impedance presented to the MSA input is given by

$$R_{\text{eff}} = Q\omega_{LC}L\left(\frac{L_2}{L_1+L_2}\right)^2\left(\frac{C_1}{C_1+C_2}\right)^2, \tag{3.10}$$

where $L_{1,2}$ and $C_{1,2}$ are defined in Figure 3.15. This configuration enables transformation of the high-impedance LCR circuit to a value comparable to the effective input impedance of the SQUID.

Because the MSA input and output impedances are bias-dependent, we leverage this tunability to optimize coupling between the tuned circuit and the amplifier. Perfect impedance matching ($R_{\text{eff}} = R_{\text{SQ,in}}$) would significantly degrade the resonator quality factor of the coupled system since the MSA input circuit itself has a low quality factor ($Q \approx 1$, Fig. 3.9). To preserve a high impedance at the trap electrode, we therefore deliberately under-couple the tuned circuit to the MSA inputsacrificing some signal amplitude to minimize damping of the tuned circuit. Figure 3.16 illustrates how the MSA input resonance can be tuned via the SQUID flux bias, with additional fine adjustment available through the SQUID current bias. In practice, both parameters are optimized to maximize the overall Q of the tuned circuit while maintaining sufficient signal gain for reliable single-electron detection.

The corresponding noise resonances for a representative set of bias conditions are shown in Figure 3.17. In this regime, the MSA is biased between 4–5 μA in flux current, intentionally detuning its input resonance to maintain a high effective impedance at the particle, even at

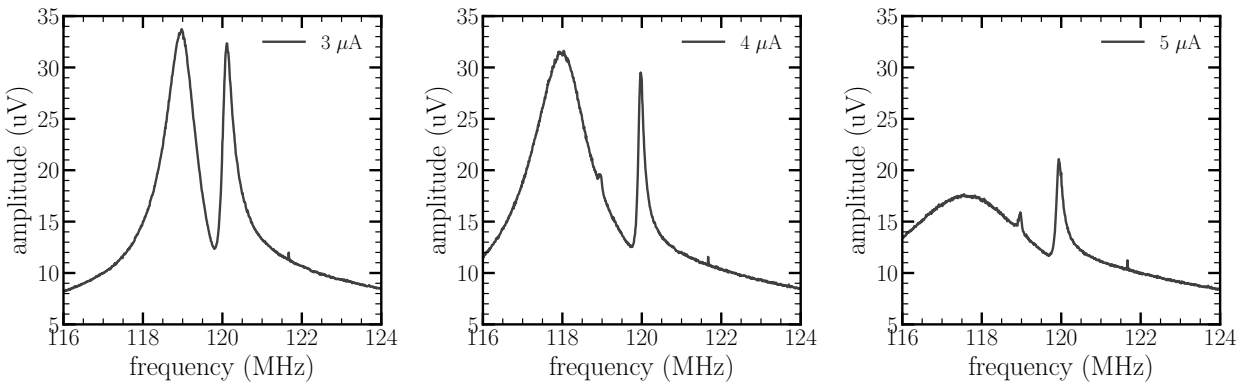

Figure 3.17: Noise resonance at 4 K of the detection circuit as the flux bias is varied while SQUID bias is held constant. The tuned circuit resonance is centered at $\sim$ 120 MHz and the SQUID input resonance is tuned by adjusting the flux bias.

the expense of reduced gain. This trade-off ensures that the electron sees a large impedance to damp its motion while the amplifier still provides adequate gain.

The output of the first-stage SQUID amplifier is fed into an identical second-stage SQUID mounted on the still. Josephson-junction-based devices exhibit intrinsic oscillation frequencies that must be carefully considered when cascading SQUID amplifiers, as unwanted coupling can cause one device to drive the other. For the devices employed here, this oscillation frequency is approximately 1 GHz, well above the resonant frequency of the tuned circuit. As demonstrated in prior work [73, 105], a simple low-pass RC filter can be employed to suppress such oscillations between SQUID stages. This RC filter serves the dual purpose of providing impedance transformation between the dynamic $\sim 10\ \Omega$ output impedance of the first-stage SQUID amplifier and the dynamic $\sim 100\ \Omega$ input impedance of the second-stage.

A cryogenic HEMT amplifier is installed at the output of the second-stage SQUID. Approximately 6 dB of attenuation is inserted between these stages, arising primarily from a well-anchored cryogenic attenuator at this temperature stage. This attenuation serves two purposes: first, it buffers the HEMT input from the dynamically varying output impedance of the SQUID, ensuring a well-defined load; second, it reduces the effective noise temperature

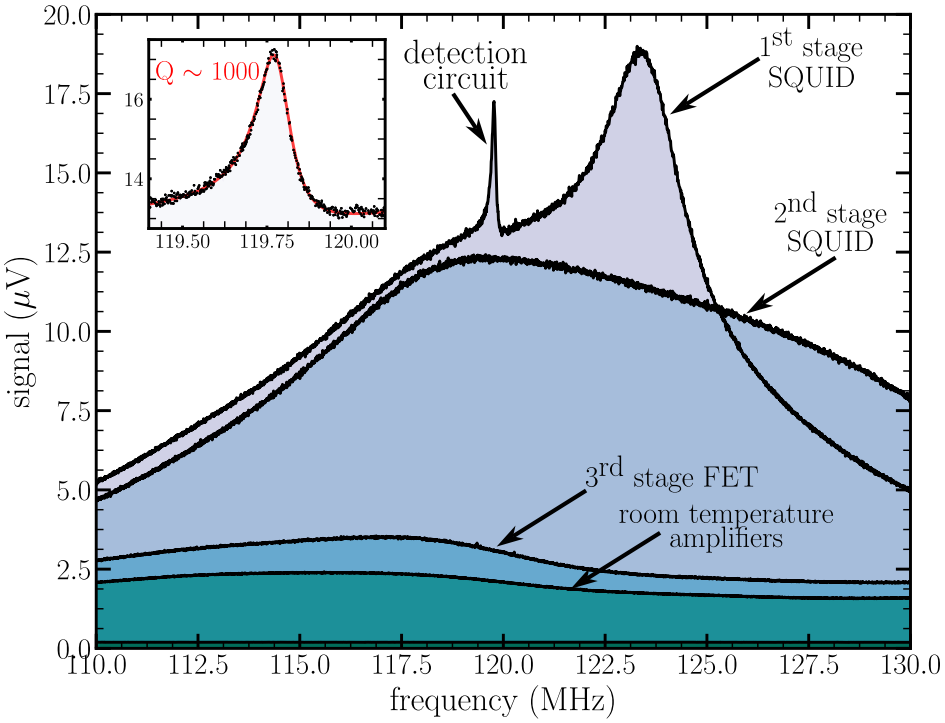

Figure 3.18: Full Noise Resonance at 1 K

at the input of the second-stage SQUID according to $T_{\mathrm{in,SQ2}} \approx \frac{T_{\mathrm{noise,HEMT}}}{G_{\mathrm{SQ}}+6\ \mathrm{dB}}$.

In future iterations of the experiment, we plan to either replace the HEMT third-stage amplifier with a SQUID amplifier or increase the gain of the first-stage SQUID, thereby enabling a simplified two-stage SQUID-based detection chain.

The noise resonance of the entire detection chain at 1 K is shown in Figure 3.18. This is measured by turning on each subsequent amplifier and measuring the noise resonance on a spectrum analyzer. Each amplification stage is clearly resolved. We suspect that the shape of the second stage gain changes with the first stage SQUID on because of the impedance presented at its input from the dynamic output impedance of the first stage. The large peak when the first stage SQUID is on is the MSA input circuit modified by C_2 in the impedance transformation circuit. The center of this peak is tunable with the SQUID and flux bias. The narrower peak on its should is the resonance of the LCR circuit. The center of the MSA input circuit is deliberately detuned in this example. We are able to adjust the SQUID bias

parameters to center the two resonances closer to each other at the expense of the Q of the LCR circuit. This feature of the SQUID detection has been used to vary the damping rate of the particles as discussed in the following section.

3.4 First results with SQUID amplifier detection

3.4.1 First electron dips detected with SQUID amplifier

Electrons have been detected with the SQUID amplifier at dilution refrigerator temperatures through dip detection in the measured noise resonance, Figure 3.19. The ideal noise signal from the LCR circuit is

$$V_N(\omega) = \sqrt{4k_{\mathrm{B}}T\,\mathrm{Re}[Z(\omega)]\Delta f} \tag{3.11}$$

When trapped electrons in the trap are resonant with the detection circuit, they are effectively driven by the noise current of the circuit. This manifests itself as a dip in the noise resonance as the electron "shorts" the LCR circuit at this frequency and the resistance between the detection electrode and ground ideally becomes zero [68].

If there is no additional source of noise to the particle from external drives or trapping voltage variation then a clean noise resonance is observed with the dip falls to the noise baseline of the circuit as observed in this result. We define the signal to noise (SNR) ratio of the dip signal as,

$$SNR = \frac{\text{peak amplitude of noise resonance}}{\text{noise baseline amplitude}} \tag{3.12}$$

In this implementation of the SQUID, we have improved the SNR in two ways:

1. Reduced the noise temperature of the the LCR circuit by reducing the noise temper-

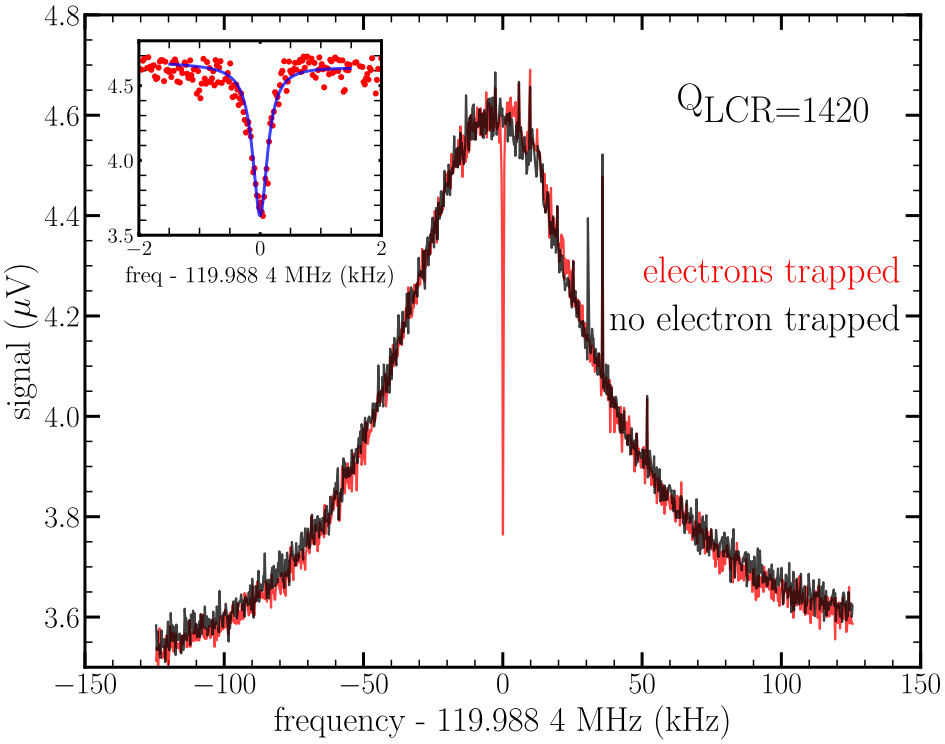

Figure 3.19: 5 electrons in our Penning trap detected by the SQUID amplifier at 200 mK

ature of the amplifier.

2. Improved the peak amplitude of the LCR circuit through improving the effective Z_{eff} to 260 kΩ at 120 MHz.

3.4.2 Single electron counting with SQUID amplifier

We have demonstrated sensitivity sufficient for single electron counting with dips using the SQUID amplifier, Figure 3.20. The full-width half maximum (FWHM) of the dip with a single electron is the axial damping rate $\gamma_z/2\pi$ as defined in 2.38. For N trapped electron, the FWHM is $N \times \gamma_z/2\pi$ [68].

Starting with an empty trap, we load a single electron into the trap using a very weak current on our field emission point and measure its dip FWHM. The same loading parameters

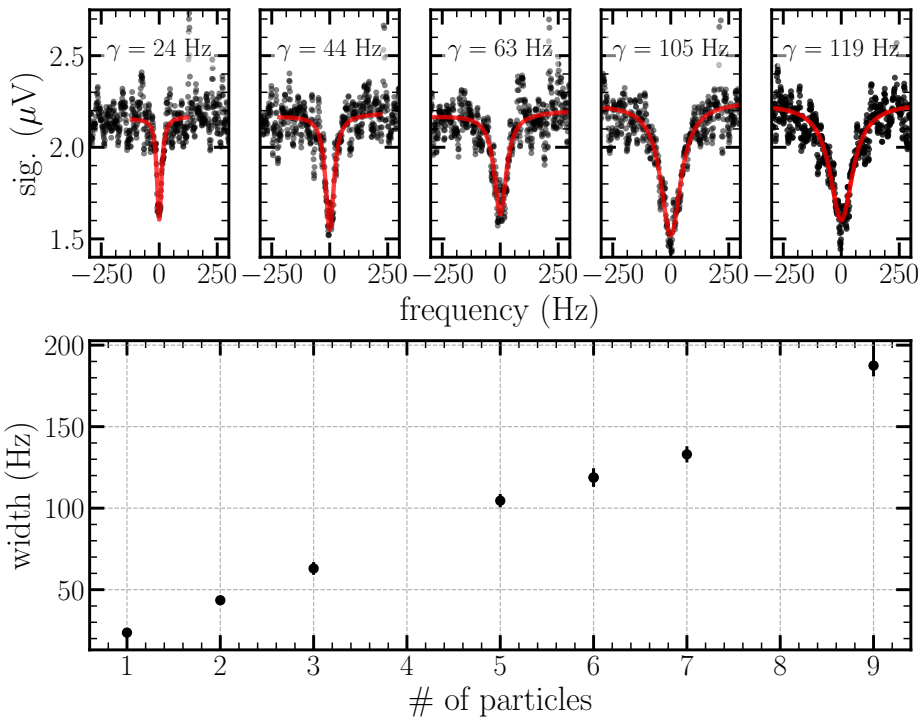

Figure 3.20: Counting of single electrons with the SQUID amplifier using dip width detection

are repeated and subsequent electrons are loaded. The clear quantization of the dip width is observed confirming the estimate of the damping rate for a single electron in our trap as $\gamma_z \approx 20$ Hz. This is a factor of 4 better than what is achieved in the 2023 g-factor apparatus. This improved SNR enables faster single electron detection via dip detection and should enhance precise axial frequency determination.

3.4.3 Demonstration of tunable damping of the electron with the SQUID amplifier

Varying the damping rate has been proposed as a method of circumventing detector backaction broadening in electron g-factor experiments with large magnetic bottles and higher axial temperatures [93, 94]. A demonstration of this scheme has been shown with an HEMT transistor used to detuned the detection resonance from the particle's axial frequency

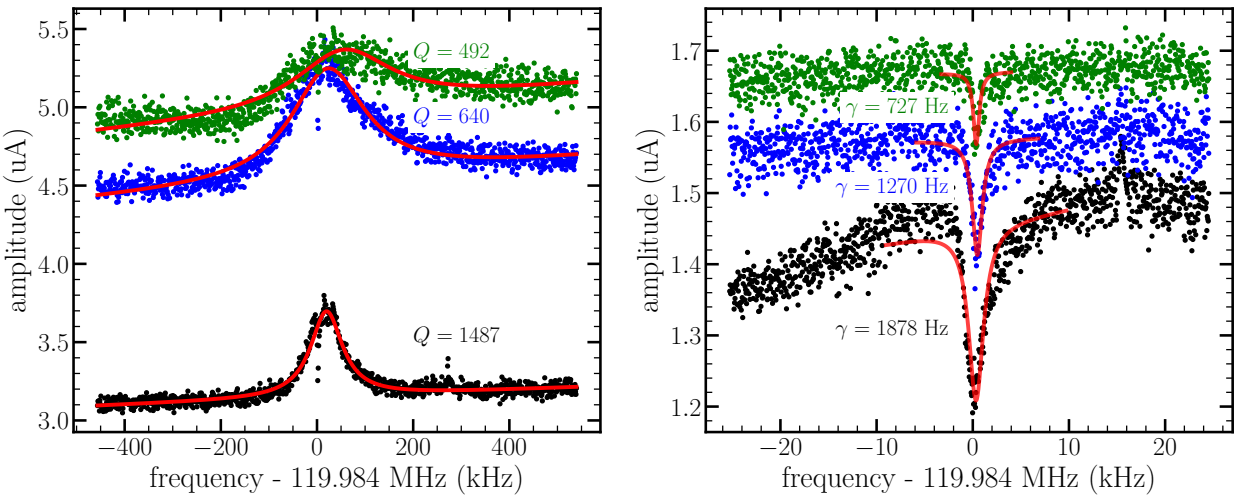

Figure 3.21: Tuning of the axial damping rate of a cloud of electrons using the SQUID amplifier

[108], hence changing the axial damping rate.

We have demonstrated a slight tuning of the axial damping rate using the developed SQUID detection chain as shown in Figure 3.21. In this scheme the Q of the LCR circuit is degraded and its center frequency detuned by leveraging the variable input impedance and, hence, coupling to the SQUID amplifier. A large cloud of about 100 electrons are loaded into the trap and the SQUID bias is varied to three different settings. We observed both a reduction of the Q of the circuit and a corresponding reduction in the axial damping rate resulting in narrower dips for the same electron cloud at different SQUID bias settings.

While a γ_z reduction by a factor of three will be insufficient for improving the precision of our measurement at the current magnetic bottle size and temperatures, this technique may prove useful in schemes where a large magnetic bottle is used at higher temperatures.

The same effect of narrowing the lineshape can be achieved through detuning the particle's axial frequency from the tuned circuit detection resonance. However, detuning the particle's axial frequency is not a feasible approach for a g-factor measurement. The Penning trap DC biases are heavily filtered with RC-filters with time constants of up to 10

minutes. Thus, tuning the particle's axial frequency on- and off- resonance between measurement attempts would be impractical. Therefore, this demonstration of tunable damping of the particle via SQUID bias adjustments provides a feasible path to at least a factor of 3 improvement in the 2023 measurement if the same magnetic bottle size is used and the same axial temperature is achieved. However, since we expect a greatly reduced axial temperature with the SQUID then tunable damping with the SQUID should result in a greatly improved magnetic moment measurement.

3.5 Current Challenges and Future Improvements

Although significant progress has been made in integrating the MSA amplifier with the electron Penning trap, some challenges still remain for stable operation for long periods of time, say for a g-factor experiment. In general, a fluctuating gain output that is worse at lower temperatures and higher magnetic fields. For this reason the results presented have been at the reduced field of 0.75 T where we observe better stability. We will discuss these challenges below along with solutions currently being implemented.

3.5.1 Vibration induced gain fluctuation

We initially observed a large vibration induced gain fluctuation of the SQUID correlated to the the low frequency pulse of the two pulse tube refrigerators mounted to the dewar top for cooling the fridge radiation shields and for local helium reliquefication (see Chapter 2). The observation is shown in Figure 3.22. We drive the at the SQUID input at with two frequencies $v_z - 5$ MHz $= 115$ MHz and $\nu_{\mathrm{mod}} = 5$MHz. The non-linearity of the SQUID mixes these two drives giving a response at 120 MHz. We mix this response down to 5 MHz and monitor the output on a lock-in amplifier referenced to ν_{mod}. A clear 1.2 Hz oscillation is seen with the pulse tube refrigerators (PTR) on vs. off.

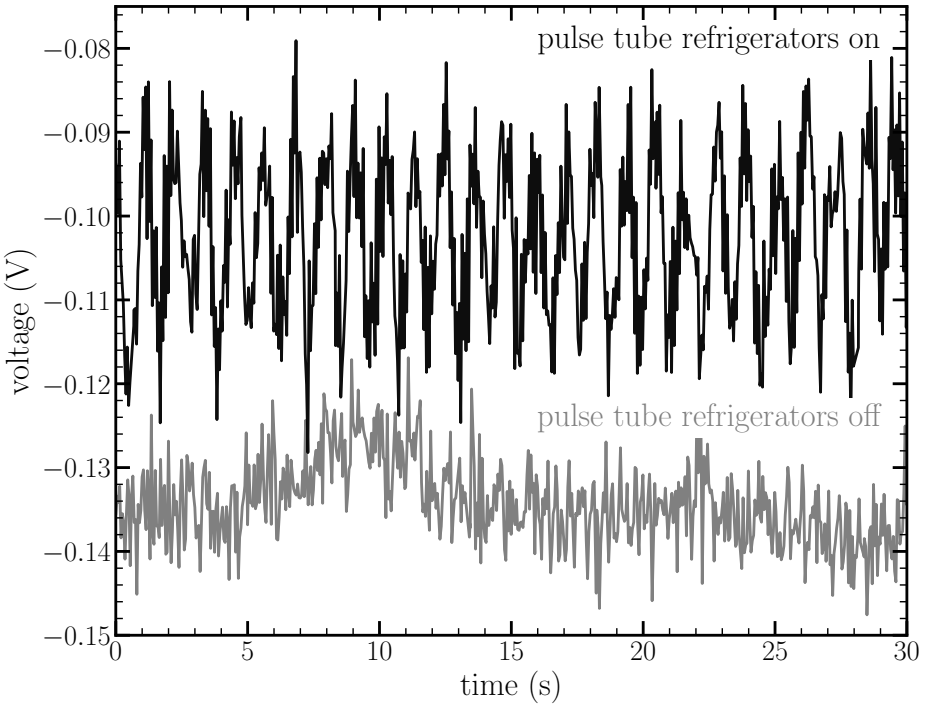

Figure 3.22: Observed vibration induced gain oscillation of the SQUID. The oscillation is correlated to the 1.2 Hz pulse of the pulse tube refrigerators on the dewar.

Since this observation, we have made significant reconfigurations to the mounts between the PTRs and the liquid helium dewar to mitigate this effect. While the progress has been sufficient to make the measurements presented in this work, more work is currently underway to better decouple the dewar top from sources of vibrations through the PTRs, main pumping line to the fridge, and even the numerous cables made to the dilution refrigerator.

As detailed in 2, we have installed an active vibration isolation stage and we have shown that we are able to achieve an ultra-low vibration system when well vibrationally decoupled from the surrounding environment (Fig. 2.21). This is the best vibrational state achievable in the current apparatus and efforts are underway to achieve this condition during normal operation.

At the time of writing, the mechanism between behind the vibration induced gain fluctuation is currently under investigation. We have observed that the fluctuation appears more

severe at lower temperatures. We propose and are investigating the following mechanisms for the observations:

- **Relative motion between the SQUID loop and magnetic field axis driven by dewar vibrations**. The SQUID is an extremely sensitive magnetic flux sensor sensitive to femto-Tesla variations in the flux threading its loop. If the SQUID moves relative to the magnetic field, the amount of flux penetrating the superconducting shield that it measures would vary with time leading to a fluctuation of the measured gain.

- **Microphonic Noise Sources**. Mechanical vibrations of the long DC bias leads to the SQUID in the large magnetic field can produce spurious noise signals at the frequency of oscillation [106]. While we have made significant efforts to mitigate this effect through biasing with with tightly wound twisted pair wires for DC biasing and low pass filtering as close as possible to the SQUID, we plan to further mitigate these effects with a low-frequency flux locked loop [109].

- **Flux motion in the the superconducting shield**. In type II superconductors, when above the lower critical field and in the mixed state, flux penetrates the superconductor and is pinned to defects in the superconductor. The pinned flux can hop between pinning sites resulting in a time varying magnetic field through the SQUID. The source of flux motion can be either thermally activated [110] or mechanically driven [111].

In addition to improving the vibrational decoupling between our experimental system and sources of noise, we are currently developing addressing the observed gain fluctuation through implementing an improved magnetic shield and a low-frequency flux locked loop.

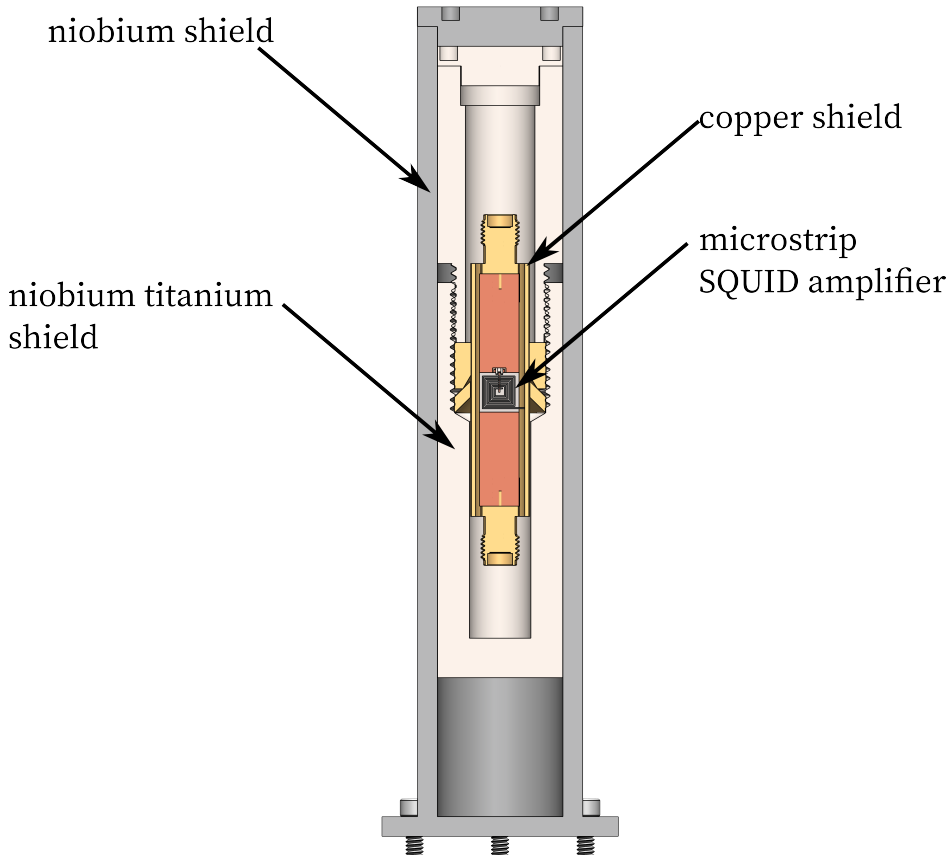

Figure 3.23: Proposed superconducting shield design.

3.5.2 Improved magnetic shielding

We propose a new magnetic shield configuration for improved shielding of the SQUID loop from the ambient 25 mT field, Figure 3.23. With better shielding we aim to reduce the effect of relative motion between the SQUID and applied field and the effect of mechanically driven flux motion.

The proposed shield consists of a niobium (Nb) outer shield, a niobium-titanium (NbTi) middle shield, and a copper inner shield that is the housing of the SQUID amplifier. While previous the previous shield was an open endcap tube, we plan to implement a closed cylinder with small holes for DC and RF cable access positioned at the top of the shield. Each shield is machined out of one piece except of the top cap which is removable.

Ideally, at this field the Nb shield acts as a type I superconductor and we get complete flux exclusion from the Meissner effect. In reality, for bulk Nb, impurities lower its lower critical field and the Nb is sometimes in the mixed state. We are machining the outer shield with high purity Nb (99.95%) to mitigate this and expect to achieve most of the shielding from the Nb shield.

The middle NbTi shield (52.5:47.3 Nb:Ti, 99.9% purity) typically has a low lower critical field $H_{c1} \approx 10 - 100$ mT but very high upper critical field $H_{c2} \approx 8 - 10$ T. The high upper critical field is possible due to strong flux pinning in the material. We aim to leverage this strong flux pinning, to strongly confine flux that penetrates the first Nb shield. This should reduce motion of the motion of flux between pinning sites resulting in a more stable field as seen by the SQUID. Finally, the copper shield of the SQUID housing is meant to be a final shield to reduce field noise through Eddy current shielding.

3.5.3 Low Frequency Flux-Locked Loop

In low-frequency applications, DC SQUIDs are almost universally operated in a flux-locked loop (FLL) configuration [99]. In these application, the FLL is used to either linearize the period $V - \Phi$ response of the SQUID or/and stabilize the long term drift of the SQUID. While the first scheme would be challenging at our frequencies since the feedback loop bandwidth would need to match or exceed the carrier frequency, stabilizing the gain could be useful for our application and could possibly address some of the current challenges.

A flux-bias stabilization scheme has been demonstrated for 777 MHz MSAs similar to the ones we currently employ [109]. We propose using a similar scheme, Figure 3.24 to address the low frequency gain fluctuation that we observed while maintaining the high frequency performance.

The SQUID is biased to its optimal parameters as done in the experiments presented in

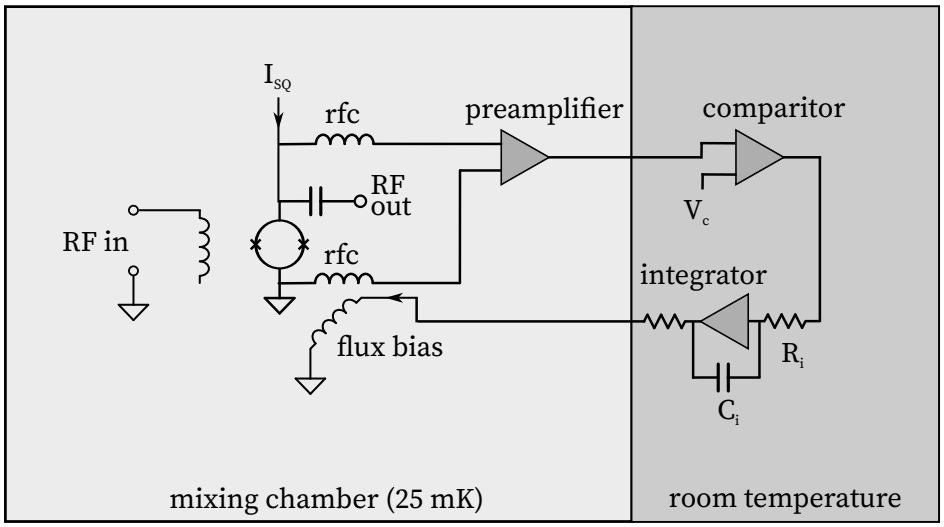

Figure 3.24: Schematic for Proposed Flux-Locked Loop. Noise from the preamplifier used to amplify the small DC voltage drop across the SQUID can be suppressed by cryogenic RF chokes (rfc)

this chapter. The ~ 10 μ V DC voltage drop across the SQUID is amplified cryogenically and measured at room temperature. Large RF chokes are added to these voltage probes to prevent RF noise leakage to the SQUID loop. The amplifier used at this stage can be a second DC SQUID or cryogenic HEMT. In principle, this amplifier can be placed at room temperature but must be carefully implemented as to avoid increasing the noise temperature of the MSA.

The amplified DC voltage drop across the SQUID is passed through a comparator set to $V_c = g_{\text{pre-amp}} \times V_{\text{SQ}}$, where V_{SQ} is the voltage across the SQUID at its optimal bias parameters. Variations in the ambient magnetic field can cause the effective flux bias to drift from its optimal value. When this occurs, the output of the comparator changes resulting in a negative feedback flux applied to the SQUID to cancel the magnetic field fluctuation.

The integrator time constant sets the frequencies of fluctuations that are corrected for. We can select the integrator time constants R_i and C_i such that only field fluctuations at frequencies lower than $g_{\text{SQ}}/2\pi R_i C_i$ will be removed. We are interested in canceling fluctuations

on that are slower than 10 s, the timescale of the gain fluctuations observed.

3.6 Summary

We have detected a single electron with a microstrip SQUID amplifier for the first time. In our current configuration at 120 MHz, the signal from a single electron ($\gamma_z/2\pi = 20$ Hz) is about a factor of four higher than has ever been observed. The noise temperature of the similar MSA's were characterized at 4 K and observed to be a factor of 10 lower than the conventionally used HEMT amplifier. Work is underway to measure the noise temperature of our system at dilution refrigerator temperatures. With our current set-up, in the absence of any spurious source of noise, we expect to be limited by the dilution refrigerator's physical temperature and not the noise temperature of the detector chain.

In the current implementation, the MSA exhibits a low frequency gain fluctuation correlated with vibration that is worse at low temperature and high magnetic fields. While we have been able to significantly reduce the vibration induced gain fluctuation and observe the results presented in this thesis, further work is currently underway to improve the vibration decoupling. Additionally, we have proposed a reconfiguration of the superconducting shield and a scheme for a low-frequency flux-locked-loop that should mitigate the observed gain fluctuation.

The detection of a single electron with improved signal to noise opens the door to a measurement of the electron g-factor at a greatly reduced axial temperature. Although some challenges remain, this could lead to a great improvement in the measurement precision of the electron magnetic moment.

Chapter 4

Microwave Cavity Correction

4.1 Introduction

The metal walls of the Penning trap form a microwave cavity with resonant modes that are typically close to the cyclotron frequency at 5.5 T. The modification of the modes around the single trapped particle compared to free space inhibits or enhances spontaneous emission off- vs. on-resonance respectively, and shifts the measured cyclotron frequency in the trap cavity $\bar{\nu}_c^{\mathrm{cav}}$ from the free-space value needed for the determination of the g-factor [63, 64].

The effect of the particle-trap cavity coupling introduces a small shift to the measured cyclotron frequency in the trap $\bar{\nu}_c$,

$$\bar{\nu}_c^{\mathrm{cav}} = \bar{\nu}_c + \Delta\bar{\nu}_c^{\mathrm{cav}} = \bar{\nu}_c \left(1 + \frac{\Delta\bar{\nu}_c^{\mathrm{cav}}}{\bar{\nu}_c}\right) \tag{4.1}$$

The particle-trap coupling does not shift the spin frequency, but the coupling does shift the measured anomaly frequency $\bar{\nu}_a$ from the free-space value since the anomaly is defined as a

difference between the spin and cyclotron frequency,

$$\bar{\nu}_a \rightarrow \bar{\nu}_a - \Delta\bar{\nu}_c^{\text{cav}} \tag{4.2}$$

The measured g-factor, is therefore shifted by the particle-trap cavity coupling as,

$$\Delta\frac{g}{2}\Big|_{\text{cav}} = \frac{\bar{\nu}_a + \Delta\bar{\nu}_c^{\text{cav}} - \frac{\bar{\nu}_z^2}{2\left(\bar{f}_c+\Delta\bar{\nu}_c^{\text{cav}}\right)}}{\bar{f}_c + \Delta\bar{\nu}_c^{\text{cav}} + \frac{3}{2}\frac{\delta_r}{2\pi} + \frac{\bar{\nu}_z^2}{2\left(\bar{f}+\Delta\bar{\nu}^{\text{cav}}\right)}} - \frac{\bar{\nu}_a - \frac{\bar{\nu}_z^2}{2\bar{f}_c}}{\bar{f}_c + \frac{3}{2}\frac{\delta_r}{2\pi} + \frac{\bar{\nu}_z^2}{2\bar{f}}} \approx \left(1 + \frac{\bar{\nu}_a}{\bar{\nu}_c}\right)\frac{\Delta\bar{\nu}_c^{\text{cav}}}{\bar{\nu}_c}, \tag{4.3}$$

where the final approximation is sufficient for the work discussed in this chapter ($\mathcal{O}\left(10^{-15}\right)$ level). Accounting for this correction requires measuring all the microwave modes that couple to the trapped electron and accounting for the shift in a hybrid re-normalized calculation [41, 42, 112].

The microwave cavity shift alongside the cyclotron lineshape broadening equally comprised the largest systematic limitations in the 2023 g-factor measurement. Lowering the axial temperature and advancing the relativistic detection scheme with the *near*-quantum-limited detector (Chapter 3) clearly enable suppression of lineshape broadening and higher measurement precision. To control the cavity-shift systematic, continued improvements in both the apparatus and theoretical modeling are required.

In this chapter, we first introduce the theory background particle-trap cavity coupling then present a detailed treatment of the cavity shift systematic in the 2023 electron g-factor measurement. This work was an independent calculation of the cavity correction from [42] that was performed in parallel and contributed to the final published result [6]. The remainder of the chapter focuses on how the insights gained from the 2023 measurement informed the design and implementation of the newly developed trap cavity. In this context, we provide the corresponding cavity-shift calculation for the new trap cavity and outline potential paths for further reducing this systematic in future measurements.

4.1.1 Electromagnetic Modes in an Ideal Cylindrical Cavity

We employ closed-endcap cylindrical Penning traps for the electron magnetic moment experiment. The conductive walls of the Penning trap impose the boundary conditions for the electromagnetic fields,

$$E_{\parallel} = 0 = B_{\perp}, \tag{4.4}$$

where $E_{||}$ and $B_{\perp}$ are the parallel component of the electric field and the perpendicular component of the magnetic field respectively. A cylindrical cavity of height $2z_0$ and radius ρ_0 imposing these boundary conditions allows two classes of electromagnetic modes, "transverse-electric" or TE, and "transverse-magnetic" or TM modes. The expressions for the electromagnetic field structure and resonant frequencies are straightforwardly derived in [83]. The resulting resonant mode frequencies ω_{mnp} for TE and TM modes respectively are,

$${}^{\mathrm{TE}}\omega_{mnp} = c\sqrt{\left(\frac{x'_{mn}}{\rho_0}\right)^2 + \left(\frac{p\pi}{2z_0}\right)^2} \tag{4.5}$$

$${}^{\mathrm{TM}}\omega_{mnp} = c\sqrt{\left(\frac{x_{mn}}{\rho_0}\right)^2 + \left(\frac{p\pi}{2z_0}\right)^2}, \tag{4.6}$$

where each mode is indexed by $m, n,$ and p, x_{mn} is the n-th root of the order-m Bessel function ($J_m(x_{mn}) = 0$), and x'_{mn} is the n-th root of the derivative of the order-m Bessel function ($J'_m(x_{mn}) = 0$). The indices describe the nodes of the electromagnetic field structure of each mode: $m = 0, 1, 2, \ldots$, is the number of nodes in the azimuth as it is swept through π radians, $n = 1, 2, \ldots$, is the number of antinodes in the azimuthal component of the electric field along the radius, and $p = 1, 2, \ldots$ for TE modes and $p = 0, 1, 2, \ldots$, for TM modes is the number of antinodes along the axis of the trap-cavity.

4.1.2 Cyclotron Motion in a Microwave Cavity: Lifetime and Frequency Shifts

The coupling between the resonant modes of a microwave cavity and a single trapped electron is explored in great detail in [41,63,64,112–115], we only present the relevant results in this thesis. In a fully re-normalized treatment, the cyclotron frequency shift $\Delta\omega_c^{\text{cav}}$ and modified cyclotron damping rate γ_c at cyclotron frequency ω_c for a single electron at position z and ρ is given by,

$$\Delta\omega_c^{\text{cav}} - \frac{i}{2}\gamma_c = -\frac{i}{2}\gamma_{c;0} + \omega_c \left\{ \Sigma_S \left[\omega_c, z, \rho, Q^{\text{TE}}, Q^{\text{TM}}\right] + \Sigma_P \left[\omega_c, z, Q^{\text{TE}}, Q^{\text{TM}}\right] \right\} \tag{4.7}$$

where Q^{TE} and Q^{TM} are the quality factors of the TE and TM modes respectively, and the free space cyclotron damping rate $\gamma_{c;0}$ is given by,

$$\gamma_{c;0} = \frac{1}{4\pi\epsilon_0}\frac{3m_e c^2}{4e^2\omega_c^2} \tag{4.8}$$

Equation 4.7 includes terms Σ_P and Σ_S which contain the contributions form the parallel plates and cylindrical walls of the microwave cavity. The parallel plate contribution is given by,

$$\Sigma_P(\omega, z) = -r_0 \left[2\sum_{j=1}^{\infty} F\left(4jz_0\right) - \sum_{j=1}^{\infty} F\left(2(2j-1)z_0 + 2z\right) - \sum_{j=1}^{\infty} F\left(2(2j-1)z_0 - 2z\right) \right] \tag{4.9}$$

where,

$$F(z) = \frac{1}{|z|}\left[e^{\frac{i\omega|z|}{c}} \left(1 + \frac{ic}{\omega|z|} - \frac{c^2}{\omega^2 z^2}\right) + \frac{c^2}{\omega^2 z^2} \right] \tag{4.10}$$

The cylindrical wall contribution is given as,

$$\begin{aligned}\Sigma_S\left(\omega,z,\rho,Q^{\mathrm{TE}},Q^{\mathrm{TM}}\right) = &-\frac{r_0}{z_0}\sum_{p=1}^{\infty}\sin^2\left[\frac{p\pi}{2}\left(\frac{z}{z_0}+1\right)\right]\sum_{m=0}^{\infty}(1+\mathrm{sgn}(m))\times \\ &\left[\frac{K_m'\left(\mu_p^{\mathrm{TM}}\rho_0\right)}{I_m'\left(\mu_p^{\mathrm{TE}}\rho_0\right)}R_I\left(m;\mu_p^{\mathrm{TM}}\rho\right)+\left(\frac{p\pi c}{2\omega z_0}\right)^2\times\right. \\ &\left.\left(\frac{K_m\left(\mu_p^{\mathrm{TM}}\rho_0\right)}{I_m\left(\mu_p^{\mathrm{TM}}\rho_0\right)}R_I\left(m;\mu_p^{\mathrm{TM}}\rho\right)-\frac{K_m\left(\frac{p\pi\rho_0}{2z_0}\right)}{I_m\left(\frac{p\pi\rho_0}{2z_0}\right)}R_I\left(m;\frac{p\pi\rho}{2z_0}\right)\right)\right.\end{aligned} \tag{4.11}$$

where,

$$\begin{aligned}\mu_p^{\mathrm{TE}} &= \sqrt{\left(\frac{p\pi}{2z_0}\right)^2-\left[\frac{\omega}{c}\left(1+\frac{i}{2Q^{\mathrm{TE}}}\right)\right]^2} \\ \mu_p^{\mathrm{TM}} &= \sqrt{\left(\frac{p\pi}{2z_0}\right)^2-\left[\frac{\omega}{c}\left(1+\frac{i}{2Q^{\mathrm{TM}}}\right)\right]^2}\end{aligned} \tag{4.12}$$

and,

$$R_I(m;x) = \left(\frac{m}{x}\right)^2 I_m(x)^2 + I_m'(x)^2. \tag{4.13}$$

Here, $\mathrm{sgn}(x)$ is the signum function, $I_\nu(x)$ is the modified Bessel function of the first kind, and $K_\nu(x)$ is the modified Bessel function of the second kind. Note that a limitation of this expression for the cavity shift is that it allows only the aggregate quality factors of the TE and TM modes to be included. Assigning the quality factors to the individual modes of the cavity is not possible with this expression.

Near the resonant mode of the cavity, the cavity frequency shift from a single mode can be approximate in the form of a Lorentzian contribution as,

$$\Sigma_S(\omega,z,\rho) \approx \frac{{}^{(\mathrm{TE,\ TM})}\lambda_{mnp}^2}{\left(\omega\left(1+\frac{i}{2^{(\mathrm{TE,\ TM})}Q}\right)\right)^2 - {}^{(\mathrm{TE,\ TM})}\,\omega_{mnp}^2} \tag{4.14}$$

where $\lambda_{mnp}^{2\ (\mathrm{TE,\ TM})}$ is a parameter that quantifies the coupling strength of each mode to the

trapped electron. Generally, the coupling strength λ_M^2 as a position ρ, z is given by,

$$\lambda_M^2 = \frac{e^2}{m\epsilon_0} \frac{\left|\vec{E}_M(\rho,z)_x\right|^2 + \left|\vec{E}_M(\rho,z)_y\right|^2}{\int_V \left|\vec{E}_M(\mathbf{r})\right|^2 d\mathbf{r}} \tag{4.15}$$

where $\vec{E}_M(\rho,z)_x$ and $\vec{E}_M(\rho,z)_y$ are the magnitude of the component of the electric field in the x and y directions at position (ρ, z).

The specific expression for the mode coupling to a single electron at position z and ρ is given explicitly as,

$$\begin{aligned} {}^{\mathrm{TE}}\lambda_{mmp}^2 &= \frac{2r_0c^2}{z_0\rho_0^2} \frac{-(1+\mathrm{sgn}(m))}{J_m''(x'_{mn})\,J_m(x'_{mn})} \sin^2\left[\frac{p\pi}{2}\left(\frac{z}{z_0}+1\right)\right] R_J\left(m; x'_{mn}\frac{\rho}{\rho_0}\right) \\ &= \frac{2r_0c^2}{z_0\rho_0^2} \frac{-1}{J_m''(x'_{mn})\,J_m(x'_{mn})} \quad (\text{ at } \rho=0 \text{ and } z=0 \text{ for } m=1 \text{ and } p\text{-odd }) \end{aligned} \tag{4.16}$$

for TE modes, and

$$\begin{aligned} {}^{\mathrm{TM}}\lambda_{mnp}^2 &= \frac{2r_0c^2}{z_0\rho_0^2} \frac{1+\mathrm{sgn}(m)}{J_m'(x_{mn})^2} \left(\frac{p\pi}{2z_0}\frac{c}{{}^{\mathrm{TM}}\omega_{mnp}}\right)^2 \sin^2\left[\frac{p\pi}{2}\left(\frac{z}{z_0}+1\right)\right] R_J\left(m; x_{mn}\frac{\rho}{\rho_0}\right) \\ &= \frac{2r_0c^2}{z_0\rho_0^2} \frac{1}{J_m'(x_{mn})^2} \left(\frac{p\pi}{2z_0}\frac{c}{{}^{\mathrm{TM}}\omega_{mnp}}\right)^2 \quad (\text{ at } \rho=0 \text{ and } z=0 \text{ for } m=1 \text{ and } p\text{-odd }), \end{aligned} \tag{4.17}$$

for TM modes. Here, $R_J(m;x)$ is defined as,

$$R_J(m;x) = \begin{cases} \frac{m^2}{x^2}J_m(x)^2 + J_m'(x)^2 & (x \neq 0), \\ \frac{1}{2} & (x=0, m=1), \\ 0 & (x=0, m\neq 1). \end{cases} \tag{4.18}$$

For an electron at exactly the trap center, that is $\rho, z = 0$, the mode coupling λ_M^2 vanishes except for modes where $m = 1$ and p-odd. These modes are referred to as strong coupling

modes.

We can write the correction to the cyclotron frequency and the modified damping rate from a single resonant mode at frequency ω_M and coupling strength λ_M as

$$\Delta\omega_c^{\text{cav}} - i\frac{\gamma_c}{2} = \frac{\omega\lambda_M^2}{\omega^2 + i\omega\Gamma_M - \omega_M^2} \tag{4.19}$$

where Γ_M is the full-width at half maximum, therefore $\Gamma_M = \omega_M/Q_M$. We note that while the full re-normalized correction correction only allows for a generic Q for TE and TM modes, the single mode approximation allows us to assign different quality factors for each mode. Both the full re-normalized expression and the single mode approximation is utilized to calculate the cavity shift systematic as will be discussed in the following section.

Note that the cavity correction $\Delta\omega_c^{\text{cav}}$ is independent of the mode Q when the cyclotron frequency is far off-resonance,

$$\Delta\omega_c^{\text{cav}} \approx \frac{\omega\lambda_M^2}{\omega^2 - \omega_M^2} \left(|\omega - \omega_M| \gg \Gamma_M\right) \tag{4.20}$$

This implies that the critical parameters for the accurate determination of the cavity shift when the particle's cyclotron frequency is far off-resonance with a cavity mode are the mode frequency ω_M and the coupling strength λ_M^2 and not the Q of the mode.

However, we also note here that inhibition of the cyclotron damping rate will be limited by a cavity with a poor quality factor and this is undesirable in two ways. First with a poor cavity Q, the cyclotron lifetime is shortened making it difficult to resolve quantum jumps, and, second, the width of the measured anomaly lineshape is proportional to γ_c, therefore a larger γ_c would result in a less precise measurement of the anomaly frequency.

4.2 Cavity Correction in the 2023 Measurement

The cylindrical Penning trap used for the electron magnetic moment measurement is not an ideal right circular cavity. Holes are introduced on-axis for particle access and slits are introduced in the walls of the trap-cavity to form the electrodes of the Penning trap. Additionally, the surface resistance of the walls of the cavity, limited by both the classical skin-effect and anomalous skin-effect at the temperatures and frequencies achieved, introduce significant loss of to the microwave cavity. The result of the imperfect cylindrical cavity is that the modes measured in the cavity are shifted from the ideal case. The re-normalized correction (equation 4.7) assumes the ideal cavity. Therefore, for an accurate determination of the microwave cavity shift, the resonant modes of the cavity are measured and the correction is modified to include the measured cavity modes.

There are two methods to measure the microwave cavity modes *in-situ* using either a single electron or a large cloud of electrons [113–115]. Mapping of the modes with a single electron is described in detail in [41, 42]. It requires the direct measurement of the cyclotron damping rate of a single electron excited to a high cyclotron state. This method is slower, since it relies on measuring the strongly inhibited cyclotron decay off-resonance, and provides less accuracy since we are unable to measure γ_c accurately on-resonance where there is enhanced spontaneous emission. Nevertheless, mapping the microwave modes with a single electron is a useful tool as the mechanism is better understood than with a cloud. Furthermore, it is a useful tool for systematic checks as the cyclotron damping rate can be measured as the particle can be moved axially and radially.

To extend the mapping of cavity modes, we employ a parametrically driven cloud of electrons; the details of this technique are presented in the next section.

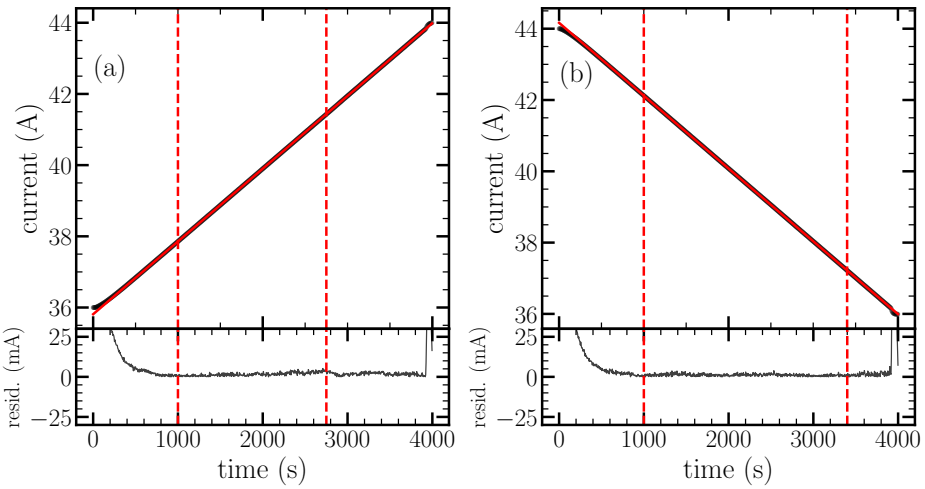

Figure 4.1: Measured magnet current vs time during the mode map sweep. (a) is current swept up and (b) is current swept down. We only use the regions between the red lines where the current sweep linearly maps to sweep time.

4.2.1 Mode Mapping with a Cloud of Electrons

The synchronization of the driven axial motion of a driven cloud of electrons is a sensitive fast probe of the the cyclotron damping rate γ_c as first observed in [113–115]. The cloud of electrons are parametrically driven to large axial oscillations with a drive at twice the axial frequency. The center of mass motion of the driven cloud is detected through its image charge on the detection electrode.

The exact mechanism of the coupling between the parametrically driven motion and the cyclotron damping rate has not been fully understood but is discussed in detail in the Appendices of [41, 42]. As the electrons are driven to large oscillation amplitudes, the internal motion of the cloud is excited as well. The internal motion of the cloud is cooled at a rate proportional to the cyclotron damping rate γ_c. Close to resonance, where γ_c is large, the internal motion of the cloud is efficiently cooled and the parametric excitation drives the center of mass motion to large oscillation amplitudes. In contrast, off-resonance, the internal motion of the cloud is weakly cooled and the parametric response remains at

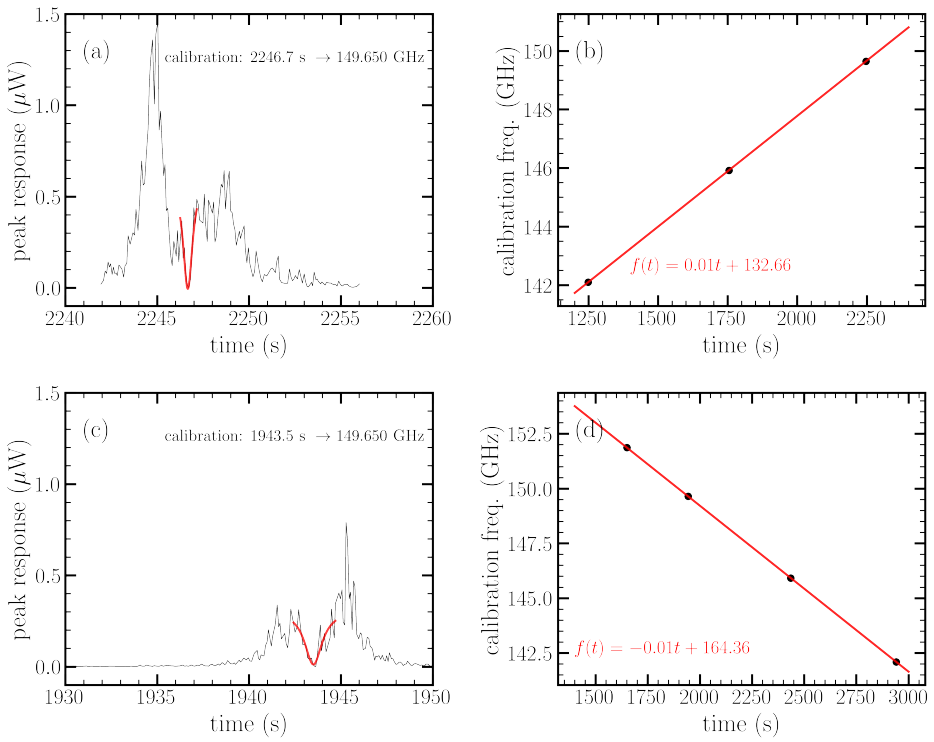

Figure 4.2: Calibration of Mode Mapping Scans. Microwave drives at fixed calibration frequencies are applied and corresponding dips are observed in the spectra (left panels). Through recording the time where we observe the dip and the calibration frequency, we determine a calibration function of sweep time to frequency (right panels). (a) and (b) are for the sweeps up in frequency and (c) and (d) are for the sweeps down in frequency

smaller amplitudes. The parametric response thus yields a response where the center of mass amplitude, and hence detected driven signal, is proportional to the cyclotron damping rate. We use this response to carefully map the modes of the microwave cavity *in-situ*.

Calibrated Mode Maps

We utilize the fast and sensitive response of the parametrically excited cloud of electrons to map the cavity modes by monitoring the parametric response as the cyclotron frequency of the cloud of electrons is varied via sweeping the magnetic field of the superconducting magnet. The voltage output of the magnet supply can be monitored and converted to the current through the solenoid since the inductance of the solenoid is known. However, an accurate

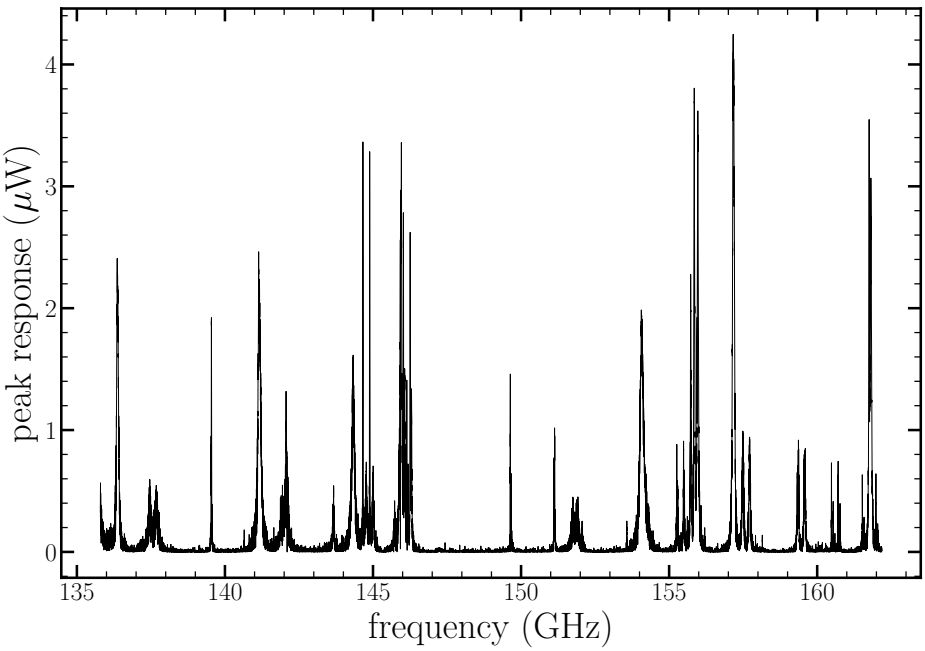

Figure 4.3: Calibrated ode map of trap cavity from 140 GHz to 160 GHz obtained with a cloud of parametrically driven electrons. The methodology is described in text.

conversion of the sweep current to cyclotron frequency must be performed to produce an accurate microwave mode map. We determine the current output of the power supply as a function of sweep time, Figure 4.1. Due to the large inductance of the superconducting solenoid, the current response of the system is non-linear at the start and end of the sweep. We fit the current response as a function to time to a line and truncate the data used in the parametric mode map to the region where the current change is linear with time to less than 5 mA.

We now have a parametric response signal that is linear with the sweep field and hence cyclotron frequency. The parametric response signal is indexed to the sweep time, and now what is required is a conversion of sweep time to cyclotron frequency. This calibration is achieved through applying a microwave drive to the cloud of electrons at known frequencies. When the cyclotron frequency of the cloud of electrons is resonant with the applied drive, the internal motion is significantly heated and the oscillation amplitude of the center of

mass motion, and hence signal, is significantly reduced. The corresponding dip in the parametric signal is correlated with the microwave drive at a recorded timestamp. We repeat the calibration measurement a several different microwave drive frequencies and generate a calibration function of sweep time to cyclotron frequency.

The outlined calibration procedure is shown in Figure 4.2. We repeat the calibration procedure in both a sweep up in frequency and down in frequency and check the linearity of the response. Now, the measured parametric response as a function of sweep time is converted to cyclotron frequency. An example of one such calibrated mode map is shown in Figure 4.3. The mode map is measured with a sweep up and down in current to cross-check the calibration procedure. The modes are fitted to Lorentzian functions and the center frequency is compared in the up and down sweeps. The discrepancy in the measured mode frequencies in the calibrated up and down sweeps is the calibration error and is the uncertainty in the measured mode frequencies. The full mode maps across the cyclotron frequency range 50 GHz to 165 GHz is published in [42] along with the measured mode frequencies and calibration error.

4.2.2 Calculated Correction to *g*-factor

We use the measured mode frequencies to find the best-fit for the half-height z_0 and radius ρ_0 of the trap cavity. These were determined to be $z_0 = 3906\ (35)\ \mu$m and $\rho_0 = 4539\ (31)\ \mu$m and were used as inputs to the re-normalized cavity shift correction function, Equation 4.7. This correction on its own is insufficient to correct for the cavity shift since it does not capture the measured cavity mode frequencies exactly. The observed discrepancy between the measured mode frequency and the calculated mode frequencies using the best fit parameters are shown in Figure 4.4.

We account for the discrepant mode frequencies by building a hybrid re-normalized correc-

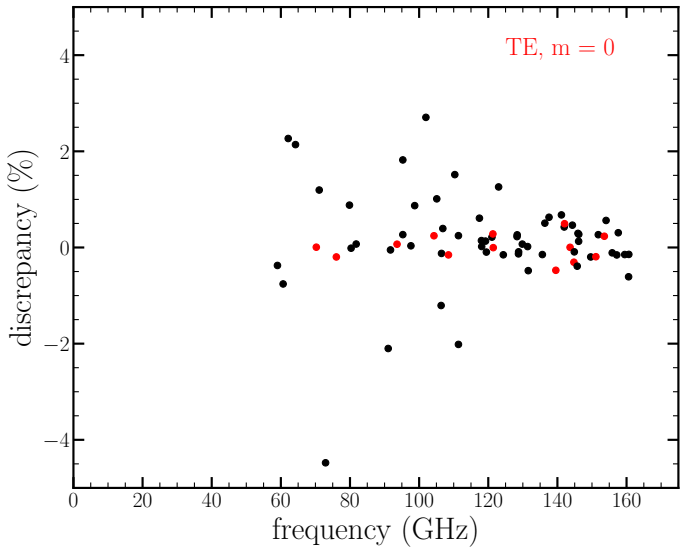

Figure 4.4: Measured mode frequency discrepancies from ideal cavity with dimensions $\rho_0 = 4539$ μm and $z_0 = 3907$ μm determined from the best fit parameters to the measured mode frequencies. We have observed that TE modes with m=0 (red) show better agreement with the idealized calculation.

tion function where Lorentzian single mode approximation, equation 4.19, for each measured mode is subtracted from re-normalized correction function using the best fit cavity parameters then the contribution from each measured mode is added back to the correction function with the measured resonant frequency and the measured quality factor. We found that we are able to exactly subtract the contribution from individual modes in the re-normalized function as long as the input quality factors for TE and TM modes are exactly equal. In the correction function we use ${}^{\mathrm{TE}}Q = {}^{\mathrm{TM}}Q = Q^{(0)} = 3000$, about the average Q observed experimentally.

The hybrid re-normalized correction function is given explicitly as,

$$\Delta\omega_c^{\mathrm{cav}} - \frac{i}{2}\gamma_c = -\frac{i}{2}\gamma_{c;0} + \omega_c\left\{\Sigma_S\left[\omega_c, z, \rho, Q^{(0)}, Q^{(0)}\right] + \Sigma_P\left[\omega_c, z, Q^{(0)}, Q^{(0)}\right]\right\} + \sum_{\substack{\text{all measured}\\ \text{modes}}}\left(-\frac{\omega_c\lambda_M^{2(\text{ calc. })}}{\omega_c^2 + i\omega_c\Gamma_M^{(\text{calc. })} - \omega_M^{(\text{ calc. })\,2}} + \frac{\omega_c\lambda_M^{2(\text{ est. })}}{\omega_c^2 + i\omega_c\Gamma_M^{(\text{meas. })} - \omega_M^{(\text{ meas. })\,2}}\right), \tag{4.21}$$

where the terms denoted with the superscript (calc.) are the calculated using the best fit parameters for the cavity radius and height. $\Gamma_M^{(\text{meas.})}$ and ω_M are the measured mode full-width at half-maximum (FWHM) and resonant frequency respectively. In accounting for the empirical resonances, $\lambda_M^{2\,(\text{est.})}$ is the only parameter that cannot be directly measured and contributes the largest uncertainty to the correction function. In the calculation, we estimate $\lambda_M^{2\,(\text{est.})}$ as the value of with the best fit parameters for the cavity dimensions.

We account for the uncertainty in $\lambda_M^{2\,(\text{est.})}$ through a dimensional argument based on empirical observations. The coupling strength is a measure of the electric field at the position of the electron normalized to the electric field of the cavity resonance across the entire cavity, Equation 4.15. $\lambda_M^{2\,(\text{est.})}$ therefore scales as (cavity length)$^{-3}$ while the resonant mode frequencies, Equation 4.6, scale as (cavity length)$^{-1}$. The observed RMS discrepancies between the measured and calculated mode frequencies is 1.7 %, Figure 4.4. Therefore, we assigned an error of 5.1 % on $\lambda_M^{2\,(\text{est.})}$, three times the observed mode frequency discrepancy from the best fit cavity parameters. This uncertainty on the coupling strength is the largest contribution to the total uncertainty of the cavity correction. We account for this uncertainty by calculating the cavity correction with $\lambda_M^{2\,(\text{est.})}$ varied $\pm 5\%$ for each mode. The difference between the cavity correction with $\lambda_M^{2\,(\text{est.})}$ varied is assigned the uncertainty on the correction to the cyclotron frequency.

The calculated correction to the cyclotron frequency as a function of the cyclotron frequency using the hybrid re-normalized calculation along with its uncertainty as described in this thesis is presented in Figure 4.5. The result acted as a cross-check to the calculation performed in [42] and informed the uncertainty from the cavity shift calculation reported in [6]. Furthermore, the lessons learned in the treatment of the cavity shift systematic in this measurement informed the design of the new trap cavity designed for the next generation of the electron/positron measurement.

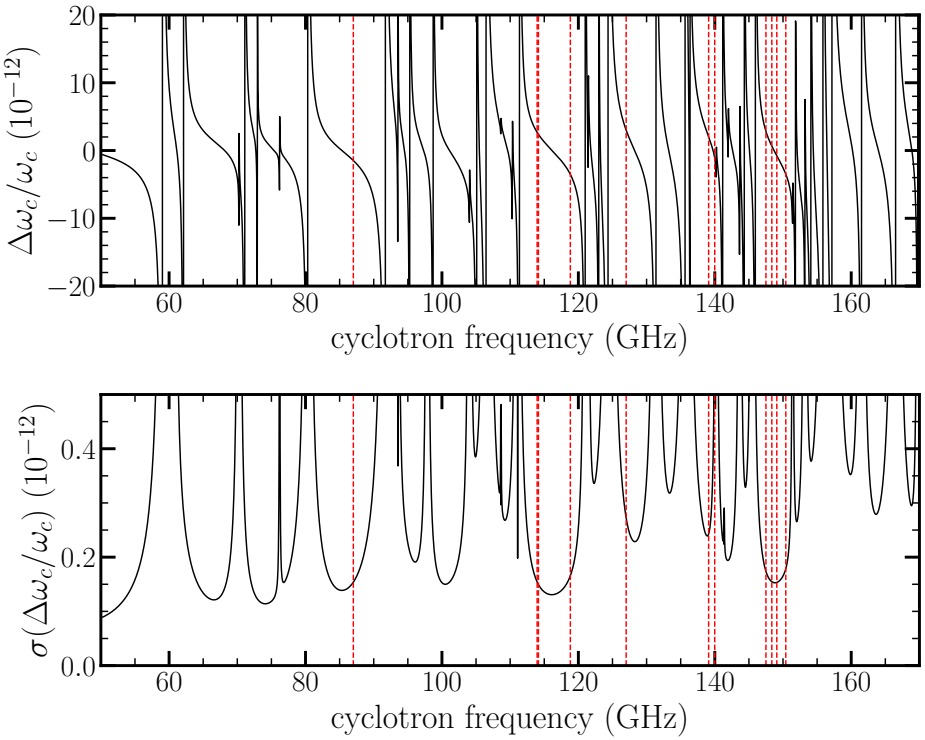

Figure 4.5: Calculated Cavity Correction and Uncertainty in the 2023 g-factor measurement. The red broken lines indicate where the 11 g-factor measurements were taken.

4.2.3 Limitations of the Cavity Correction Calculation

There are two main limitations of the current procedure for determining the cavity shift of the measured cyclotron frequency. The first is the uncertainty assigned to the coupling parameter as previously discussed and the second is contribution from higher frequency modes that we are unable to measure directly. Our superconducting magnet is only capable of ramping its field to 6 T; as a result, the largest cyclotron frequency that can be probed is about 160 GHz. Modes in the cavity that are above this frequency cannot be measured and precisely accounted for. While the error contribution from these higher order modes were not dominant in the 2023 measurement ($\Delta g/2 \sim \mathcal{O}(10^{-13})$), accounting for the higher frequency modes may be relevant in future higher precision measurements.

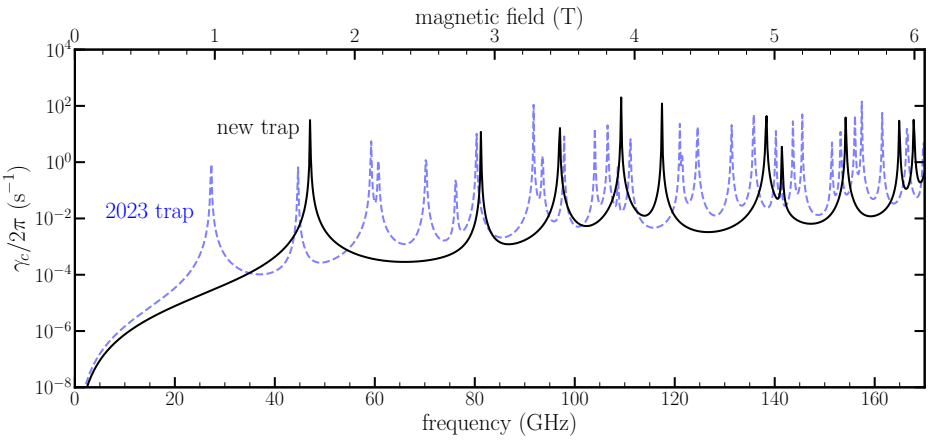

Figure 4.6: Comparison of the damping rate in the 2023 trap (blue broken line) vs. designed trap (black line). While there are over 25 strongly coupled modes from 0- 170 GHz in the old cavity, there are less than 10 in the new cavity.

4.3 Cavity Mode Shifts in the New Trap

The design principle of new trap cavity presented in this thesis is to improve the electrostatic trap anharmonicity, as discussed in Chapter 2, and to address the cavity shift systematic limitation. The latter is the subject of this section of this thesis.

The electrostatic requirements of the trap fixed the relative dimensions of the trap ρ_0/z_0, the size of the trap cavity is a free parameter. We have chosen to construct a 5 times smaller trap by volume in this thesis ($z_{0,2023}/z_{0,\text{new trap}} \approx 1.6$). Since the interval between modes is inversely proportional to the trap size, the reduction of the trap volume has increased the spacing between the modes of the cavity. Additionally, with the reduced trap size the lowest frequency mode that couples to the cyclotron motion at the center of the trap is 47 GHz in this trap compared to 27 GHz in the trap used for the 2023 measurement. We refer to this region as the *below-cutoff* frequency region, and it offers an intriguing opportunity for future measurements as the shift here is dominated by the contribution from the lowest mode.

The calculated cyclotron damping rate in the new trap vs. the trap used in the 2023 measurement is shown in Figure 4.6. The reduced mode density is clear, and the new trap

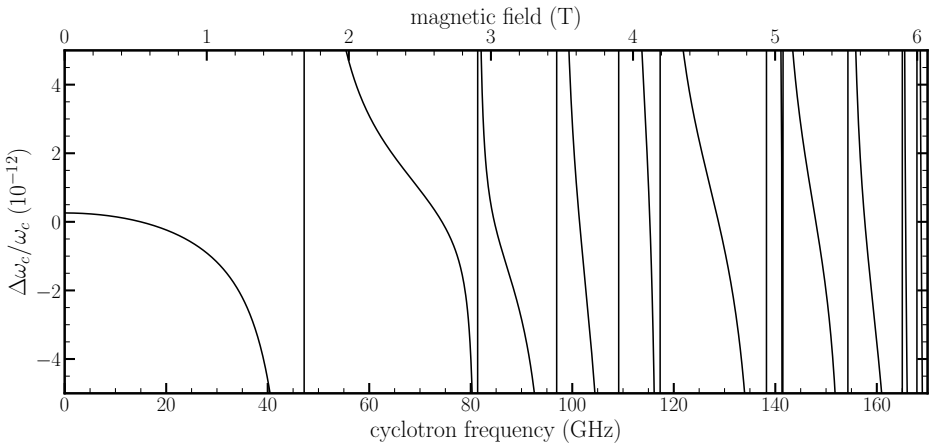

Figure 4.7: Calculated cavity Correction in the New Trap-Cavity. There are several attractive regions between strongly coupled modes for future g-factor measurements.

offers many more frequency regions where a the cyclotron damping rate is lower than for the previous trap by a factor of 5-10 and are attractive for future measurements. This is because the width of the measured anomaly lineshape scales as the the cyclotron damping rate γ_c, therefore a 5-10 times smaller γ_c would result is a 5-10 times reduced anomaly linewidth.

The calculated cyclotron frequency cavity shift as a function of frequency across the full range accessible by our magnet is shown in Figure 4.7. In this calculation we have assumed a mode Q of 3000 for all modes as was used in the 2023 measurement. Here, many attractive regions exist for future measurements. For example, above cut-off frequency, there are many 15-20 GHz wide regions uninterrupted by strongly coupled modes. To demonstrate this, we have calculated the cavity shift of the trap used in the 2023 measurement on the same axis as the new trap cavity in Figure 4.8 between 140 GHz and 160 GHz, where four measurements were performed as denoted by the red diamonds. While in the 2023 trap there are 8 strongly coupled modes in this region, in the new trap there are only two.

In Figure 4.8, we include the estimation of the uncertainty in the cavity correction under the same assumption for the dominant uncertainty, $\lambda_M^2 = \pm 5\%$. Even with the significantly reduced mode density, the cavity correction uncertainty in this region is comparable under

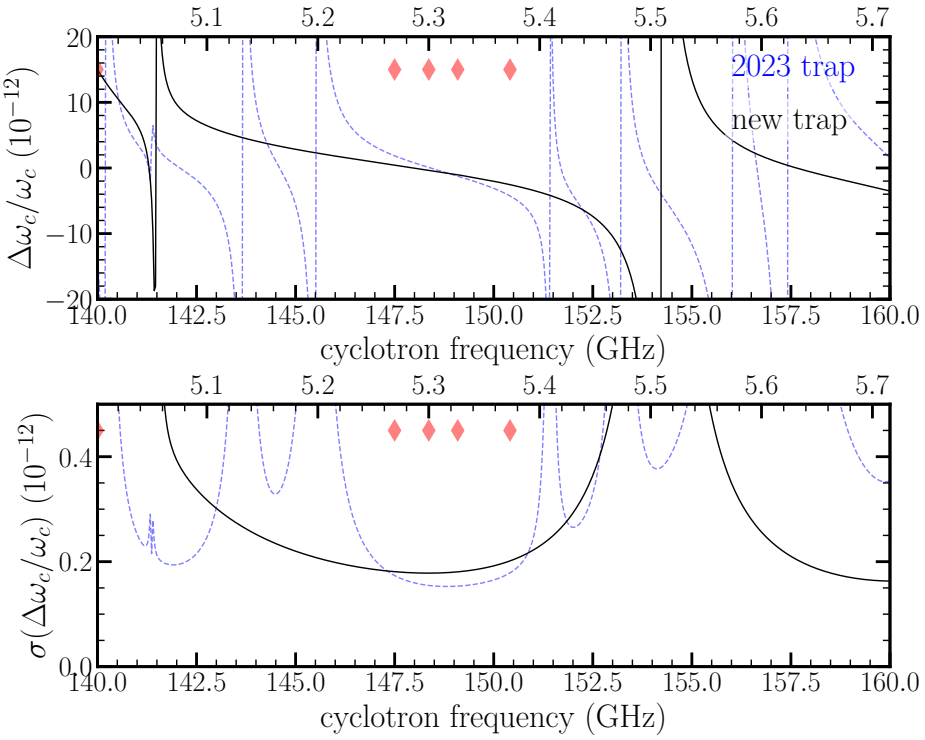

Figure 4.8: Comparison of the cavity correction in the 2023 trap vs. designed trap. The red diamonds indicated where g-factor measurements were performed in the 2023 measurement. In the 140-160 GHz range there were 7 strongly coupled modes, in the new cavity there are only two.

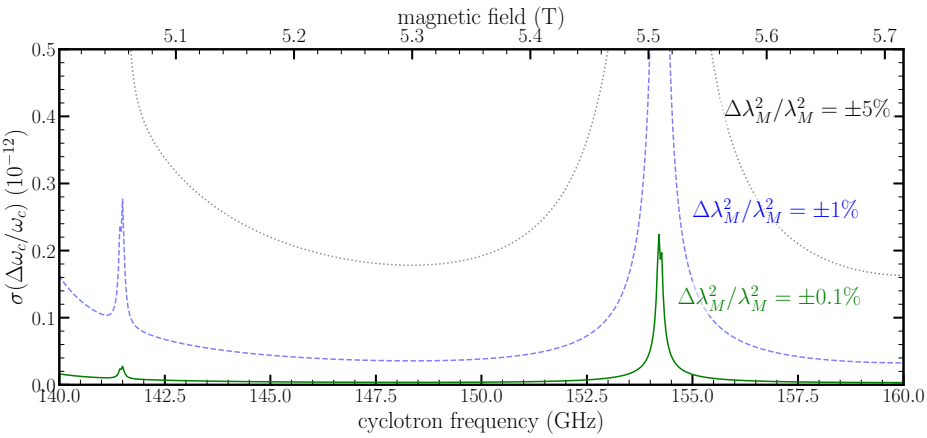

Figure 4.9: Dependence of uncertainty in cavity correction on the coupling strength. The uncertainty in the cavity correction scales linearly with the uncertainty in the coupling strength.

these assumptions. The coupling strength is a measure of the field locally at the position of the electron normalized to the field across the entire volume of the trap, Equation 4.15. Therefore, λ_M^2 scales like the inverse of the cavity size, that is $\lambda_M^2 \sim 1/(\text{volume})^1$.

Even though there are fewer modes contributing to the cavity shift in the new trap cavity, these modes have a larger relative contribution. Consequently, a similar relative uncertainty on the coupling strength implies a larger contribution to the uncertainty on the cavity correction for each mode. The net result is that even with the significantly reduced mode density the cavity shift and its uncertainty remains comparable to the 2023 measurement.

The only path forward is to reduce the reduce the uncertainty in the coupling strength. Figure 4.9 demonstrates how the cavity correction uncertainty would scale with reduced uncertainty on the λ_M^2. The reduction in the uncertainty of the cavity correction with λ_M^2 is linear, therefore a reduction by factor of 10 in the estimated uncertainty in λ_M^2 would mean a 10 times better measurement. Since the coupling strength cannot be directly probed *in-situ* then the challenge of reducing this uncertainty is the immediate challenge in pushing the precision of the g-factor measurement further.

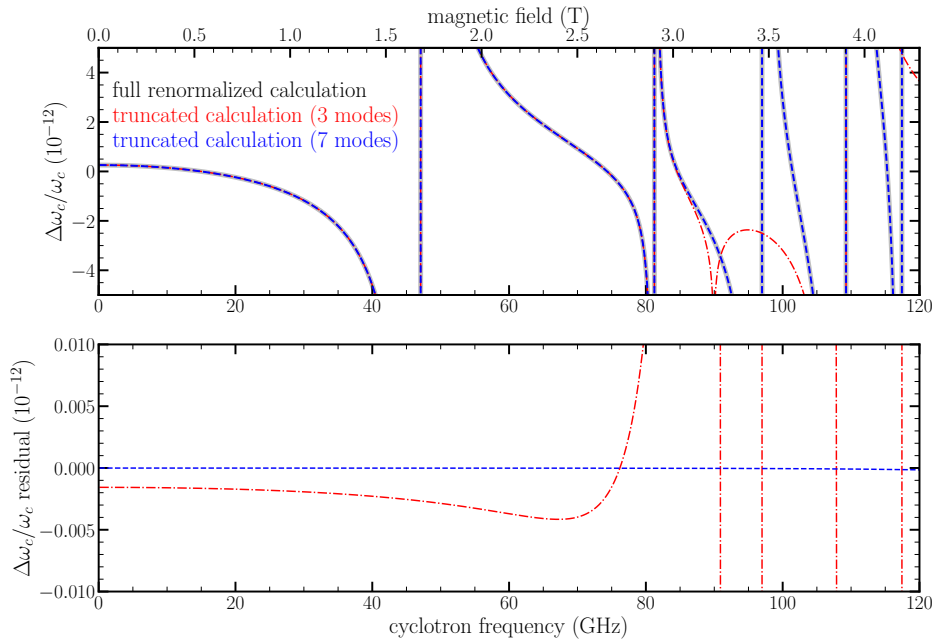

Figure 4.10: Cavity Correction with Truncated Sum. With only the first 3 modes included in the sum, the difference with the full calculation is $< 1 \times 10^{-14}$, while with the first 7 modes the difference is $< 1 \times 10^{-17}$.

4.3.1 Determining λ_M^2 in the New Trap

As outlined thus far, the major gain thus far with the new trap is the reduced mode density but at the cost of the increased coupling strength compared to the 2023 measurement trap-cavity. In this section we propose a procedure for reducing the coupling strength uncertainty in a future magnetic moment measurement.

Below the *cut-off* frequency of the trap cavity, that is, below the lowest resonant mode of the cavity, the cavity shift is dominated by the contribution of the lowest frequency mode. Figure 4.10 shows the calculated cavity shift as a function of the number of modes include in the re-normalized calculation below the cut-off frequency of the trap (47.1 GHz). Even with only the lowest three modes included, the correction to the cavity mode is already less than 1×10^{-14} in relative units different from the full re-normalized calculation. When the lowest 7 strongly coupled modes are included, the residual with the full re-normalized calculation

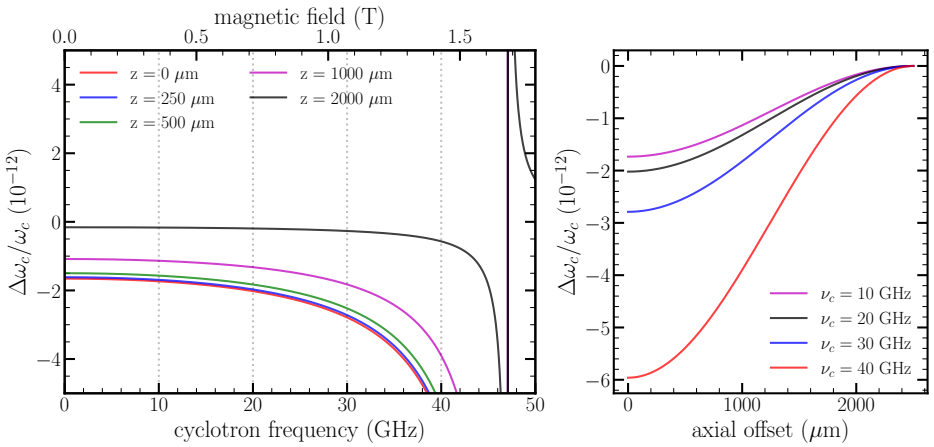

Figure 4.11: Lowest mode coupling vs. axial offset assuming the Lorentzian approximation from the lowest mode only.

is $< 1 \times 10^{-17}$ in relative units.

Therefore, in a future measurement of the g-factor below cut-off in this trap cavity, only the contribution to the cavity correction from the lowest several modes needs to be includes to determine the cavity shift at the projected precision of the experiment. This is precisely the advantage gained in moving to a smaller trap-cavity. In the previous trap-cavity where there were over 25 strongly coupled modes in the frequency range up to 150 GHz, in the new trap cavity there are only 7.

With the reduced mode density we expect to be able to more precisely determine the best fit parameters of the cavity z_0 and ρ_0 that more accurately represents the cavity properties of the trap. This should reduce the discrepancy of the measured mode frequencies from that determined from the best fit parameters Figure (4.4). Additionally, we can consider directly inferring λ_M^2 through measurement with a single electron. Since we do not know the exact mechanism that relates the measured parametrically driven response to the cavity properties and cyclotron damping, we cannot infer λ_M^2 from the parametric response. Additionally, even though we can measure the cyclotron damping rate with a single electron, using a single electron to determine λ_M^2 through lifetime measurements at the $< 1\%$ level would be

challenging since it would require precise determinations of the damping rate close to the cavity resonances where we observe enhanced spontaneous emission.

An complementary approach would be to directly determine the magnetic moment of the electron at different cyclotron frequencies below cut-off and with the axial position of the particle offset from the center. Figure 4.11 demonstrates how the measured cavity shifted cyclotron frequency, and hence the g-factor scales as the particle is axially offset. We plot the correction to the relative correction cyclotron frequency (and hence measured magnetic moment) as a function of cyclotron frequency and axial offset below the cut-off frequency of the trap. Note in this calculation we only include the single mode Lorentzian approximation (Equation 4.19) from the lowest mode of the cavity. We propose measurements of the magnetic moment at several cyclotron frequencies below cut-off and at different axial offsets. The measured magnetic moment can be fitted and extrapolated to the zero shift or free space magnetic moment. Further details on this proposal will follow in future work.

4.4 Summary

The most recent measurement of the magnet moment was equally limited by the cavity shift systematic effect and the cyclotron lineshape broadening. This chapter addressed the cavity shift systematic through first describing the work done in the determination of the cavity shift in the 2023 electron magnetic moment measurement and describing how this work informed the design of the trap cavity used in majority of the work presented in this thesis.

We have constructed and implemented a 5 times smaller trap-cavity by volume. This allows us to achieve a significantly reduced mode density compared to the trap-cavity used in the 2023 measurement. However, with this smaller trap-cavity, the coupling of the trap-cavity modes to the trapped particle is larger since the coupling strength of each mode scales

as the inverse of the volume of the trap cavity, that is $\lambda_M^2 \sim (\text{volume})^{-1}$.

The major challenge to higher precision measurements of the g-factor will be in accurately estimating the coupling strength between the trapped electron and the cavity mode. With our current tools this cannot be directly measured, however in the designed trap-cavity, with the reduced mode density we expect that we can more accurately estimate the coupling strength and achieve an improved measurement.

Chapter 5

Towards State Readout with Special Relativity

As discussed throughout this thesis, the most recent measurements of the electron magnetic moment were limited by two main systematic effects– the cyclotron lineshape broadening and cavity shift. Chapter 4 discusses the cavity shift systematic effect. Chapter 3 and this chapter discusses the reduction of the lineshape broadening through the elimination of the magnetic field inhomogeneity introduced for the quantum non-demolition coupling used for state readout. In future electron g-factor measurements, state readout will be performed through measuring the small axial frequency shift occurring due to the relativistic mass increase from the absorption of a single microwave photon exciting a cyclotron jump or spin flip. When a microwave photon is absorbed by the particle and excites its state from $n_c = 0 \rightarrow 1$, the increase in energy is equivalent to an increase in the relativistic mass of the electron from $m_e \rightarrow m_e + \hbar\omega_c/c^2$. This change results in an axial frequency shift of $(\delta\omega_z)_{\text{rel}} = -\frac{\hbar\omega_c}{2m_e c^2}\omega_z$.

The challenge of the relativistic detection scheme is that the axial frequency shift is about a factor of 10 smaller than axial frequency shifts used in previous experiments and therefore

needs an equivalent improvement in the axial frequency shift detection sensitivity is required. The improved apparatus developed in this work brings this long-standing goal within reach. The cyclotron linewidth parameter $\Delta\omega_c$ goes as,

$$\Delta\omega_c = \frac{eB_2}{m_e}\frac{k_B T_z}{m_e \omega_z^2}, \tag{5.1}$$

where B_2 is the size of the magnetic bottle, T_z is the axial temperature, ω_z is the axial frequency of the trapped electron. The two paths towards narrowing the the measured cyclotron lineshape involve reducing the axial temperature of the particle T_z and/or reducing the size of the magnetic bottle B_2. Chapter 3 addressed our effort towards implementing a SQUID amplifier that should reduce the axial temperature of the trapped electron from about 500 mK in the most recent g-factor experiments [6,40,75], to the *near*-quantum limited temperature of 10 mK.

This chapter deals with reducing the size of the magnetic bottle B_2 used for state-readout in the experiment. While all previous electron magnetic moment measurements have relied on state-readout with the magnetic bottle technique, also known as the continuous Stern-Gerlach effect, [116,117], a long-standing goal of the experiment is to eliminate the magnetic bottle entirely and instead rely on the axial frequency shift resulting from the relativistic mass shift from single cyclotron level change or spin flip [65, 118]. Not only will this reduce the measured cyclotron linewidth (equation 5.1) but may also reduce systematic broadening effects arising from axial and radial misalignments between the trapped electron in the Penning trap from the center of the magnetic bottle field described by Equation 5.2.

This chapter discusses our progress toward state-readout using the relativistic mass increase. We will first discuss the traditional magnetic bottle state readout scheme and its alternatives then we will outline principle of the relativistic detection, the requirements, and how the work described in this thesis brings us closer to relativistic state readout. Finally,

we will discuss the path forward.

5.1 State Readout with the Magnetic Bottle

As discussed in Chapter 2, g-factor measurement relies on the measurement of the ratio of two frequencies, the anomaly frequency ν_a and the cyclotron frequency ν_c. However, only the axial oscillation frequency of the particle is monitored. Therefore, changes to the spin and cyclotron state of the particle are read out as changes to the axial frequency of the particle through coupling these motions.

The coupling is accomplished through the introduction of a magnetic bottle, a pair of ferromagnetic rings (typically high purity nickel in the electron g-factor experiment), symmetrically about the center of the Penning trap. The magnetic bottle adds a magnetic field,

$$\vec{B}(z) = B_0\hat{z} + B_2\left(z^2 - \frac{\rho^2}{2}\right)\hat{z} - B_2 z\rho\hat{\rho} \tag{5.2}$$

onto the electrostatic field arising from the electrodes of the Penning trap. Here B_0 is a constant offset introduced by the bottle and B_2 is referred to as the size of the magnetic bottle.

Since the electron's total magnetic moment along the z-direction μ_z depends on the spin m_s and cyclotron states n_c,

$$\mu_z = -2\mu_B\left(\frac{1}{2} + n_c + \frac{g}{2}m_s\right) \tag{5.3}$$

then the total confining potential along the z-axis arising from the electrostatic potential

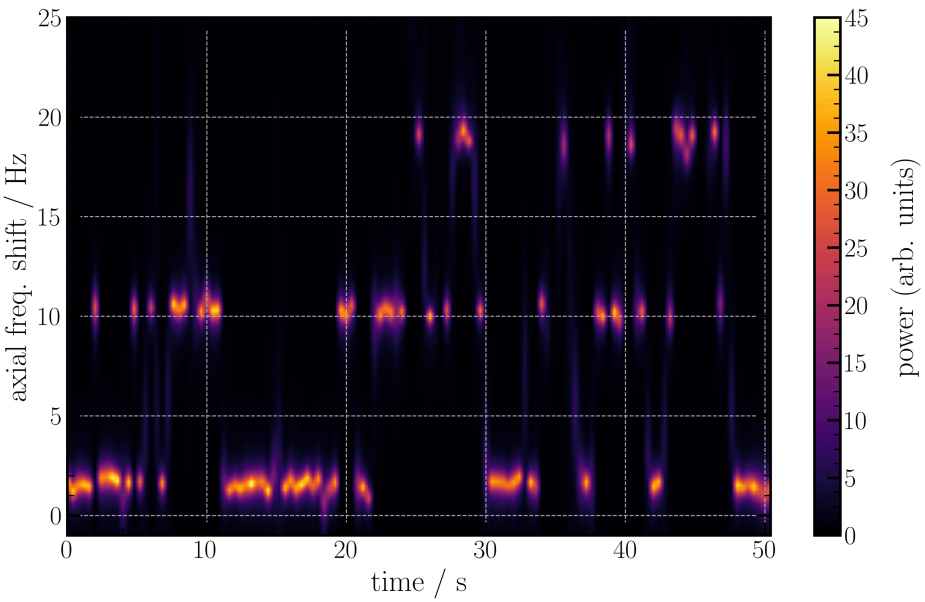

Figure 5.1: Quantum jumps in the commissioning run of the 2023 g-factor apparatus ($B_2 = 1500$ Tm^{-2} , $\nu_z = 114$ MHz).

and the magnetic bottle potential is,

$$\begin{aligned}\phi(z) &= \frac{1}{2}m\omega_z^2 z^2 + 2\mu_B B_2 z^2 \left(\frac{1}{2} + n_c + \frac{g}{2}m_s\right) \\ &\approx \frac{1}{2}m\left[\omega_z + \frac{2\mu_B B_2}{m\omega_z}\left(\frac{1}{2} + n_c + \frac{g}{2}m_s\right)\right]^2 z^2 \\ &= \frac{1}{2}m\left[\omega_z + \delta_c\left(\frac{1}{2} + n_c + \frac{g}{2}m_s\right)\right]^2 z^2,\end{aligned} \tag{5.4}$$

where we have defined the bottle shift term for one quantum jump δ_c as,

$$\delta_c \equiv \frac{2\mu_B B_2}{m_e\omega_z} = \frac{\hbar e B_2}{m_e^2\omega_z} \tag{5.5}$$

The shift in the axial frequency associated with a change in the cyclotron or spin state is,

$$\delta\omega_z = \delta_c\left(n_c + \frac{g}{2}m_s\right) \tag{5.6}$$

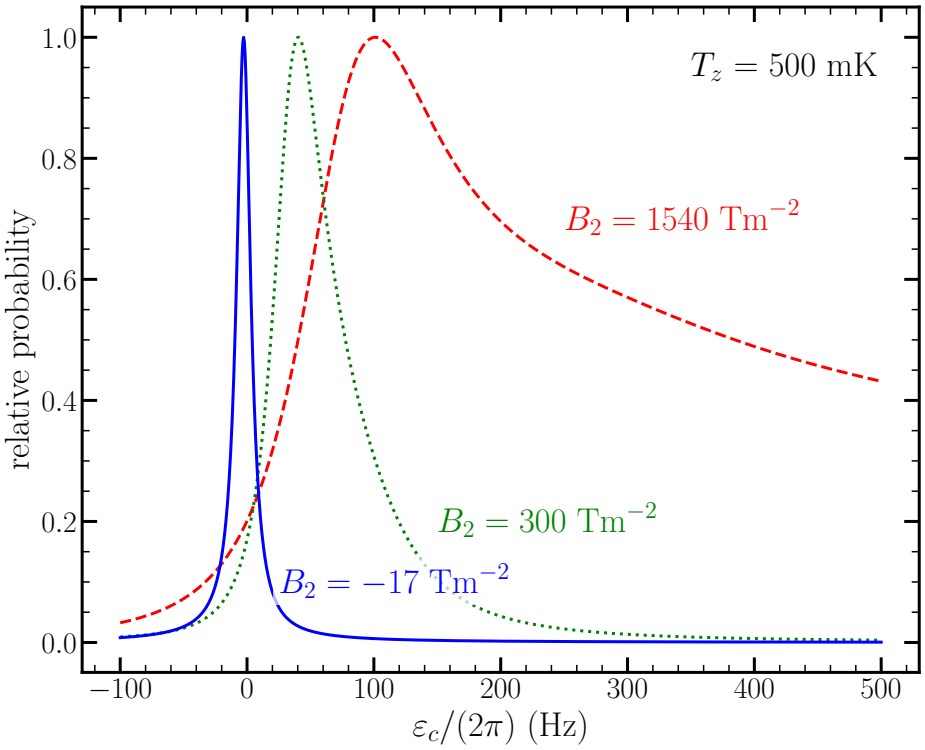

Figure 5.2: Dependence on the Cyclotron Lineshape on the magnetic bottle size at 500 mK.

Therefore, with the magnetic bottle superimposed on the Penning trap, change in the cyclotron or spin states are read out as changes in the axial frequency of the particle as shown in Figure 5.1. This demonstration of the non-destructive quantum state readout [60,62] is from the commissioning run of the 2023 g-factor experiment with $B_2 = 1500$ Tm^{-2}. The axial frequency of the particle is monitored as the cyclotron motion is excited with an on-resonance microwave cyclotron excitation drive.

While this elegant approach of coupling the axial motion to the cyclotron and spin motion to achieve state readout has enabled the electron g-factor measurement, it is now the limit in achieving narrower cyclotron linewidths. The thermal axial motion of the trapped particle, driven by detector backaction, in the inhomogenous magnetic bottle field described by Equation 5.2, gives rise to the cyclotron linewidth described by Equation 5.1. Figure 5.2 demonstrates how the measured lineshape depends on the size of the magnetic bottle at

500 mK. Therefore, reducing and ultimately eliminating the magnetic bottle broadening to the cyclotron linewidth is imperative for future electron g-factor measurements.

Before exploring the relativistic detection scheme, we will briefly discuss alternative approaches to the relativistic detection and highlight why these are not appropriate for our current experiment.

5.1.1 Alternative Approaches

The trade-off in reducing and eventually eliminating the magnetic bottle broadening is that the jump size and hence state detection sensitivity required scales as the size of the magnetic bottle, that is $\delta_c \propto B_2$, while the lineshape width scales also scales as the bottle width, $\Delta\omega_{c,a} \propto B_2 T_z/\omega_z^2$. While the smallest bottle size is favored for narrower detection, it comes at the expense of the size of the bottle shift. Therefore a reduced bottle size requires improved axial frequency shift detection sensitivity. This tradeoff is a longstanding problem in the electron magnetic moment measurement and other high precision magnetic moment measurements, for example, the proton/antiproton measurement. Several alternative direction to circumventing the bottle broadening have been proposed and explored. We will briefly summarize these approaches and their specific challenges as it relates to the electron magnetic moment experiment.

Variable Magnetic Bottle

The variable or switchable magnetic bottle [119] is a scheme proposed and demonstrated where a $B_2 z^2$ field is switched on through running a current through a superconducting wire placed symmetrically with the axis of the Penning trap. A current is run through the superconducting loop to produce the magnetic bottle field during state readout then switched off during the spectroscopy phase of the measurement.

While simple, implementing the scheme presents two challenges:

1. inducing a magnetic bottle field of order what has been used in electron magnetic moment experiments ($B_2 \sim 100$ Tm^{-2}) would require ~ 6 A of current for a superconducting loop the size of a typical ring electrode. This was impractical in the liquid helium systems of the past and even more impractical in the dilution refrigerator systems used today.

2. A single loop on its own would introduce both a zeroth order contribution, B_0, and higher order even terms $B_4,\ B_6, \cdots$. The residual B_0 contribution even when the variable bottle is switched *off*, if not controlled, can change between measurement cycles leading to the broadening of the measured cyclotron line.

Also, the limited cooling power of the dilution refrigerators used in the electron g-factor experiments today, 500 μW at 100 mK, make the implementation of the variable bottle scheme impossible. One can imagine using a superconducting flux transformer with an external winding placed outside of the magnet dewar itself; however, the current required for such a scheme would be impractical.

Multiple Penning trap technique

A multi-Penning trap technique is employed in the proton/anti-proton magnetic moment measurement. Since the proton magnetic moment scales as the much smaller nuclear magnetic moment, $\mu_N/\mu_B = m_e/m_B \approx 1/2000$, the magnetic bottle required for state-readout is several thousand times larger and the bottle broadening effect is more severe [120, 121].

The proton/antiproton experiments employ a multi-trap technique to circumvent the bottle broadening. The apparatus consists of several traps including one for precision spectroscopy where there is no magnetic bottle, $B_2 \approx 0$ Tm^{-2}, and one for state-readout where

the magnetic bottle is deliberately very large, $B_2 \approx 3 \times 10^5$ Tm^{-2} [122]. A trapped proton/antiproton is shuttled between the spectroscopy trap to the measurement trap throughout the measurement process.

This approach is not appropriate for the electron magnetic moment. At the precision at which the electron magnetic moment is measured, the microwave cavity coupling between the cyclotron motion of the particle and the Penning trap cavity modes shifts the measured g-factor from the free space value, see Chapter 4. This necessitates the deliberate choice of a closed endcap Penning trap [59] where the cavity shift is calculable as opposed to the open endcap cylindrical trap [88] used in the proton/antiproton experiments. Additionally, the inhibited spontaneous emission enabled by the closed endcap trap [70] enables sufficiently long lifetimes for us to achieve the quantum cyclotron [60, 62].

The multi-trap technique is possible through lossless shuttling of ions between open-endcap Penning traps [88]. For the closed endcap Penning traps [59] with minuscule access holes used in this experiment, lossless shuttling between traps has not been demonstrated. Therefore the multi-trap technique is not suitable for our current experiments.

Quantum Logic Spectroscopy

A dual trap method using quantum logic spectroscopy (QLS) mediated by a wire has recently been proposed for electrons [123]. The proposal describes a spectroscopy trap optimized for quantum jump spectroscopy and a logic trap with a large bottle and enhanced harmonicity for optimized for fast state readout. Separate electrons are confined in each trap and their axial motions are coupled via a wire. Through entanglement of the axial motions of the two trapped electrons, cyclotron transitions in the spectroscopy trap can be read out in the optimized logic trap.

While promising, this scheme requires ground state cooling of the axial state, multi-electron multi-trap entanglement, and the realization of low power dissipation cryogenic RF

switches before implementation. The development of these techniques are beyond the scope of this thesis work but the demonstration of single electron detection with a SQUID amplifier which should enable significantly lower axial temperatures is a tool that can be used in this future scheme.

5.2 Principle of Relativistic Detection

The goal in this detection scheme is to detect single quantum cyclotron transitions or spin flips through the relativistic mass increase associated with that transition [65]. The detection of many cyclotron transitions has been observed before [118,124]. The energy shift associated with a single cyclotron transition is $\hbar\omega_c$ and the mass-energy equivalence principle dictates that this increase in internal energy is equivalent to an increase in the effective mass of the electron, that is $m_e \rightarrow m_e + \hbar\omega_c/c^2$.

The classical axial oscillation frequency of the trapped electron is,

$$\omega_z = \sqrt{\frac{eV_R}{m_e d^2}\,(1 + C_2)} = \alpha \times \frac{1}{\sqrt{m_e}}, \tag{5.7}$$

Therefore, the axial frequency shift that occurs due to the relativistic mass increase when a single cyclotron photon $\hbar\omega_c$ is absorbed is,

$$\frac{(\delta\omega_z)_{\mathrm{rel}}}{\omega_z} = -\frac{\hbar\omega_c}{2m_e c^2}. \tag{5.8}$$

We can express this axial frequency shift as an equivalent magnetic bottle as,

$$B_{2;\mathrm{rel}} = -\frac{m_e\omega_z^2\omega_c}{2ec^2}, \tag{5.9}$$

In our system, with the magnetic field set to 5.5 T, $\omega_z/(2\pi) = 120$ MHz, and $\omega_c = 154$

experiment	B_2 (T/m^2)	ν_z (MHz)	T_z (K)	$\delta\omega_z$ (Hz)	$\Delta\omega_c$ (Hz)
UW 1987 [58, 125]	150	60	4.2	1.3	1880
Harvard 2008 [40]	1540	200	1.1 - 0.23	4	200
NU 2023 [6]	300	114	0.5	1.3	124
ATRAP 2013 [126]	2.9×10^5	0.920	8.5	0.119 [1]	–

Table 5.1: Summary of bottle shifts from previous experiments. We include the ATRAP experiments with a single antiproton for reference. [1] the spin flip is measured in these experiments instead of the cyclotron shift.

GHz, $(\delta\omega_z)_{\rm rel} = -0.08$ Hz and $B_{2;\rm rel} = -17$ Tm^{-2}. We note, as discussed in Chapter 3, we have observed increased instability in our SQUID amplifier at larger magnetic fields and, therefore, have performed most of the SQUID detection demonstrations at a reduced field of 0.75 T. At this field, $(\delta\omega_z)_{\rm rel}/(2\pi) = -0.01$ Hz and $B_{2;\rm rel} = -2.4$ Tm^{-2}. The rest of the chapter assumes the design goal of detection at 5.5 T.

The 2023 g-factor measurement utilized a magnetic bottle size of $B_2 = 300$ Tm^{-2} which gave a axial frequency shift $\delta\omega_z/(2\pi) = 1.3$ Hz. The minimum resolvable axial frequency shift in this apparatus through a driven axial detection scheme was less than 0.1 Hz with over a minute averaging time (Chapter 5, [42]). Table 5.1 gives a concise summary of magnetic bottle sizes and bottle jump shifts used in previous experiments.

While the relativistic shift was only marginally resolvable in the 2023 apparatus after extensive averaging, the present system was designed and built to achieve superior frequency resolution more rapidly due to two key advances:

1. **Lower detector noise temperature from the SQUID amplifier**. We have demonstrated single electron detection with a SQUID amplifier (Chapter 3). The dilution refrigerator reaches temperatures below 10 mK. The coupling of the axial motion to the detection circuit is characterized by the single particle damping rate γ_z while the detector noise floor is set by its noise temperature T_N, resulting in noise power density of $k_B T_N$ per Hz. Consequently, the driven signal SNR scales like $SNR \propto \gamma_z/T_N$ plus

the bath temperature T_0. In the demonstrated system γ_z is increased by a factor of 4 relative to 2023 and we expect temperature will be reduced by a factor of 25, due to the *near*-quantum limited SQUID amplifier. Therefore, we expect a ~ 100 improvement in the driven-signal SNR.

2. **A more harmonic trap for larger driven signals.** We have designed and implemented a trap with improved harmonicity (Chapter 2). With this new trap we expect a factor of 20 reduction in the dominant contribution to the anharmonicity compared to the 2023 experiment and hence expect to reduce the amplitude dependent axial frequency. With this new trap we can then drive the particle to much larger amplitudes without paying the penalty of axial frequency broadening.

With these two critical improvements we expect achieve a greatly improved SNR compared to the previous experiment and be able to resolve the relativistic shift with less averaging. The next section discusses a demonstration of the improved dip detection. However, as we will see, for future g-factor measurement, driven responses are essential. We will discuss the challenges that prevented us from achieving this in this current iteration of the experiment and how we plan to overcome these challenges.

5.3 Demonstrated improvement in SNR with Single Electron Dips

While we have not yet demonstrated improved driven signals with a single electron due to SQUID saturation, we have demonstrated improved dip detection with a single electron (Figure 5.3). The SNR demonstrated in these dip measurements are at more than a factor of 2 improved on the best dip measurements in the apparatus used for the 2023 measurement of the electron magnetic moment, even with 5 times less averaging. With the SNR demonstrated

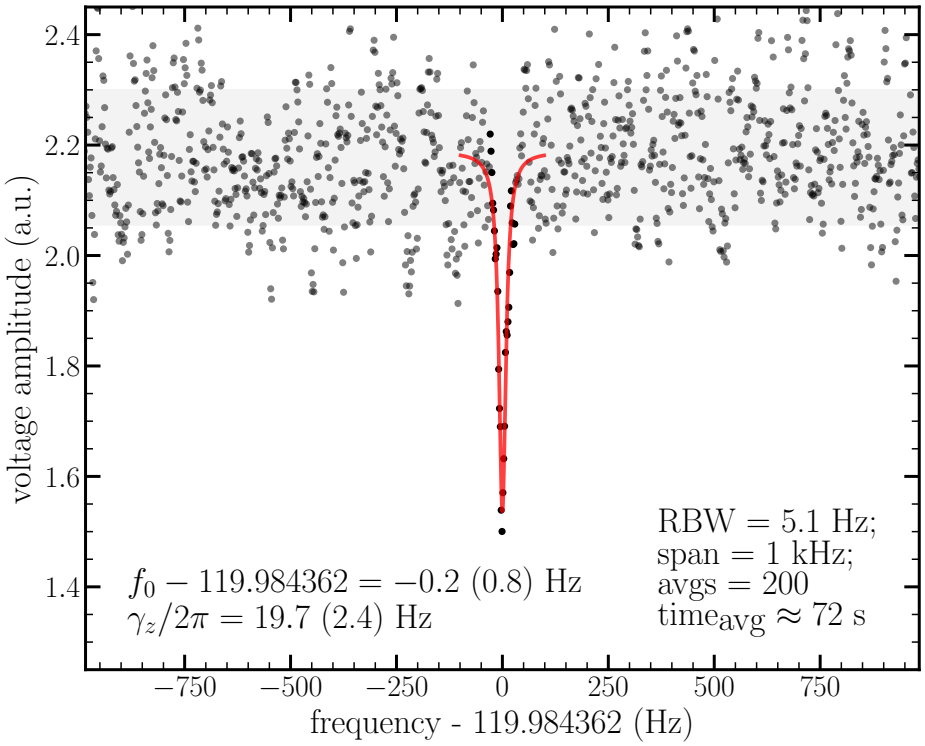

Figure 5.3: Single electron dip detected with the SQUID amplifier in the new trap. A dip SNR defined as dip depth divided by standard deviation of the background noise (shown by the gray band) of 7 is achieved after only 72 s of averaging.

in the shown dip measurement the minimum resolvable axial frequency shift is ~ 1.4 Hz.

Since SNR scales a $1/\sqrt{N}$, we estimate that with ten times more acquisition time, about 10 minutes, the minimum resolvable shift of around 0.4 Hz at the same resolution bandwidth. Averaging longer until we can resolve the relativistic shift with dips is possible; however, with this long timescale of averaging the minimum resolvable frequency will be limited by other causes of axial frequency fluctuation, for example, voltage drifts due to temperature fluctuations of the power supply, pressure fluctuations in the dewar, etc. Additionally, such a slow readout scheme would be undesirable for a electron g-factor measurement as it would require us to make measurements of the spin flip and anomaly frequency and the total measurement timescale would grow significantly.

Therefore, although it is possible to measure the relativistic frequency shift through dip

measurements and long averaging, it is undesirable since the measurement timescale would be significantly extended. Additionally, these dip measurements were taken at 200 mK. As we reduce the temperature of the system in future measurements the SNR of the dip will reduce as the square root of the temperature. Therefore, at 10 mK we can expect at best a reduction in SNR by a factor of 4.5, making this scheme extremely difficult. Going forward, the best scheme is a driven scheme as it enhances the SNR as we will discuss in the next section.

5.4 Current Limitations and Next Steps

5.4.1 Mixed drive scheme with direct feedthrough cancellation

We propose using a mixed drive scheme to detect the relativistic shift. The particle can be driven with two drives $\nu_{\text{drive}} - \nu_{\text{mod}}$ and ν_{mod}, where ν_{drive} is the main drive frequency and ν_{mod} is a modulation frequency as shown in Figure 5.5 (a). The electron will mix these two drives and respond at ν_{drive} [68]. An example of the in-phase and quadrature response of this drive scheme as ν_d is swept across the axial frequency of the particle ν_z is shown in Figure 5.4. This data was taken with a single electron detected with a transistor amplifier in the apparatus used for the 2023 g-factor measurement [42].

We propose driving the particle with $\nu_{\text{drive}} - \nu_{\text{mod}} = \nu_z - \nu_{\text{mod}}$ and ν_{mod}, where ν_z is the axial frequency of the particle. By continuously monitoring the quadrature response to the drive we can detect small changes in the axial frequency of the particle as a large shift in the measured quadrature response.

While we did try this scheme in with the SQUID amplifier, we were not able to measure the expected damped driven harmonic oscillator response as seen in Figure 5.4. The mixed drive scheme relies on the particle mixing the two drives and responding at their sum. It

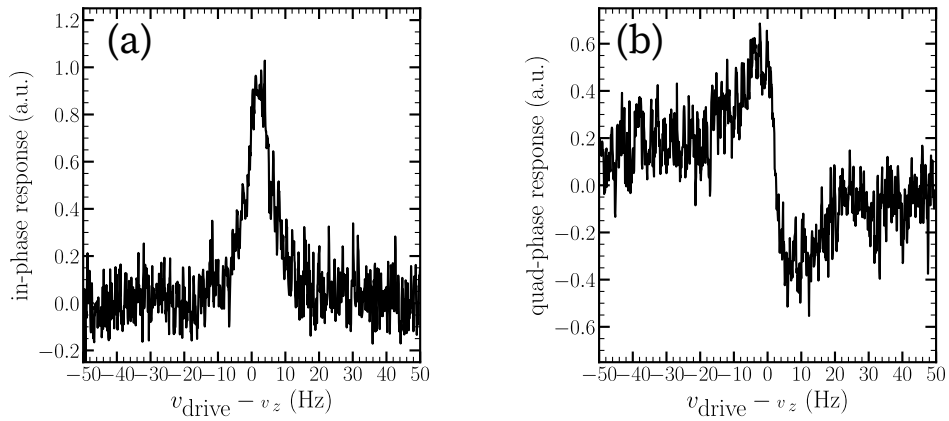

Figure 5.4: Driven in-phase (a) and quadrature response (b) of a single electron oscillator. Detected with an FET amplifier.

relies on the non-linearity of the single electron oscillator in an imperfect harmonic potential. At the same time, the SQUID amplifier is an extremely non-linear device capable of strongly mixing the drives. We suspect that this strong mixing from the SQUID amplifier to be the reason for us not observing the expected response. Additionally, although the SQUID is configured as an extremely sensitive RF amplifier, its dynamic range is very small and it saturates with a drive strength ~ 100 dBm. The direct feedthrough from the mixed drive is sufficient to saturae the SQUID.

To circumvent this challenge we propose directly driving at the input of the SQUID with a phase and amplitude adjusted drive signal $\nu_{\rm drive} - \nu_{\rm mod}$ to cancel the direct feedthrough of $\nu_{\rm drive} - \nu_{\rm mod}$ that the SQUID amplifier currently sees. This should allow us to only measure the mixed drive response from the particle while canceling any direct feedthrough and mixing done by the SQUID amplifier.

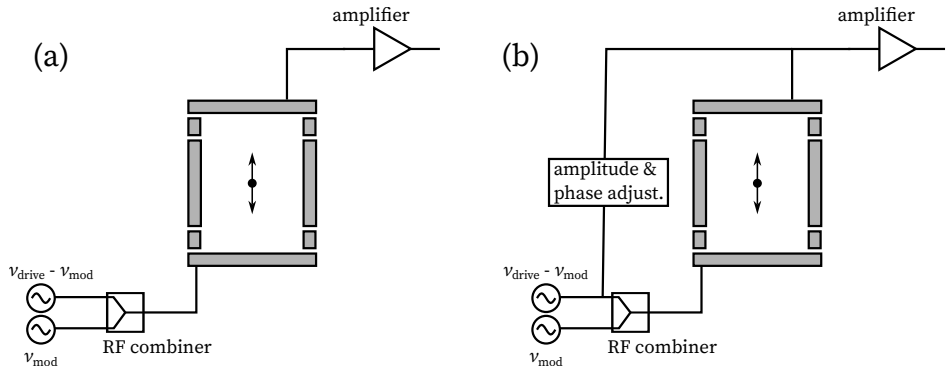

Figure 5.5: Mixed drive scheme typically used (a) and Mixed drive with direct feedthrough compensation (b)

5.4.2 Temporary use of a the Magnetic Bottle for Low Temperature Characterization

We have demonstrated single electron detection with the SQUID amplifier but we are still to quantify the reduction of the axial temperature of the particle. While we expect the particle's axial temperature to ultimately be limited by the dilution refrigerator temperature of 10 mK, many sources of noise, for example insufficiently attenuated RF drive lines, detector back-action from warmer stages, SQUID bias voltage noise, etc., can raise the noise temperature of the amplifier and the effective axial temperature of the particle. The axial temperature of the particle must be carefully characterized going forward.

The simplest method for precisely determining the axial temperature of the particle is through measuring and fitting the cyclotron lineshape to extract the temperature. We propose introducing a relatively large magnetic bottle $B_2 = 300$ Tm^{-2}, such that the axial frequency shift with a cyclotron jump is $\delta\omega_z/2\pi = 1.3$ Hz is easily resolvable. This axial frequency shift was easily resolved in the 2023 measurement [6, 42] and should be easily resolvable in our current apparatus. The cyclotron lineshape can then be measured at different fixed bath temperatures to determine the lowest achievable axial temperature of the particle.

We note that even with this larger bottle, the expected cyclotron linewidth would still be narrower by a factor 25 than the measured lineshape in the 2023 measurement if $T_z = 10$ mK is demonstrated. Once the temperature of the particle is carefully characterized and the axial frequency detection is optimized then the next step would be to remove the magnetic bottle completely.

5.5 Summary

We have presented the motivation and mechanism for quantum state-readout in the electron magnetic moment experiment with special relativity. The removal of the magnetic bottle from future state-readout schemes is expected to reduce the cyclotron lineshape by a factor of 6 compared to the 2023 measurement, though it introduces the need for enhanced axial frequency discrimination.

To address this, we have developed a system that should achieve improved axial frequency resolution by reducing the axial temperature of the trapped particle through the use of the SQUID amplifier and by implementing a more harmonic Penning trap that allows larger driven axial oscillation amplitudes with minimal frequency broadening. With the upgraded SQUID-based detection chain, we demonstrated a substantial improvement in the single electron-dip detection. Nevertheless, while it is possible to discriminate the axial frequency shift sufficiently for relativistic detection through extended averaging, we argue that this scheme is not optimal for future g-factor measurements.

Looking ahead, we propose the reintroduction of the magnetic bottle to enable precise characterization of the particle's axial temperature, together with the implementation of a compensated mixed-drive detection scheme for fast and efficient readout of the relativistic axial frequency shift. This paves the way for a future electron magnetic moment measurement with relativistic state-readout

Chapter 6

Conclusion

This thesis, describes the construction and commissioning of an entirely new apparatus and the development of new techniques that will enable higher-precision measurement of the electron and positron magnetic moments. Chapter 1 outlines the theoretical motivation for improving these measurements, discusses uncertainties for the most recent determination of the electron magnetic moment [6, 42], and presents strategies to surpass these.

Chapter 2 details the principles of the measurement and the design of the new apparatus. The system includes a dilution refrigerator that reaches temperatures below 10 mK, an exceptionally harmonic Penning trap with an optimized microwave cavity for both unprecedented detection sensitivity and cavity-shift control, a positron accumulation trap for a future positron measurement, and superb vibration isolation of the experimental platform.

Chapter 3, describes the implementation of a SQUID detector. This effort required the design and commissioning of a reduced-fringe-field superconducting solenoid, superconducting shields, and careful impedance matching across cascaded SQUID stages. With this new detection scheme we have demonstrated the detection of a single electron with the highest signal-to-noise ratio observed. It should now be possible to demonstrate a 25-fold reduction in the electron axial temperature over all previous measurements. The SQUID now operates

stably at lower magnetic fields and modest temperatures ($B \leq 0.75$ T, T ≥ 200 mK), but the proposed superconducting shield design and flux-correction outlined in Chapter 3 should to mitigate the gain instability observed at lower temperatures and higher fields.

Chapter 4 reviews the cavity-shift correction applied in the 2023 g-factor measurement and how this informed the design of the new trap-cavity system. The trap is five times smaller in volume, substantially reducing the cavity-mode density to enable the reduction of the cavity-shift uncertainty.

Finally, Chapter 5 describes how our progress brings detecting the relativistic mass increase associated with a single cyclotron transition or spin flip, a long standing goal of our experimental program [65], within reach. We have demonstrated markedly improved non-driven single electron sensitivity with the new apparatus, establishing the foundation for relativistic state readout when driven-signal detection sensitivity is employed.

The tools and methods developed in this thesis bring the experiment substantially closer to achieving quantum-limited detection sensitivity, ultimately enabling state detection without a magnetic gradient, narrowing the cyclotron lineshape by an order of magnitude or more. The cavity shift will be reduced using the new trap-cavity design.

These tools bring us much closer to a ten-times improved measurements of the electron and positron magnetic moments. Together, these two measurements will provide the most stringent test of CPT invariance with leptons to date and provide the most sensitive test of the Standard Model of particle physics.

Bibliography

[1] P. A. M. Dirac, Proc. R. Soc. Ser. A **117**, 610 (1928).

[2] P. Kusch and H. M. Foley, Phys. Rev. **72**, 1256 (1947).

[3] J. Schwinger, Phys. Rev. **73**, 416 (1948).

[4] R. P. Feynman, Rev. Mod. Phys. **20**, 367 (1948).

[5] S. Tomonaga, Prog. Theor. Phys. **1**, 27 (1946).

[6] X. Fan, T. Myers, B. Sukra, and G. Gabrielse, Physical Review Letters **130**, 071801 (2023).

[7] V. C. Rubin and W. K. Ford Jr, Astrophysical Journal, vol. 159, p. 379 **159**, 379 (1970).

[8] N. Aghanim *et al.*, Astron. Astrophys **641**, A6 (2020).

[9] Y. Fukuda *et al.*, Physical Review Letters **81**, 1562 (1998).

[10] Q. R. Ahmad *et al.*, Physical Review Letters **89**, 011301 (2002).

[11] A. G. Riess *et al.*, The astronomical journal **116**, 1009 (1998).

[12] S. Perlmutter *et al.*, The Astrophysical Journal **517**, 565 (1999).

[13] A. D. Sakharov, *In The Intermissions Collected Works on Research into the Essentials of Theoretical Physics in Russian Federal Nuclear Center, Arzamas-16* (World Scientific, ADDRESS, 1998), pp. 84–87.

[14] L. Canetti, M. Drewes, and M. Shaposhnikov, New Journal of Physics **14**, 095012 (2012).

[15] T. Aoyama, T. Kinoshita, and M. Nio, Atoms **7**, (2019).

[16] P. J. Mohr, D. B. Newell, B. N. Taylor, and E. Tiesinga, Rev. Mod. Phys. **97**, 025002 (2025).

[17] J. Schwinger, Phys. Rev. **73**, 416 (1948).

[18] C. M. Sommerfield, Ann. Phys. (N.Y.) **5**, 26 (1958).

[19] A. Petermann, Nucl. Phys. **5**, 677 (1958).

[20] S. Laporta and E. Remiddi, Phys. Lett. B **379**, 283 (1996).

[21] S. Laporta, Physics Letters B **772**, 232 (2017).

[22] T. Aoyama, M. Hayakawa, T. Kinoshita, and M. Nio, Phys. Rev. D **91**, 033006 (2015).

[23] S. Volkov, Phys. Rev. D **110**, 036001 (2024).

[24] T. Aoyama, M. Hayakawa, A. Hirayama, and M. Nio, Phys. Rev. D **111**, L031902 (2025).

[25] S. Volkov, Phys. Rev. D **100**, 096004 (2019).

[26] H. Elend, Physics Letters **20**, 682 (1966).

[27] M. A. Samuel and G. Li, Phys. Rev. D **44**, 3935 (1991).

[28] G. Li, R. Mendel, and M. A. Samuel, Phys. Rev. D **47**, 1723 (1993).

[29] S. Laporta and E. Remiddi, Phys. Lett. B **301**, 440 (1993).

[30] S. Laporta, Il Nuovo Cimento A (1965-1970) **106**, 675 (1993).

[31] P. M. A. Kurz, T. Liu and M. Steinhauser, Nucl. Phys. B **879**, 1 (2014).

[32] T. Aoyama, M. Hayakawa, Kinoshita, and M. Nio, Phys. Rev. D **85**, 033007 (2012).

[33] Jegerlehner, Fred, EPJ Web Conf. **218**, 01003 (2019).

[34] A. Beyer *et al.*, Science **358**, 79 (2017).

[35] S. Sturm, F. Köhler, J. Zatorski, A. Wagner, Z. Harman, G. Werth, W. Quint, C. H. Keitel, and K. Blaum, Nature **506**, 467 (2014).

[36] F. Khler, S. Sturm, A. Kracke, G. Werth, W. Quint, and K. Blaum, Journal of Physics B: Atomic, Molecular and Optical Physics **48**, 144032 (2015).

[37] B. J. Mount, M. Redshaw, and E. G. Myers, Phys. Rev. A **82**, 042513 (2010).

[38] L. Morel, Z. Yao, P. Cladé, and S. Guellati-Khélifa, Nature **588**, 61 (2020).

[39] R. H. Parker, C. Yu, W. Zhong, B. Estey, and H. Müller, Science **360**, 191 (2018).

[40] D. Hanneke, S. Fogwell, and G. Gabrielse, Phys. Rev. Lett. **100**, 120801 (2008).

[41] D. Hanneke, Ph.D. thesis, Harvard University, 2007, (thesis advisor: G. Gabriesle).

[42] X. Fan, Ph.D. thesis, Harvard University, 2022, (thesis advisor: G. Gabriesle).

[43] MITP Topical Workshop: Precision Determinations of the Fine-Structure Constant (2025), `https://indico.mitp.uni-mainz.de/event/417/`, 2025, mainz, DE, October 2731, 2025.

[44] Z. Pagel, Ph.D. thesis, University of California, Berkeley, 2023, (thesis advisor: H. Mueller).

[45] J. S. Schelfhout, T. M. Hird, K. M. Hughes, and C. J. Foot, Phys. Rev. A **110**, 053309 (2024).

[46] M. Wang, G. Audi, F. G. Kondev, W. Huang, S. Naimi, and X. Xu, Chinese Physics C **41**, 030003 (2017).

[47] M. Pospelov, Phys. Rev. D **80**, 095002 (2009).

[48] S.-F. Ge, X.-D. Ma, and P. Pasquini, The European Physical Journal C **81**, 787 (2021).

[49] D. P. Aguillard *et al.*, Phys. Rev. Lett. **135**, 101802 (2025).

[50] R. Aliberti *et al.*, Physics Reports **1143**, 1 (2025).

[51] J. Batley *et al.*, Physics Letters B **746**, 178 (2015).

[52] J. P. Lees *et al.*, Phys. Rev. Lett. **119**, 131804 (2017).

[53] P. Ilten, Y. Soreq, J. Thaler, M. Williams, and W. Xue, Phys. Rev. Lett. **116**, 251803 (2016).

[54] R. Aaij *et al.*, Phys. Rev. Lett. **124**, 041801 (2020).

[55] A. M. Sirunyan *et al.*, Phys. Rev. Lett. **124**, 131802 (2020).

[56] L. K. Gibbons *et al.*, Phys. Rev. D **55**, 6625 (1997).

[57] S. Navas *et al.*, Phys. Rev. D **110**, 030001 (2024).

[58] R. S. Van Dyck, Jr., P. B. Schwinberg, and H. G. Dehmelt, Phys. Rev. Lett. **59**, 26 (1987).

[59] G. Gabrielse and F. C. MacKintosh, Intl. J. of Mass Spec. and Ion Proc. **57**, 1 (1984).

[60] S. Peil and G. Gabrielse, Phys. Rev. Lett. **83**, 1287 (1999).

[61] B. D'Urso, Ph.D. thesis, Harvard University, 2003, (thesis advisor: G. Gabrielse).

[62] S. Peil, Ph.D. thesis, Harvard University, 1999.

[63] L. S. Brown, G. Gabrielse, K. Helmerson, and J. N. Tan, Phys. Rev. A **32**, 3204 (1985).

[64] L. S. Brown, G. Gabrielse, K. Helmerson, and J. Tan, Phys. Rev. Lett. **55**, 44 (1985).

[65] G. Gabrielse and H. Dehmelt, National Bureau of Standards, Special Publication 219 (1984).

[66] G. Gabrielse and G. Venanzoni, Measured Lepton Magnetic Moments, 2025.

[67] B. Lautrup and H. Zinkernagel, Studies in History and Philosophy of Science Part B: Studies in History and Philosophy of Modern Physics **30**, 85 (1999).

[68] L. S. Brown and G. Gabrielse, Rev. Mod. Phys. **58**, 233 (1986).

[69] H. Dehmelt, in *Radiofrequency Spectroscopy of Stored Ions I: Storage**Part II: Spectroscopy is now scheduled to appear in Volume V of this series.*, Vol. 3 of *Advances in Atomic and Molecular Physics*, edited by D. Bates and I. Estermann (Academic Press, ADDRESS, 1968), pp. 53–72.

[70] G. Gabrielse and H. Dehmelt, Phys. Rev. Lett. **55**, 67 (1985).

[71] R. H. Koch, D. J. Van Harlingen, and J. Clarke, Applied Physics Letters **38**, 380 (1981).

[72] F. C. Wellstood, C. Urbina, and J. Clarke, Phys. Rev. B **49**, 5942 (1994).

[73] M. Mck, J. B. Kycia, and J. Clarke, Applied Physics Letters **78**, 967 (2001).

[74] L. S. Brown and G. Gabrielse, Phys. Rev. A **25**, 2423 (1982).

[75] B. Odom, D. Hanneke, B. D'Urso, and G. Gabrielse, Phys. Rev. Lett. **97**, 030801 (2006).

[76] B. Odom, Ph.D. thesis, Harvard University, 2004, (thesis advisor: G. Gabrielse).

[77] S. Sturm *et al.*, The European Physical Journal Special Topics **227**, 1425 (2019).

[78] A. Weigel, Ph.D. thesis, Ruprecht-Karls-Universität, Heidelberg, 2019.

[79] W. W. Maxalpine and R. O. Schildknecht, Proceedings of the IRE **xxx**, 2099 (1959).

[80] W. W. Macalpine and R. O. Schildknecht, Proc. IRE **47**, 2099 (1959).

[81] L. S. Brown, K. Helmerson, and J. Tan, Phys. Rev. A **34**, 2638 (1986).

[82] L. S. Brown, K. Helmerson, and J. Tan, Phys. Rev. A **34**, 2638 (1986).

[83] J. D. Jackson, *Classical Electrodynamics*, 3rd ed. (John Wiley & Sons, New York, 1999).

[84] P. J. Schultz and K. G. Lynn, Rev. Mod. Phys. **60**, 701 (1988).

[85] J. Estrada, T. Roach, J. N. Tan, P. Yesley, and G. Gabrielse, Phys. Rev. Lett. **84**, 859 (2000).

[86] J. Estrata, Ph.D. thesis, Harvard University, 2003, (thesis advisor: G. Gabrielse).

[87] S. F. Hoogerheide, Ph.D. thesis, Harvard University, 2013.

[88] G. Gabrielse, L. Haarsma, and S. L. Rolston, Intl. J. of Mass Spec. and Ion Proc. **88**, 319 (1989), ibid. 93:, 121 (1989).

[89] G. Gabrielse, X. Fei, L. A. Orozco, R. L. Tjoelker, J. Haas, H. Kalinowsky, T. A. Trainor, and W. Kells, Phys. Rev. Lett. **65**, 1317 (1990).

[90] S. Sellner *et al.*, New Journal of Physics **19**, 083023 (2017).

[91] J. W. Britton, J. G. Bohnet, B. C. Sawyer, H. Uys, M. J. Biercuk, and J. J. Bollinger, Phys. Rev. A **93**, 062511 (2016).

[92] L. S. Brown, Phys. Rev. Lett. **52**, 2013 (1984).

[93] X. Fan and G. Gabrielse, Phys. Rev. A **103**, 022824 (2021).

[94] X. Fan and G. Gabrielse, Phys. Rev. Lett. **126**, 070402 (2021).

[95] F. London, *Superfluids* (Wiley, New York, 1950).

[96] B. S. Deaver and W. M. Fairbank, Phys. Rev. Lett. **7**, 43 (1961).

[97] I. Giaever, Phys. Rev. Lett. **5**, 147 (1960).

[98] B. Josephson, Physics Letters **1**, 251 (1962).

[99] J. Clarke and A. Braginski, *The SQUID Handbook: Fundamentals and Technology of SQUIDs and SQUID Systems* (Wiley, Weinheim, Germany, 2006).

[100] C. Hilbert and J. Clarke, Journal of Low Temperature Physics **61**, 263 (1985).

[101] M. Mck, M.-O. Andr, J. Clarke, J. Gail, and C. Heiden, Applied Physics Letters **72**, 2885 (1998).

[102] M. Mück, J. B. Kycia, and J. Clarke, Applied Physics Letters **78**, 967 (2001).

[103] M. P. DeFeo and B. L. T. Plourde, Applied Physics Letters **101**, 052603 (2012).

[104] M. Mck and J. Clarke, Journal of Applied Physics **88**, 6910 (2000).

[105] R. Therrien, Ph.D. thesis, University of California, Berkeley, Berkeley, CA, 2002, thesis advisor: J. Clarke.

[106] R. M. Weisskoff, G. P. Lafyatis, K. R. Boyce, E. A. Cornell, R. W. F. Jr., and D. E. Pritchard, J. Appl. Phys. **63**, 4599 (1988).

[107] J. R. Claycomb and J. Miller, J. H., Review of Scientific Instruments **70**, 4562 (1999).

[108] X. Fan, S. E. Fayer, T. G. Myers, B. A. D. Sukra, G. Nahal, and G. Gabrielse, Review of Scientific Instruments **92**, 023201 (2021).

[109] M. Mck and J. Clarke, Review of Scientific Instruments **72**, 3691 (2001).

[110] P. W. Anderson and Y. B. Kim, Rev. Mod. Phys. **36**, 39 (1964).

[111] I. A. Golovchanskiy, A. V. Pan, T. H. Johansen, J. George, I. A. Rudnev, A. Rosenfeld, and S. A. Fedoseev, Phys. Rev. B **97**, 014524 (2018).

[112] D. Hanneke, S. Fogwell Hoogerheide, and G. Gabrielse, Phys. Rev. A **83**, 052122 (2011).

[113] J. N. Tan, Ph.D. thesis, Harvard University, 1992, (thesis advisor: G. Gabrielse).

[114] J. Tan and G. Gabrielse, Phys. Rev. A **48**, 3105 (1993).

[115] J. Tan and G. Gabrielse, Phys. Rev. Lett. **67**, 3090 (1991).

[116] H. Dehmelt, Proceedings of the National Academy of Sciences **83**, 2291 (1986).

[117] R. Van Dyck, Jr., P. Ekstrom, and H. Dehmelt, Nature **262**, 776 (1976).

[118] C. Tseng and G. Gabrielse, Applied Physics B **60**, 95 (1995).

[119] J. Van Dyck, R. S., F. L. Moore, D. L. Farnham, and P. B. Schwinberg, Review of Scientific Instruments **57**, 593 (1986).

[120] J. DiSciacca and G. Gabrielse, Phys. Rev. Lett. **108**, 153001 (2012), (correction: an observed Δf_z of 20 rather than 50 Hz signaled a 0.3 μm cyclotron radius.).

[121] A. Mooser *et al.*, Nature **509**, 596 (2014).

[122] B. M. Latacz *et al.*, Nature **644**, 64 (2025).

[123] X. Fan, A. Noguchi, and K. Taniguchi, Physical Review A **111**, 042806 (2025).

[124] G. Gabrielse, H. Dehmelt, and W. Kells, Phys. Rev. Lett. **54**, 537 (1985).

[125] R. S. Van Dyck, P. B. Schwinberg, and H. G. Dehmelt, in *The Electron: New Theory and Experiment*, edited by D. Hestenes and A. Weingartshofer (Springer Netherlands, Dordrecht, 1991), pp. 239–293.

[126] J. DiSciacca *et al.*, Phys. Rev. Lett. **110**, 130801 (2013).